HIGH FIDELITY DETERMINISTIC SOLUTION OF NEUTRON TRANSPORT PROBLEMS IN GRAPHITE

A Thesis

by

AARON J. HOLZAEPFEL

Submitted to the Office of Graduate and Professional Studies of
Texas A&M University
in partial fulfillment of the requirements for the degree of

MASTER OF SCIENCE

Chair of Committee,	Marvin L. Adams
Committee Members,	Ryan G. McClarren
	Raytcho D. Lazarov
Head of Department,	Yassin A. Hassan

August 2016

Major Subject: Nuclear Engineering

ABSTRACT

The study of thermal radiative transfer in the high energy density regime is important to the National Nuclear Security Administration, and experiments are an important component of such studies. Strong non-linear coupling of radiation hydrodynamics and thermal radiation transport makes it difficult to infer radiation transport uncertainties from experiments. In order to address this problem and have a hierarchical approach to model validation, the Center for Exascale Radiation Transport (CERT), created at Texas A&M University, has designed neutrons-in-graphite experiments as surrogates for thermal radiative transfer in high energy density. There is a strong mathematical analogy between the process of radiative absorption and emission, and the process of neutrons scattering in highly diffusive mediums. This allows the solution for thermal radiation transport benchmark problems to be measured by the neutrons-in-graphite surrogate experiments.

The CERT team has designed a series of neutrons-in-graphite experiments to allow investigation of many of the significant transport difficulties regarding thermal radiative transport including: muti-scale modelling in time, space, and angle; highly scalable parallel solution techniques; and refinement in time, space, and angle. The development of computation methods to efficiently and accurately simulate the neutrons-in-graphite surrogate experiments and the predictive science methods to quantify the uncertainty will also be applicable to the analogous thermal radiation transport simulations.

This thesis systematically investigates the required spatial, angular, and energy resolution needed to obtain high-fidelity deterministic transport solutions for the neutrons-in-graphite experiments designed as surrogates for thermal radiative transfer. Semi-analytic and stochastic methodologies are considered in order to investigate the deterministic neutron transport discretization error as a function of the spatial, angular, and energy resolution.

For the discretization error calculations, a hierarchical approach is taken towards increasingly complex geometries. Infinite graphite medium problems with a uniform source have only energy dependence. The infinite medium problems are used to compute the deterministic multi-group discretization error as a function of the energy resolution. 2D graphite problems with an infinite line source and 3D graphite cube problems with a point source are modelled to analyse spatial and angular discretization error as a function of spatial and angular resolution. An analysis is performed on the angular discretization ray effect errors that are present in deterministic discrete ordinate calculations. This research informs the uncertainty quantification efforts for CERT and points the way to the further development of deterministic calculations.

NOMENCLATURE

Abbreviations

AMR	Adaptive Mesh Refinement
CDF	Cumulative Density Function
CERT	Center for Exascale Radiation Transport
CSDA	Continuous Slowing Down Approximation
ENDF	Evaluated Nuclear Data Files
HED	High-Energy Density
LS	Level Symmetric
MCNP	Monte Carlo N-Particles
NNSA	National Nuclear Security Administration
PDF	Probability Density Function
PDT	Parallel Deterministic Transport
PSAAP	Predictive Science Academic Alliance Program
RRD	Reaction Rate Density

Symbols

$n\left(\vec{r},\vec{\Omega},E,t\right)$	6-Dimensional phase-space radiation density
$\psi\left(\vec{r},\vec{\Omega},E,t\right)$	Radiation angular flux
$\phi\left(\vec{r},E,t\right)$	Radiation scalar flux
$J\left(\vec{r},\vec{\Omega},E,t\right)$	Radiation current density
$S\left(\vec{r},\vec{\Omega},E,t\right)$	Extraneous source density
$I\left(\vec{r},E,t\right)$	Angular intensity
$\varphi\left(\vec{r},E,t\right)$	Angle integrated intensity
$\sigma(E)$	Neutron macroscopic cross-section
$\kappa(E)$	Photon macroscopic cross-section
$\sigma_s\left(\vec{r},E'\rightarrow E,\vec{\Omega},t\right)$	Single differential scatter cross-section
$\sigma_s\left(\vec{r},E'\rightarrow E,\vec{\Omega}'\rightarrow\vec{\Omega},t\right)$	Double differential scatter cross-section
$B(E,T)$	Planck function
h	Planck's constant
k	Boltzmann's constant
$Y_{kn}(\Omega)$	Spherical harmonics
$P_{kn}(\mu)$	Associated Legendre polynomial
ϵ_{L2}	Relative L2 error norm
$D(E)$	Diffusion coefficient
$\bar{\mu}_{0L}(E)$	Avg. value of the cosine of the scattering angle in lab frame
$q\left(\vec{r},u\right)$	Slowing down density
$\bar{\xi}(u)$	Average lethargy gain in a collision at lethargy u

TABLE OF CONTENTS

Page

LIST OF FIGURES

FIGURE Page

LIST OF TABLES

TABLE Page

1. INTRODUCTION

The study of radiation transport through matter is important in many applications of practical interest, including nuclear reactor design and analysis, medical diagnostics and therapy, climate modeling, remote sensing, and many others. The applications that motivates this thesis are those involving matter with high energy density (HED), in which the dominant heat-transfer mechanism is thermal radiative transfer. Important HED applications include astrophysical studies, nuclear fusion, and HED laboratory experiments.

Modelling thermal radiation transport requires a 7-dimensional phase space: 3 position variables, 2 direction variables, 1 energy variable, and 1 time variable. Thermal radiation transport in HED is multiscale in time, space, and direction. 10^{15} unknowns can easily be required for high-fidelity deterministic HED thermal radiation transport calculations. The development of efficient exascale computing with massively-parallel algorithms will play a vital role in achieving the required space, time, and angle resolution needed to obtain high-fidelity solutions to these difficult problems [26].

The study of thermal radiation transport is of vital importance to the National Nuclear Security Administration (NNSA). Current NNSA HED thermal radiation transport applications include the National Ignition Facility at Lawrence Livermore National Laboratory, Omega Laser System at University of Rochester, and the Z-machine pulsed power facility at Sandia National Laboratory. As part of the NNSA Predictive Science Academic Alliance Program (PSAAP), the Center for Exascale Radiation Transport (CERT) was created at Texas A&M University. CERT objectives can be broken down into two main goals. First, the development of computation methods to efficiently and accurately simulate thermal radiation transport in the HED regime using exascale computing. Second, the development of predictive science to quantify the input, simulated, and experimental uncertainty in the results [26].

A major challenge to the development of thermal radiation transport techniques in the HED is that HED thermal radiation transport experiments are not possible without the complicating factor of strong non-linear coupling of radiation with hydrodynamics. As result, it is difficult or impossible to draw separate inferences about errors stemming from the radiation and hydrodynamics portions of the computation. Fortunately, there exists a strong mathematical analogy between the process of radiative absorption and emission, and the process of neutrons scattering in highly diffusive mediums. This allows equivalent transport experiments to be performed outside of the HED regime [24]. This is the motivation for much of the work undertaken by the Center for Exascale Radiation Transport at Texas A&M University.

This thesis investigates the required spatial, angular, and energy resolution needed to obtain high-fidelity deterministic transport solutions for the neutrons-in-graphite experiments designed as surrogates for thermal radiative transfer in HED applications. This research is important to the CERT project as it systematically determines the discretization error as a function of the spatial, angular, and energy resolution for deterministic transport calculations in the neutrons-in-graphite problems that are being studied by CERT.

2. INTRODUCTION TO TRANSPORT THEORY

Radiation transport theory is the study of radiation transport and interactions through material, where “radiation” includes subatomic particles and photons. We shall use the term “particles” to include photons for simplicity of presentation. To describe the transport of radiation at a specific time, both the position and momentum of the radiation must be defined. This requires a 6-dimensional phase space: 3 position variables (x, y, z) or $(\vec{r})$, 2 direction variables (θ, γ) or $(\vec{\Omega})$, and 1 energy variable (E). The phase-space radiation density, denoted by $n\left(\vec{r}, \vec{\Omega}, E, t\right)$, is defined in Equation 2.1.

$$n\left(\vec{r}, \vec{\Omega}, E, t\right) d^3r \, d\vec{\Omega} \, dE = \begin{array}{c} \text{expected number of particles in}\, d^3r \,\text{about} \\ \vec{r}, \text{ energy interval}\, dE \,\text{about}\, E, \text{ moving in} \\ \text{direction}\, \vec{\Omega} \,\text{within solid angle}\, d\vec{\Omega} \,\text{at time}\, t \end{array} \tag{2.1}$$

$n\left(\vec{r}, \vec{\Omega}, E, t\right)$ has units $\left[\frac{\#\, particles}{cm^3 \cdot sr \cdot eV}\right]$. For simplicity the 6-dimensional differential phase space will be referred to as d^6V in future calculations. Multiplying the radiation phase-space density by the radiation speed results in radiation angular flux, $\psi\left(\vec{r}, E, \vec{\Omega}, t\right)$, shown in Equation 2.2. The scalar radiation flux, $\phi\left(\vec{r}, E, t\right)$, is obtained by integrating the angluar flux over all directions, as shown in Equation 2.3 [11].

$$\psi\left(\vec{r}, E, \vec{\Omega}, t\right) = n\left(\vec{r}, \vec{\Omega}, E, t\right) v\left(E\right) \tag{2.2}$$

$$\phi\left(\vec{r}, E, t\right) = \int_{4\pi} d\Omega \, \psi\left(\vec{r}, E, \vec{\Omega}, t\right) \tag{2.3}$$

Material properties of interest are reaction cross-sections. Reaction cross-sections represent the probabilities of specific reactions occurring as radiation travels through a medium. Microscopic cross-sections, $\sigma_{micro}\left(E\right)$, have units of area and represent the effective cross-sectional area presented by the target nucleus or atom to the radiation for a specific reaction. These microscopic cross-sections primarily depend on the type of radiation, the reaction occurring, energy of the radiation in the reference frame of the target atom, and the target nuclide. Many nuclear data libraries such as the Evaluated Nuclear Data Files (ENDF) have microscopic cross-sections tabulated for the different types of radiation, different reactions occurring, varying radiation energy, and different target nuclides. The macroscopic cross-sections, $\sigma_{macro}\left(E\right)$, for a specific nuclide is obtained by multiplying the microscopic cross-sections by the atom density of the nuclide as shown in Equation 2.4.

$$\sigma_{macro,i}(E) = \frac{\rho N_a}{M}\sigma_{micro,i}(E) = N\sigma_{micro,i}(E) \tag{2.4}$$

In Equation 2.4, ρ is the mass density, N_a is Avogadro's number, M is molar mass, and N is the atom density. Subscript i denotes the specific reaction occurring. The macroscopic cross-section for a material containing multiple nuclides is computed by summing the macroscopic cross-section of each nuclide as shown in Equation 2.5.

$$\sigma_{macro,i}^{mixture}(E) = \sum_{j=1}^{\#\,nuclides} N^j \sigma_{micro,i}^{j}(E) \tag{2.5}$$

The macroscopic cross-section represents the expected number of reactions per particle path length at energy E. For simplicity, in what follows the neutron reaction macroscopic cross-sections will be denoted with σ and the photon reaction macroscopic cross-sections will be denoted with κ. If there is no superscript, the cross section or opacity is for the relevant mixture. In thermal radiation transport, cross-sections are commonly referred as opacities.

Using these cross-sections, a reaction rate density (RRD) is the product of angular flux and macroscopic cross-section as shown in Equation 2.6

$$RRD\left[\frac{\#\,\text{reactions of type}\,i}{cm^3\cdot sr\cdot eV\cdot s}\right]=\psi\left(\vec{r},E,\vec{\Omega},t\right)\times\sigma_i(E,t) \tag{2.6}$$

Reactions are often separated into two broad categories: absorption and scattering. The total cross-section is the sum of the absorption, σ_a, and scattering, σ_s, cross-sections as shown in Equation 2.7.

$$\sigma_t(E,t)=\sigma_a(E,t)+\sigma_s(E,t) \tag{2.7}$$

Two other important reaction cross-section terms are macroscopic single differential scatter cross-sections and macroscopic double differential scatter cross-sections. The single differential scatter cross-section, $\sigma_s\left(\vec{r},E'\rightarrow E,t\right)$, is obtained by multiplying the macroscopic scatter cross-section by a probability density function which is outlined in Equation 2.8.

$$\sigma_s\left(\vec{r},E'\rightarrow E,t\right)=\sigma_s(E,t)f\left(\vec{r},E'\rightarrow E,t\right) \tag{2.8}$$

In Equation 2.8, $f\left(\vec{r},E'\rightarrow E,t\right)$ is a probability density function for a neutron with initial energy E' scattering into final energy E. $f\left(\vec{r},E'\rightarrow E,t\right)$ has units of inverse energy. $\sigma_s\left(\vec{r},E'\rightarrow E,t\right)dE$ represents the scatter cross-section for radiation with initial energy E' scattering into energy interval dE about E. Similarly, the double differential scatter cross-section, $\sigma_s\left(\vec{r},E'\rightarrow E,\vec{\Omega}'\rightarrow\vec{\Omega},t\right)$, is computed in Equation

2.9.

$$\sigma_s\left(\vec{r}, E' \rightarrow E, \vec{\Omega}' \rightarrow \vec{\Omega}, t\right) = \sigma_s(E,t) f\left(\vec{r}, E' \rightarrow E, \vec{\Omega}' \rightarrow \vec{\Omega}, t\right) \tag{2.9}$$

In Equation 2.9, $f\left(\vec{r}, E' \rightarrow E, \vec{\Omega}' \rightarrow \vec{\Omega}, t\right)$ is the probability density function for a neutron with initial energy E' and travelling in initial angle $\vec{\Omega}'$ scattering into final energy E and angle $\vec{\Omega}$. $f\left(\vec{r}, E' \rightarrow E, \vec{\Omega}' \rightarrow \vec{\Omega}, t\right)$ has units of inverse energy and inverse solid angle. $\sigma_s\left(\vec{r}, E' \rightarrow E, \vec{\Omega}' \rightarrow \vec{\Omega}, t\right) dE d\Omega$ represents the scatter cross-section for radiation with initial energy E' and travelling in initial angle $\vec{\Omega}'$ scattering into final energy interval dE about E and direction $\vec{\Omega}$ within solid angle $d\vec{\Omega}$. Integrating the single differential scatter cross-section over all energies or integrating the double differential scatter cross-section over all energies and angles will produce the regular scattering cross-section.

Another neutron cross-section category is the "transfer" cross-section denoted with σ_x. σ_x accounts for all collisional interactions where a neutron interacts with the matter and one or more neutrons emerge from the interaction. The "transfer" interactions include scattering, fission, and $(n, 2n)$ reactions. Single differential and double differential transfer cross-sections have the same form as shown above with the single differential and double differential scatter cross-sections.

2.1 Derivation of the General Radiation Transport Equation

A radiation transport equation can be derived by writing a conservation statement.

$$\begin{aligned} \int d^6V \, \frac{d}{dt}\left[n\left(\vec{r}, \vec{\Omega}, E, t\right)\right] &= Gain\,Rate - Loss\,Rate = \\ & Net\,Collision\,Rate + Extraneous\,Source\,Rate - Net\,Leakage\,Rate \end{aligned} \tag{2.10}$$

The net collision term refers to the collisions or reactions that cause the radiation to be gain or lost from the 6-dimensional phase-space. This term depends on the type of transport problem and will be left as shown in Equation 2.11 for now.

$$Net\,Collision\,Rate = \int d^6V \left.\frac{\partial n}{\partial t}\right|_c \tag{2.11}$$

The net leakage of radiation from a differential volume can be expressed with the following integral over its surface, S,

$$Net\,Outleakage\,Rate = \int d\Omega \int dE \int dS\, n\left(\vec{r}, \vec{\Omega}, E, t\right) v(E)\vec{\Omega} \cdot \vec{e}_n \tag{2.12}$$

where $\vec{e}_n$ is the unit vector normal to the surface S. Using Guass's divergence theorem, Equation 2.12 can be rewritten into Equation 2.13 [11].

$$Net\,Outleakage\,Rate = \int d^6V\, \vec{\Omega} \cdot \nabla\psi\left(\vec{r}, E, \vec{\Omega}, t\right) \tag{2.13}$$

Last, the extraneous source term is shown in Equation 2.14.

$$Extraneous\,Source\,Rate = \int d^6V\, S_{ext}\left(\vec{r}, E, \vec{\Omega}, t\right) \tag{2.14}$$

Putting the terms together:

$$\int d^6V \left\{\frac{1}{v}\frac{\partial\psi}{\partial t} - S_{ext} - \left.\frac{\partial n}{\partial t}\right|_c + \vec{\Omega} \cdot \nabla\psi\right\} = 0 \tag{2.15}$$

Equation 2.15 is valid regardless of what the phase-space subvolume of integration is. If an integral of a function is zero no matter what is the domain of integration, then the function itself is also zero. This results in the general radiation transport equation:

$$\frac{1}{v}\frac{\partial \psi}{\partial t} - S_{ext} - \left.\frac{\partial n}{\partial t}\right|_{c} + \vec{\Omega} \cdot \nabla \psi = 0 \tag{2.16}$$

In Equation 2.16, each term is now a rate density. Multiplying any term by d^6V will produce a rate in or out of a 6-D phase space element.

There are several assumptions built into the transport equation. These assumption include no particle-particle reactions, wave effects, or external effect such as gravity. These effects are negligible in both the neutron transport and thermal radiation transport problems of interest to CERT [24].

2.2 Neutron Radiation Transport

For neutron transport, neutrons can either be absorbed or scattered by the medium. The transport net collision rate term must account for neutrons absorbed or scattered out of any 6-D phase space element and for neutrons that have transferred (σ_x) into any 6-D phase space element. The net collision rate density term for neutrons is shown in Equation 2.17.

$$\left.\frac{\partial n}{\partial t}\right|_{c,nts} = -\sigma_t\left(E\right)\psi + \int_0^\infty dE' \int_{4\pi} d\Omega' \sigma_x\left(\vec{r}, \vec{\Omega}' \to \vec{\Omega}, E' \to E\right)\psi' \tag{2.17}$$

In Equation 2.17, $\sigma_t\left(E\right)$ is the total macroscopic cross section. $\sigma_t\left(E\right)\psi$ quantifies the neutron collision loss rate density. $\sigma_x\left(\vec{r}, \vec{\Omega}' \to \vec{\Omega}, E' \to E, t\right)$ is the macroscopic double differential transfer cross section. Integrating $\sigma_x\left(\vec{r}, \vec{\Omega}' \to \vec{\Omega}, E' \to E\right)\psi$ over all energy and solid angles quantifies the neutron collision gain rate density [11].

The final transport equation for neutrons is shown in Equation 2.18.

$$\frac{1}{v}\frac{\partial \psi}{\partial t} + \vec{\Omega} \cdot \nabla \psi + \sigma_t \psi = \int_0^\infty dE' \int_{4\pi} d\Omega' \sigma_x \left(\vec{r}, \vec{\Omega}' \rightarrow \vec{\Omega}, E' \rightarrow E, t\right) \psi' + S_{ext} \quad (2.18)$$

2.3 Thermal Radiation Transport

Thermal radiative transfer is the transfer of heat through electromagnetic waves. All forms of matter emit electromagnetic radiation. No medium is required for thermal radiation transport unlike conduction and convection heat transfer modes. Matter with HED has the dominant heat-transfer mechanism of thermal radiative transfer. In thermal radiation transport, photons can be scattered or absorbed in the medium. The medium also emits photons whose emission energy spectrum is described via a temperature dependent Planck function. The possible thermal radiation interactions are shown in Figure 2.1 [15].

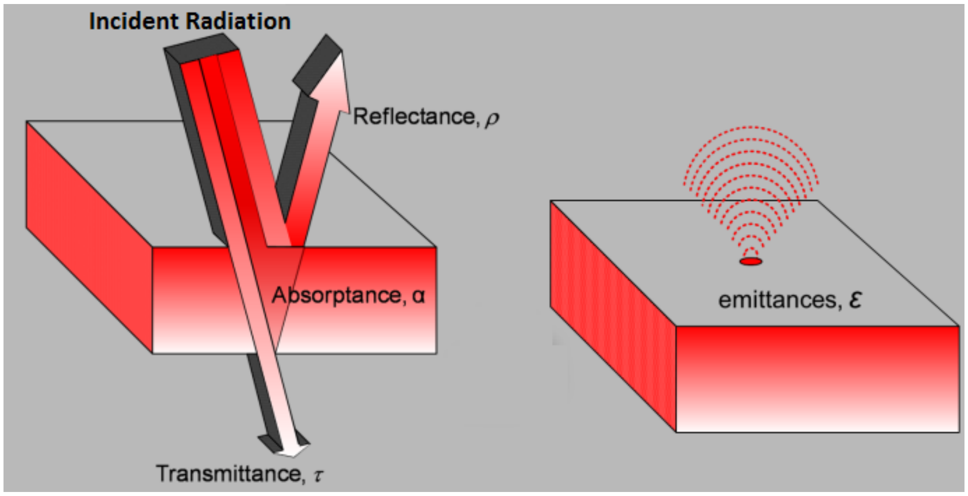

Figure 2.1: Thermal Radiation Properties [15].

Because both photon and material internal energy are conserved in thermal radiation transport, the thermal radiative transport equation is commonly written in terms of angular intensity, I, which is defined as angular flux multiplied by the radiation energy, E.

$$I\left(\vec{r},E,\vec{\Omega},t\right)=\psi\left(\vec{r},E,\vec{\Omega},t\right)E \tag{2.19}$$

Three factors must be included to define the thermal radiation transport net collision rate term. First is the loss rate density. Second is the gain rate density from scattering. Last, there is the emission gain rate density from the medium. The scattering process can often be approximated as monochromatic meaning that photons do not change energy in a scattering event. Additionally, scattering can often be approximated as isotropic. Thus the scattering gain rate density can be simplified as follows.

$$\int_{4\pi} d\Omega'\, I'\kappa_s\left(E,\vec{\Omega}'\rightarrow\vec{\Omega}\right)=\frac{\kappa_s(E)}{4\pi}\int_{4\pi} d\Omega'\, I'=\frac{\kappa_s(E)}{4\pi}\varphi\left(\vec{r},E,t\right) \tag{2.20}$$

In Equation 2.20, $\kappa_s\left(E,\vec{\Omega}'\rightarrow\vec{\Omega}\right)$ is the single differential scattering cross section for photons, $\varphi\left(\vec{r},E,t\right)$ is the angle-integrated intensity, and $\kappa_s\left(E\right)$ is the macroscopic Thompson scattering cross section [18].

The thermal radiation transport net collision rate density is shown in Equation 2.21:

$$\left.\frac{\partial n}{\partial t}\right|_{c,tr}=-I\left(\vec{r},E,\vec{\Omega},t\right)\kappa_t(E)+\frac{\kappa_s(E)}{4\pi}\varphi\left(\vec{r},E,t\right)+\kappa_e(E)B(T,E) \tag{2.21}$$

where $\kappa_t(E)$ is the macroscopic photon total cross section, $\kappa_e(E)$ is the macroscopic photon emission cross section, and $B(E,T)$ is the Planck function. In Equation

2.21, $I\left(\vec{r}, E, \vec{\Omega}, t\right) \kappa_t(E)$ represents the photon loss rate density from absorption or scatter, $\frac{\kappa_s(E)}{4\pi}\varphi\left(\vec{r}, E, t\right)$ quantifies the isotropic scattering gain rate density, and $\kappa_e(E)B(T, E)$ is the photon gain rate density from the medium's photon emission. When the radiation field is in equilibrium with the material, the angular intensity of the emitted radiation as function of energy can be described with the Planck function, which is outlined in Equation 2.22.

$$B(E, T) = \frac{2E^3}{h^3c^2}\left[\exp\left(\frac{E}{kT}\right) - 1\right]^{-1} \tag{2.22}$$

In Equation 2.22, h is Planck's constant, c is the speed of light, and k is Boltzmann's constant [18].

The final equation for thermal radiation transport is shown in Equation 2.23.

$$\frac{1}{c}\frac{\partial I}{\partial t} + \vec{\Omega} \cdot \nabla I + I\kappa_t = \frac{\kappa_s}{4\pi}\varphi + \kappa_e B(T, E) + S_{ext} \tag{2.23}$$

In Equation 2.23, c is the speed of light [18].

The radiation transport equation is non-linearly coupled to the material temperature, $T(\vec{r}, t)$, equation. The material temperature equation is simply a conservation statement as shown in Equation, 2.24:

$$C_v\frac{\partial T}{\partial t} = \int_0^\infty dE \int_{4\pi} d\Omega \left(\kappa_a I - \kappa_e B(T, E)\right) = \int_0^\infty dE \ \left(\kappa_a \varphi - 4\pi\kappa_e B(T, E)\right) \tag{2.24}$$

where C_v is the material heat capacity. We see that if photons are absorbed, their energy goes into the medium, raising its temperature. Likewise, the emission of photons causes the temperature to decrease [18]. Equation 2.24 assumes that the radiation field is in equilibrium with the material, which is valid for matter with

HED where conduction and convection heat transfer modes are negligible.

2.4 Neutrons as Surrogate for Thermal Radiation in the HED Regime

Modeling thermal radiation transport in HED presents multiple challenges. Thermal radiation transport in HED is multiscale in time, space, and direction. Real-world problems often have combinations of optically thin and optically thick regions. Boundary layers exist between these different regions. These boundary layers can significantly affect the solution even though they are orders of magnitude smaller than the full spatial domain. Angle variations on the order of microsteradians are significant in small streaming paths such as cracks. Opacities vary by many orders of magnitude with energy causing corresponding variations on the spatial and time scales. Within a material region, the absorption and scatter cross section can vary more than six orders of magnitude. 10^{15} unknowns can easily be required for high fidelity deterministic HED thermal radiation transport calculations. The development of exascale computing with massively-parallel algorithms will play a vital role in achieving the required space, time, and angle resolution needed to obtain high-fidelity solutions to these difficult problems [26].

A major challenge to the development of thermal radiation transport techniques in the HED is that HED thermal radiation transport experiments are not possible without the complicating factor of strong non-linear coupling of radiation hydrodynamics. As result the uncertainties from radiation transport can be impossible to extract from experiments. Fortunately, there exists a strong mathematical analogy between radiative absorption and emission, and neutrons scattering in highly diffusive mediums. This section goes through this analogy and how it can be used in the development of thermal radiation transport techniques.

Implicit time discretization is almost always used for time dependent particle transport calculations due to the very small time scales on which particles traverse computational cells. Let us consider the neutron transport equation shown in Equation 2.18 without any extraneous sources for simplicity. Integrating the neutron transport equation over $t_{k-1/2} < t < t_{k+1/2}$, dividing by $\nabla t^k = t_{k+1/2} - t_{k-1/2}$, and approximating

$$\frac{1}{\Delta t^k} \int_{t_{k-1/2}}^{t_{k+1/2}} dt\, \psi\left(\vec{r}, E, \vec{\Omega}, t\right) \approx \psi^{k+1/2}\left(\vec{r}, E, \vec{\Omega}\right) \tag{2.25}$$

yields Equation 2.26.

$$\begin{aligned} &\vec{\Omega} \cdot \nabla \psi^{k+1/2} + \left(\sigma_t + \frac{1}{v\Delta t}\right) \psi^{k+1/2} = \\ &\qquad \int_0^{\infty} dE' \int_{4\pi} d\Omega' \sigma_s\left(\vec{r}, \vec{\Omega}' \rightarrow \vec{\Omega}, E' \rightarrow E, t\right) \psi^{\prime,k+1/2} + \frac{1}{v\Delta t} \psi^{k-1/2} \end{aligned} \tag{2.26}$$

Equation 2.26 is a steady-state linear transport problem which must be solved at each time step [18]. Time discretizations more accurate than the "backward Euler" method shown here are often employed, but they also require solution of a series of steady-state transport problems of the form of Equation 2.26.

Thermal radiation is more complicated due to the nonlinear temperature dependence between the radiation transport and material temperature equations. Newton's method is generally used to solve the transport and material equations at each time step. Applying fully implicit (backward Euler) time discretization to the thermal radiation transport and material temperature equations shown in Equations 2.23 and 2.24 yields Equations 2.27 and 2.28 respectively [18].

$$\frac{1}{c\Delta t^k}\left(I^{k+1/2} - I^{k-1/2}\right) + \vec{\Omega} \cdot \nabla I^{k+1/2} + \kappa_t^{k+1/2} I^{k+1/2} = \frac{1}{4\pi} \kappa_s^{k+1/2} \varphi^{k+1/2} + \kappa_e^{k+1/2} B^{k+1/2} \tag{2.27}$$

$$\frac{C_v^{k+1/2}}{\Delta t^k}\left(T^{k+1/2}-T^{k-1/2}\right)=\int_0^\infty dE\ \left(\kappa_a^{k+1/2}\varphi^{k+1/2}-4\pi\kappa_e^{k+1/2}B^{k+1/2}\right) \tag{2.28}$$

Now let T^* denote the latest Newton iterate for the temperature and the superscript "$*$" denote a quantity evaluated at T^*. The next Newton iteration is obtained by evaluating the material properties at T^* and linearly expanding the temperature-dependent Plank function about T^* [18].

$$B^{k+1/2}\approx B^*+\frac{\partial B^*}{\partial T}\left(T^{k+1/2}-T^*\right) \tag{2.29}$$

Using Equation 2.29, material temperature dependence can be eliminated from the radiation transport equation. After some algebra the steady state thermal radiation transport equation can be written as follows:

$$\begin{aligned}&\vec{\Omega}\cdot\nabla I^{k+1/2}+\left(\kappa_t^*+\frac{1}{c\Delta t^k}\right)I^{k+1/2}=\\&\quad\frac{1}{4\pi}\kappa_s^*\varphi^{k+1/2}+\frac{1}{4\pi}\eta^*\chi^*\int_0^\infty dE'\int_{4\pi}d\Omega'\,\kappa_a^*\left(I'^{,k+1/2}-B^*(E)\right)+\xi^*+\frac{1}{c\Delta t^k}I^{k-1/2}\end{aligned} \tag{2.30}$$

In Equation 2.30, η^*, χ^*, and ξ^* are parameters evaluated at temperature T^*. These parameters are outlined in Equations 2.31, 2.32, and 2.33.

$$\eta^*(E)=\frac{4\pi\int_0^\infty dE\,\kappa_a^*(E)\frac{\partial B^*(E)}{\partial T}}{\frac{C_v^*}{\Delta t^k}+4\pi\int_0^\infty dE\,\kappa_a^*(E)\frac{\partial B^*(E)}{\partial T}} \tag{2.31}$$

$$\chi^*(E)=\frac{\kappa_a^*(E)\frac{\partial B^*(E)}{\partial T}}{\int_0^\infty dE'\,\kappa_a^*(E')\frac{\partial B^*(E')}{\partial T}} \tag{2.32}$$

$$\xi^*(E)=\kappa_a^*B^*-\frac{\eta\chi(E)}{4\pi}\left[\frac{C_v^*}{\Delta t^k}\left(T^{k-1/2}-T^*\right)\right] \tag{2.33}$$

The material temperature is given by Equation 2.34 [18].

$$T^{k+1/2} = T^{*} + \frac{\int_0^\infty dE\, \kappa_a^{*}(E)\left[\varphi(E) - 4\pi B^{*}(E)\right] + \frac{C_v^{*}}{\Delta t^{k}}\left(T^{k-1/2} - T^{*}\right)}{\frac{C_v^{*}}{\Delta t^{k}} + \int_0^\infty dE\, \kappa_a^{*}(E) 4\pi \frac{\partial B^{*}(E)}{\partial T}} \tag{2.34}$$

The steady state thermal radiation transport equation, shown in Equation 2.30, is very similar to the steady state neutron transport equation shown in Equation 2.26. Both are transport problems that can be solved using steady-state methods for each time step. The absorption/re-emission term in the thermal radiation transport equation is in the same form as the neutron scattering term in the neutron transport equation. In optically thick mediums, photon energy is absorbed and re-emitted many times during one time step. This is similar to neutrons scattering in a highly diffusive medium such as graphite [18]. With these close similarities it is proposed that solution methodologies for thermal radiation problems can be tested using neutrons-in-graphite experiments as a surrogate.

The following math outlines the equivalent transformation from a thermal radiation transport problem to a neutron transport problem that can be modelled experimentally. Consider the time-differenced neutron transport equation for specific energy group g and angular direction m shown in Equation 2.35.

$$\begin{aligned} &\frac{1}{v_g \Delta t}\left(\psi_{m,g}\left(\vec{r}\right) - \psi_{m,g}^{n-1/2}\left(\vec{r}\right)\right) + \vec{\Omega}_m \cdot \nabla \psi_{m,g} + \sigma_{t,g}\left(\vec{r}\right)\psi_{m,g}\left(\vec{r}\right) \\ &\qquad = \sum_{g'}^{G}\sum_{n=0}^{L} \frac{2n+1}{4\pi}\sigma_{x,n,g'\to g}\left(\vec{r}\right)\sum_{k=-n}^{n}\phi_{g'}^{kn}\left(\vec{r}\right) Y_{kn}(\vec{\Omega}) + q_{m,g}^{N,Fix}\left(\vec{r}\right) \end{aligned} \tag{2.35}$$

In Equations 2.35, $q_g^{N,Fix}$ is the fixed neutron source. The group transfer term has been reformulated using Legendre polynomial expansion where Y_{kn} are spherical harmonics which is given in Equation 2.36. $\sigma_{x,n,g'\to g}$ is the "transfer" cross-section from group g' to group g. The "transfer" cross-section accounts for all collisional interactions where a neutron interacts with the matter and one or more neutrons emerge from the interaction.

$$Y_{kn}(\vec{\Omega}) = \sqrt{\frac{(2n+1)(n-k)!}{4\pi(n+k)!}}P_{kn}(\mu)e^{ik\gamma} \tag{2.36}$$

In Equation 2.36, $P_{kn}(\mu)$ is the associated Legendre polynomial and γ is the azimuthal angle. See Chapter 3 in *Nuclear Reactor Theory* by George Bell and Samuel Glasstone for more information regarding Legendre polynomial expansion of the neutron transport equation [7].

The time-differenced thermal radiation transport equation for energy group g and angular direction m is given in Equation 2.37.

$$\begin{aligned}\frac{1}{c\Delta t}\left(I_{m,g}\left(\vec{r}\right) - I_{m,g}^{n-1/2}\left(\vec{r}\right)\right) + \vec{\Omega}_m \cdot \nabla I_{m,g} + \kappa_{a,g}\left(\vec{r}, T\left(\vec{r}\right)\right) I_{m,g}(\vec{r})& \\ = \kappa_{e,g}\left(\vec{r}, T\left(\vec{r}\right)\right)\frac{B_g\left(\vec{r}, T\left(\vec{r}\right)\right)}{4\pi} + q_{m,g}^{R,Scat}\left(\vec{r}\right) + q_{m,g}^{R,Fix}\left(\vec{r}\right)&\end{aligned} \tag{2.37}$$

In Equations 2.37, $q_g^{R,Scat}$ is the thermal radiation scatter term and $q_g^{R,Fix}$ stands for the fixed thermal radiation source. The radiation scatter term will be assumed to be negligible: $q_g^{R,Scat} = 0$. This is reasonable with thermal radiation transport in HED where the absorption and re-emission of photons are the dominant interactions. Consider a thermal radiation transport problem where the following replacements, given in Equations 2.38 and 2.39, can be made:

$$\kappa_{a,g} \leftarrow \sigma_{t,g} \tag{2.38}$$

$$c \leftarrow v_g \text{ in group } g \text{ time-derivative term} \tag{2.39}$$

After implementing Equations 2.38 and 2.39, the left-hand operator of the thermal radiation transport equation becomes the same as the neutron transport equation. Next, consider the following replacement for the photon emission cross-section shown in Equation 2.40.

$$\kappa_{e,g}\left(\vec{r}, T\left(\vec{r}\right)\right) \leftarrow \frac{\sum_{g'} \sigma_{x,0,g' \to g}\left(\vec{r}\right) \phi_{g'}^{0}\left(\vec{r}\right)}{B_g(T\left(\vec{r}\right))} \tag{2.40}$$

It is apparent from Equation 2.40 that the photon emission, $\kappa_{e,g} B_g$, will equal the isotropic component of the neutron "transfer" term. This should be true for any temperature, T, as long as B_g is nonzero. We now define the fixed radiation source as follows in Equations 2.41 and 2.42.

$$q_{m,g}^{R,Fix} \leftarrow q_{m,g}^{N,Fix} + \beta_g(\vec{r}, \vec{\Omega}_m) \sum_{g'} \sigma_{t,g'} \phi_{g'}^{0}(\vec{r}) \tag{2.41}$$

$$\beta_g(\vec{r}, \vec{\Omega}) = \frac{\sum_{g'} \sum_{n=1}^{L} \frac{2n+1}{4\pi} \sigma_{x,n,g' \to g}(\vec{r}) \sum_{k=-n}^{n} \phi_{g'}^{kn}(\vec{r}) Y_{kn}(\vec{\Omega})}{\sum_{g'} \sigma_{t,g'} \phi_{g'}^{0}(\vec{r})} \tag{2.42}$$

We now see that the thermal radiation fixed source will equal the fixed neutron source plus the anisotropic component of the neutron "transfer" term. Substituting the replacements for the photon emission cross-section and for the thermal radiation fixed source into the thermal radiation transport equation, the right-hand side of the radiative transfer equation becomes the same as that of the neutron transport equation. With the left-hand operator and the right-hand driving term the same between the thermal radiative transfer and the neutron transport equations, then as long as the boundary conditions are also the same, the radiative transfer equation should reproduce the neutron transport solution.

Lets now consider the time differenced matter energy equation shown in Equation 2.43.

$$\frac{C_v}{\Delta t}\left(T^{n+1/2}-T^{n-1/2}\right)=\sum_g\left(\kappa_{a,g}\varphi_g-\kappa_{e,g}B_g(T)\right) \tag{2.43}$$

Utilizing the above substitutions for κ_a and κ_e shown in Equations 2.38 and 2.40 respectively, the matter energy equation can be rewritten as shown in Equation 2.44:

$$\frac{C_v}{\Delta t}\left(T^{n+1/2}-T^{n-1/2}\right)=\sum_g\left(\sigma_{t,g}-\sigma_{x,g}\right)\phi_g^0 \tag{2.44}$$

where $\sigma_{x,g}$ is defined as

$$\sigma_{x,g}\left(\vec{r}\right)=\sum_{g'}\sigma_{x,0,g\to g'}\left(\vec{r}\right). \tag{2.45}$$

From Equation 2.44, it follows that $C_v\left(T^{n+1/2}-T^{n-1/2}\right)$ is equal to the net neutron loss density (neutrons per unit volume) during the nth time step. Solving the material temperature equation for temperature at t_{final} yields Equation 2.46.

$$T\left(\vec{r},t_{final}\right)=T\left(\vec{r},t_0\right)+\frac{1}{C_v}\int_{t_0}^{t_{final}}dt\sum_g\left(\sigma_{t,g}(\vec{r})-\sigma_{x,g}(\vec{r})\right)\phi_g^0(\vec{r},t) \tag{2.46}$$

C_v and $T(t_0)$ will be chosen such that T remains within a reasonable range throughout the duration of the problem, given the number of neutrons expected to be lost via collisions.

The end result of this transformation is a thermal radiation transport benchmark problem whose solution can be measured using neutrons-in-graphite surrogate experiments. In theory, with infinite energy, space, angle, and time resolution, the thermal radiation transport solution without any scattering should match the neutron experimental results. In reality, there will be experimental, iteration, truncation, equations of state, and cross-section input uncertainties to quantify [24].

3. OBJECTIVE

HED thermal radiation transport modelling requires radiation hydrodynamics. The strong non-linear coupling between radiation hydrodynamics and radiation transport is problematic. This tight coupling makes it difficult to determine if differences between simulations and experiments are caused from hydrodynamic errors, radiation transport errors, uncertainties in the equations of state, uncertainties in the opacity data, or a combination of these factors. It is advantageous to perform pure transport or pure hydrodynamic studies in order to have a hierarchical approach to model verification and validation [26]. It was mathematically shown in the previous section that there is a strong analogy between thermal radiation transport in HED and neutron scattering in a highly diffusive medium. This allows a single discipline study of thermal radiation transport to be performed using neutrons-in-graphite surrogate experiments.

Graphite provides a highly diffusive medium in which the effects of boundary layers and small streaming gaps can be examined. Multiscale dependence in time can be investigated using a fast neutron source since fast neutrons evolve on the time scale of 10^{-9}s while thermal neutrons may survive longer than 10^{-3}s. The CERT team has designed a series of neutrons-in-graphite experiments to allow investigation of many of the significant transport difficulties regarding thermal radiative transport including: muti-scale modeling in time, space, and angle; highly scalable parallel solution techniques; and refinement in time, space, and angle. Figure 3.1 sketches the characteristics of some of the planned neutrons-in-graphite experiments by the CERT team [26].

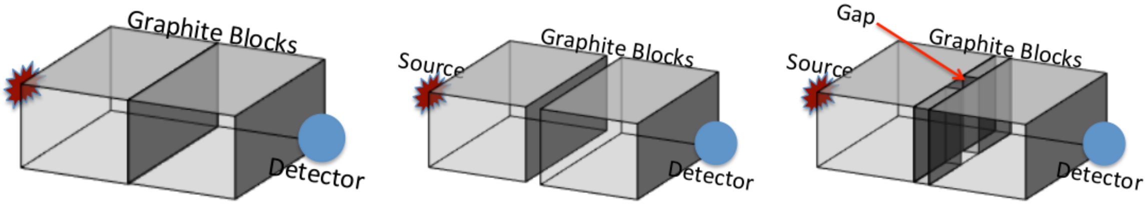

(a) A: No streaming path (b) B: 2D streaming path (c) C: 3D streaming path

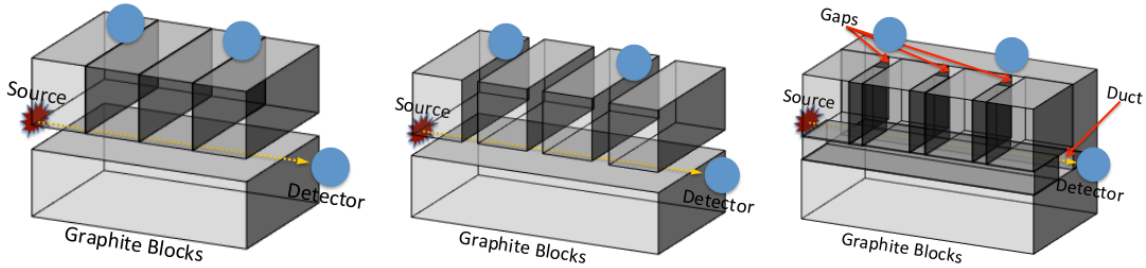

(d) A': No streaming path (e) B': 2D streaming path (f) C': 3D streaming path

Figure 3.1: Experiments for Neutron Transport with and without Thin Streaming Paths [26].

The development of predictive science methods and massively-parallel algorithms using the neutrons-in-graphite surrogate experiments and simulations will also applicable to analogous thermal radiation transport simulations. This allows the CERT team to develop thermal radiation multiscale transport models, exascale algorithms, and predictive science to quantify the input, simulated, and experimental uncertainties.

The main transport code that is being developed by CERT to model the neutrons-in-graphite surrogate experiments is Parallel Deterministic Transport (PDT). PDT is a massively parallel discrete ordinates deterministic transport code developed and maintained at Texas A&M University. Additional details regarding PDT methods and capabilities are given in the upcoming Computation Methods section. The objective of this thesis was to systematically determine the spatial, angular, and energy resolution required for high-fidelity PDT deterministic transport calculations of the neutrons-in-graphite experiments designed as surrogate for thermal radiation transport in HED. This research is important to the CERT project as it systematically investigates the discretization error as a function of the spatial, angular, and energy resolution for PDT deterministic computations of the neutrons-in-graphite surrogate problems.

4. METHODS

In order to compute the discretization error for the PDT deterministic transport calculations of the neutrons-in-graphite surrogate problems as function of energy, space, and angle resolution, the simulated results of varying energy, spatial, and angle refinement must be analysed. The PDT deterministic calculations was compared with the widely used stochastic neutron transport code, Monte Carlo N-Particles (MCNP), version 6. Developed and maintained at Los Alamos National Laboratory, MCNP is a well documented code that has undergone extensive verification and validation testing. For the purpose of these PDT deterministic discretization calculations, the MCNP solution was treated as the reference true solution. Additional information regarding the MCNP model is given in the upcoming Computation Methods section. The discretization error was computed using a relative L2 error norm whose formula is given in Equation 4.1.

$$\epsilon_{L2} = \left[\frac{\sum_j V_j \sum_i \left(\phi_{ref,i,j} - \phi_{PDT,i,j}\right)^2}{\sum_j V_j \sum_i \left(\phi_{ref,i,j}\right)^2} \right]^{1/2} \tag{4.1}$$

In Equation 4.1, ϕ is the cell averaged group neutron flux, subscript i denotes the energy group, subscript j denotes the spatial cell, and V_j is the volume in cell j.

In addition to the PDT deterministic and the MCNP Monte Carlo methods, a semi-anlytic solution approach was investigated. This method utilized the Continuous Slowing Down Approximation (CSDA) along with diffusion theory to obtain the transport solution for neutrons-in-graphite problems of interest. The strengths and weaknesses of this method was examined in comparison to the MCNP and PDT approaches. The derivation of the CSDA solution is outlined in the Computation Methods section. To systematically compute the PDT discretization error, a hierarchical approach was taken towards increasingly complex geometry problem sets.

4.1 Infinite Medium

The first set of problems consisted of an infinite graphite medium with a uniformly distributed source. For these problem sets, both AmBe and DT source spectra were modelled. In a AmBe source, Americium (Am-241) undergoes alpha decay. (α, n) reactions then occur with Beryllium (Be-9) to produce neutrons. There is also some fissions occurring in Am, which also produces neutrons. The AmBe source spectrum was calculated using SOURCES-4A by Dr. William Charlton. Sources-4A is a code system used for calculating source spectra taking into account (α, n) reactions, spontaneous fission, and delayed neutrons from radionuclide decay. The AmBe source spectrum is given in Figure 4.1. A python script was created to map this source spectrum to any desirable energy group structure. A DT source are neutrons that are produced from the fusion of Deuterium (H-2) and Tritium (H-3), typically induced in a linear accelerator. DT neutrons have energy of 14.1 MeV.

The solution to the infinite medium problems only have energy dependence, which is optimal in calculating the PDT deterministic discretization error as function of the energy resolution. Numerous group structures were considered starting with a baseline 99 groups structure. Variations of this baseline group set were constructed using additional or fewer thermal region, transition region from thermal to slowing down, slowing down region, and fast region energy groups. The transition region was found to be between $0.1eV$ and 0.5 eV. The energy discretization analysis was performed individually for the thermal region, transition region from thermal

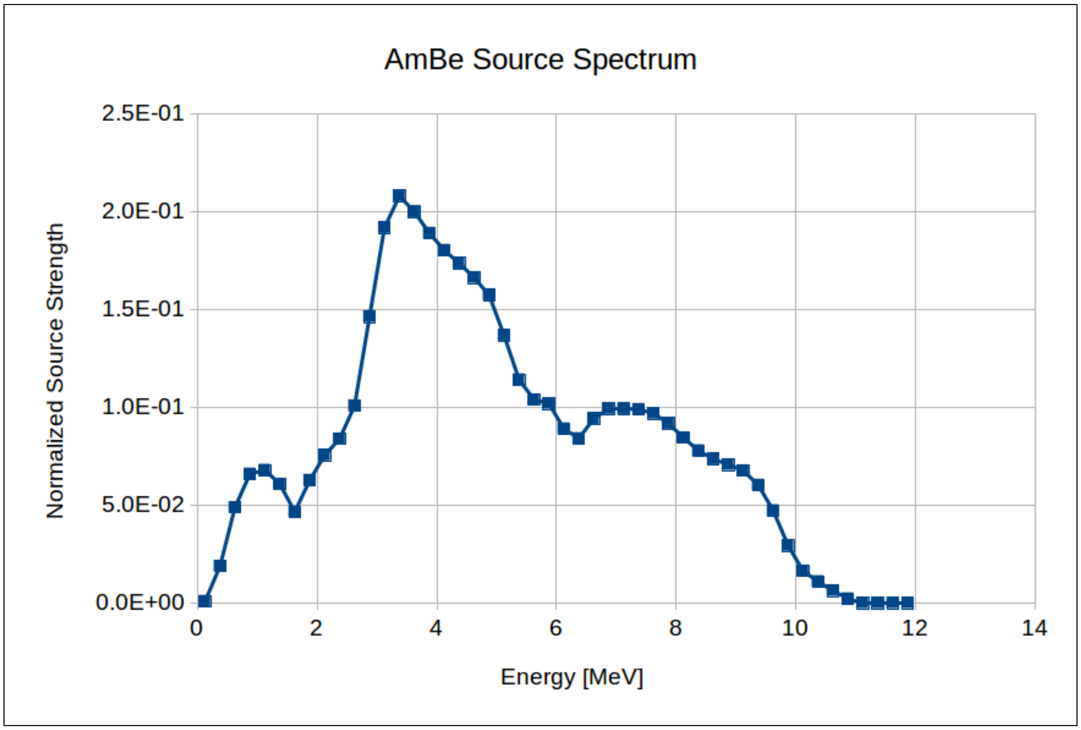

Figure 4.1: AmBe Source Spectrum.

slowing down, slowing down region, and fast region. For each region, the number of energy groups were varied in that specific region while keeping constant the number of energy groups in the other energy regions. The different energy groups structures are shown in Table 4.1.

The MCNP solution was also tallied for each group structure in order to compute the L2 error. The goal of the energy discretization analysis is to investigate how the number of energy groups in each energy region affects the discretizaiton error.

Table 4.1: Energy Group Structures.

Group Set	Group Description	Thermal Region Gps $E \leq 0.5$eV	Slowing Down Region Gps $0.5\text{eV} < E \leq 1.0$MeV	Fast Region Gps $E > 1.0$MeV
99 gp	Baseline Set	53	25	21
73 gp	Less Thermal	27	25	21
125 gp	More Thermal	79	25	21
87 gp	Less Slowing Down	53	13	21
112 gp	More Slowing Down	53	38	21
107 gp	More Transition	61	25	21
115 gp	More Transition	69	25	21
138 gp	More Transition	77	40	21
119 gp	More Fast	53	25	41
159 gp	More Fast	53	25	81

4.2 2D Geometry

The second problem set looked at 2D geometry where length in the x and y axes are bounded, but is infinite in the z axis. To achieve this, reflective boundary conditions in the z-axis was utilized in both the PDT and MCNP models. These problems utilized an approximate infinite AmBe line source parallel to the z-axis centered in the middle of the x and y axes geometry. The approximate line source had dimensions of $1cm \times 1cm$ in the x and y dimensions and extruded along the z axis. $1m \times 1m$ and $10m \times 10m$ graphite geometries were considered. A spatial and angular analysis was performed on the 2D geometry in order to investigate the solution sensitivity to the spatial and angular resolution.

The spatial analysis for the 2D geometry considered 4^2, 8^2, 16^2, 32^2, and 64^2 spatial cell refinement. The spatial flux distribution for these cell refinements was compared to the MCNP solution. A L2 error analysis was performed to investigate the 2D geometry spatial discretization error as function of the spatial resolution. For these calculations, 2048 discrete angles were used for all energy groups.

Discrete ordinate methods suffer an undesirable phenomena known as ray effects when the angular variables are under resolved. Ray effects produces spatial oscillations in the neutron flux solution. The ray effects will be more dominant at high neutron energies. Thus more quadrature directions will be needed in the higher neutron energy groups. The purpose of the angular analysis is to determine the necessary angular resolution at various energy levels. Ray effects will be further discussed in the Computation Methods section.

The angular analysis was performed by testing varying number of polar angles per hemisphere and azimuthal angles per quadrant. This testing was done independently in 7 energy ranges with the following energy divisions: $1 \times 10^{-11} MeV$, $1.78 \times 10^{-5} MeV$, $1 \times 10^{-3} MeV$, $0.1 MeV$, $1.0 MeV$, $4.94 MeV$, $9.0 MeV$, and $14.1 MeV$. In each of these energy ranges, an independent angular analysis was performed by varying the number of polar and azimuthal angles within that energy range while keeping the number of polar and azimuthal angles constant for all other energy groups. This was done in order to determine the angular resolution sensitivity in varying energy ranges. The angular analysis was performed for both the $1m \times 1m$ and $10m \times 10m$ geometries. Table 4.2 outlines the quadrature sets utilized in the angular analysis. The 2048 angle quadrature set was utilized in energy groups where the angle set was being held constant. 32^2 spatial cells were utilized in the 2D angular analysis calculations. The 2D PDT solution for each tested angle set in each of the 7 energy ranges was compared to the MCNP solution in order to perform an L2 error analysis on the angular resolution.

Table 4.2: Angle Sets.

Polar Angles per Hemisphere	Azimuthal Angles per Quadrant	Total Number of Angles
4	4	128
8	8	512
16	16	2048
32	32	8192
64	64	32768

4.3 3D Geometry

The last problem set looked at 3D geometry. $(1m)^3$ and $(10m)^3$ graphite cubes were considered with an approximate point AmBe source. The point source was centered in the cube geometry and had dimensions of $1cm^3$. Similar to the 2D geometry analysis, cm independent analyses were performed for the spatial and angular resolution. The 3D spatial analysis looked at 4^3, 8^3, 16^3, 32^3, and 64^3 spatial cells. The MCNP solution was tallied and plotted using the 64^3 cell refinement. L2 error calculations were done for these spatial resolutions. In these calculations, 2048 discrete angles were used for all energy group sets.

The same quadrature sets from the 2D analysis, given in Table 4.2, were used for the 3D geometry. Once again the quadrature sets were tested for 7 intervals: $1\times10^{-11}MeV$, $1.78\times10^{-5}MeV$, $1\times10^{-3}MeV$, $0.1MeV$, $1.0MeV$, $4.94MeV$, $9.0MeV$, and $14.1MeV$. Just as was done for the 2D angular analysis, in each energy range, an independent analysis was performed by varying the quadrature set in a specific energy range while keeping the quadrature set constant in all other energy groups. This was done for the $(1m)^3$ geometry using 64^3 spatial cells.

5. COMPUTATION METHODS

This section will go into detail regarding the computation models utilized in this research. It is informative to investigate a variety of computation approaches ranging from semi-analytic to Monte Carlo to high-fidelity deterministic. Different techniques have different strengths and weaknesses and provide different insights. A continuous slowing down approximation (CSDA) code was developed for the semi-analytic method. MCNP6 was utilized for the Monte Carlo approach. PDT was employed for the deterministic method.

The neutron cross-sections in graphite were obtained from the evaluated nuclear data files (ENDF) version VII as processed by NJOY 2012 [22]. Figure 5.1 shows the neutron total, elastic scatter, inelastic scatter, and absorption microscopic cross-sections for free carbon. Free carbon cross-sections are the cross-sections for a unbound, unordered (free) carbon. In other words, free carbon cross-sections do not account for any molecular structures. At thermal energies, the kinetic energy of the neutrons are similar to energies of excitation in molecules and crystalline lattices. As result, the binding energies of molecular or crystalline lattices must be taken into account and the free-gas model is no longer appropriate. This is handled by what is known as $S(\alpha, \beta)$ cross-sections, where S stands for scattering, α stands for a momentum transfer variable, and β is an energy transfer variable. $S(\alpha, \beta)$ cross-sections include incoherent inelastic scattering and coherent elastic scattering for graphite. Coherent scattering is where neutron waves scattered from different nuclei interfere with each other leading to a series of “Bragg edges”. In Incoherent scattering, the neutrons waves combine without interference effects. Figure 5.2 depicts a close look at

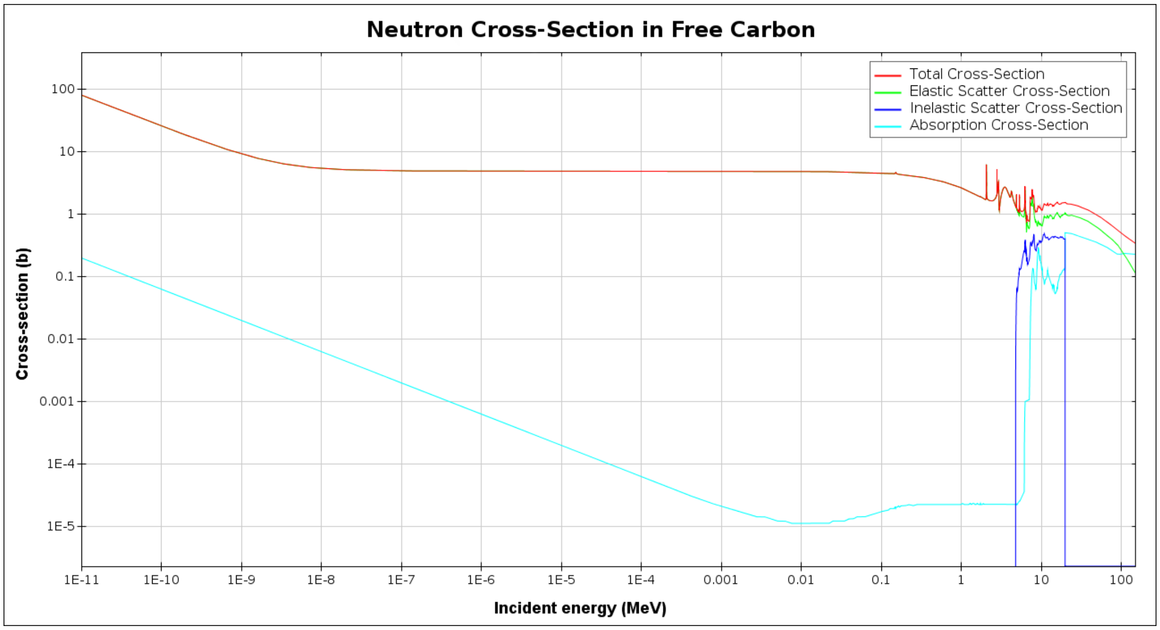

Figure 5.1: Microscopic Cross-Sections for Free Carbon.

the graphite neutron cross-section in the thermal region. In Figure 5.2, MT 221 is the free-gas total cross-section, MT 229 is the incoherent inelastic scattering cross-section, MT 230 is the coherent elastic scattering cross-section, and MT 229+230 is the total cross-section. It is apparent that the coherent elastic scattering cross-section has discontinuities (Bragg edges) [22].

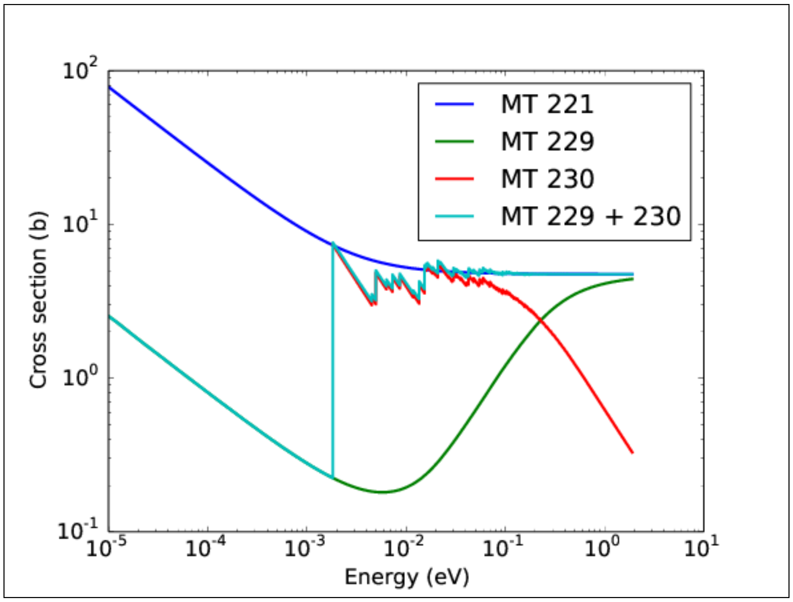

Figure 5.2: Neutron Cross-Section for Graphite at Thermal Energies.

5.1 CSDA

The CSDA is a treatment of the scattering process that makes semi-analytic solutions possible. The CSDA is briefly explained below. The energy dependent diffusion equation for a homogeneous medium is shown in Equation 5.1:

$$-D(E)\nabla^2\phi(\vec{r},E)+\sigma_t(E)\phi(\vec{r},E)=\int_0^E dE\,\sigma_s(E'\to E)\phi(\vec{r},E)+S(\vec{r},E) \qquad (5.1)$$

where $D(E)$ is the diffusion coefficient, $\phi(\vec{r},E)$ is the neutron flux, $\sigma_t(E)$ is the total macroscopic cross-section, $\sigma_s(E'\to E)$ is the single differential scattering cross section from energy E' to energy E, and $S(\vec{r},E)$ is the extraneous source. Equation 5.1 was obtained by first taking the 0th angular moment of the neutron transport equation by integrating, Equation 2.18, over all angular directions. Fick's law is then used to relate the neutron current density, $J(\vec{r},E)$, to the scalar flux as shown in

Equation 5.2.

$$\vec{J}(\vec{r}, E) = \int_{4\pi} d\Omega\, \vec{\Omega}\psi\left(\vec{r}, \vec{\Omega}, E, t\right) \approx \frac{-1}{3\sigma_{tr}(E)} \nabla\phi(\vec{r}, E) = -D(E)\nabla\phi(\vec{r}, E) \tag{5.2}$$

In Equation 5.2, $\sigma_{tr}(E)$ is known as the transport cross-section. The diffusion coefficient is calculated as shown in Equation 5.3.

$$D(E) = \frac{1}{3\sigma_{tr}(E)} = \frac{1}{3\left[\sigma_t(E) - \bar{\mu}_{0L}(E)\sigma_s(E)\right]} \tag{5.3}$$

In Equation 5.3, $\bar{\mu}_{0L}$ is the average value of the cosine of the scattering angle in the lab frame.

Using the ENDF data, the scattering distributions for elastic scatter and the first three inelastic scattering states were obtained for neutrons-in-graphite. The average cosine of the scattering angle was computed using Equation 5.4.

$$\begin{aligned} \bar{\mu}_{0L}(E) = \overline{\cos\theta_L} = \frac{\int_{4\pi} d\Omega\, \sigma(E, \theta_L)\cos\theta_L}{\int_{4\pi} d\Omega\, \sigma(E, \theta_L)} &= \frac{2\pi\sigma_s(E)\int_{-1}^{+1} d\mu_{0L}\, P_L(\mu_{0L})\mu_{0L}}{2\pi\sigma_s(E)\int_{-1}^{+1} d\mu_{0L}\, P_L(\mu_{0L})} \\ &= \int_{-1}^{+1} d\mu\, \mu_{0L}(E)P_L(\mu_{0L}) \end{aligned} \tag{5.4}$$

In Equation 5.4, θ_L is the scattering angle in the lab frame, μ_{0L} is the cosine of the scattering angle θ_L, and $P_L(\mu_{0L})$ is the probability of the scattering angle occurring. $\bar{\mu}_{0L}$ must be calculated for elastic and each inelastic scattering. The final average cosine of the scattering angle is obtained by taking a cross-section weighted average of the elastic and inelastic scattering components.

$$\bar{\mu}_{0L}(E) = \frac{\sigma_e(E)\bar{\mu}_{0L,e}(E) + \sum_{l=1}^{3}\sigma_{il}(E)\bar{\mu}_{0L,il}(E)}{\sigma_e(E) + \sum_{l=1}^{3}\sigma_{il}(E)} \tag{5.5}$$

Subscript $e, i1, i2, i3$ refer to each respective elastic and inelastic scattering, where il refers to the l-th excitation level in which the nucleus is left. The computed average cosine of the scattering angle for elastic and each inelastic scatter for carbon (graphite) is shown in Figures 5.3 through 5.6.

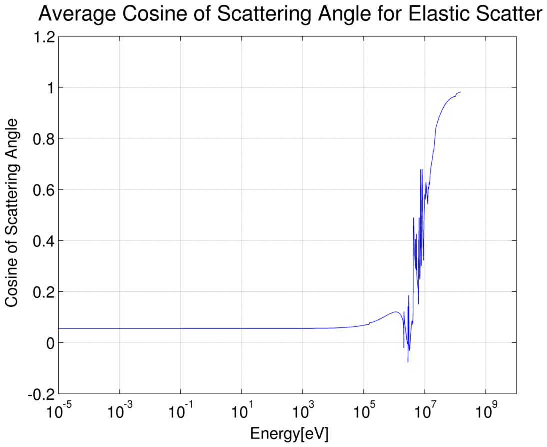

Figure 5.3: Elastic $\bar{\mu}_{0L}$

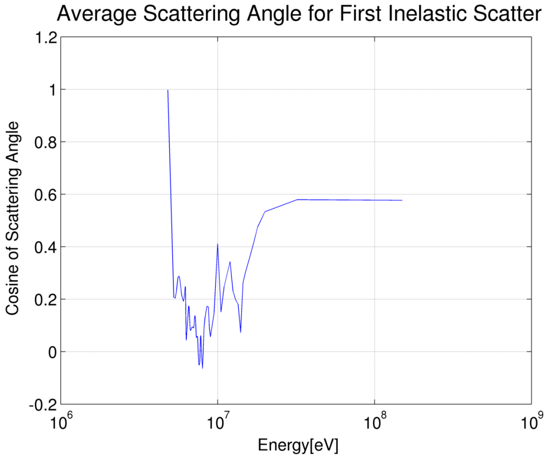

Figure 5.4: 1st Inelastic $\bar{\mu}_{0L}$

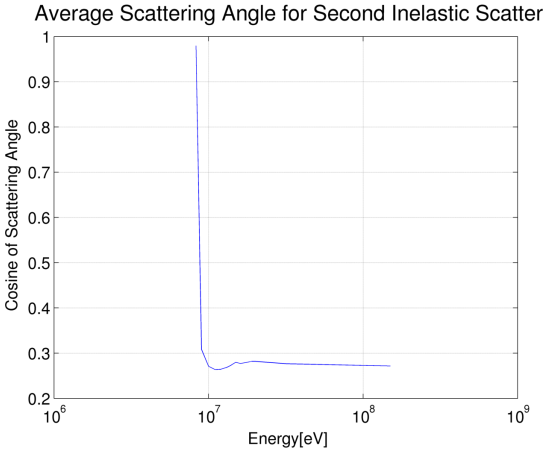

Figure 5.5: 2nd Inelastic $\bar{\mu}_{0L}$

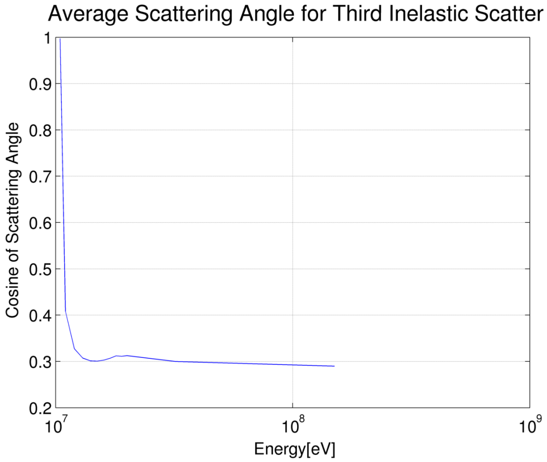

Figure 5.6: 3rd Inelastic $\bar{\mu}_{0L}$

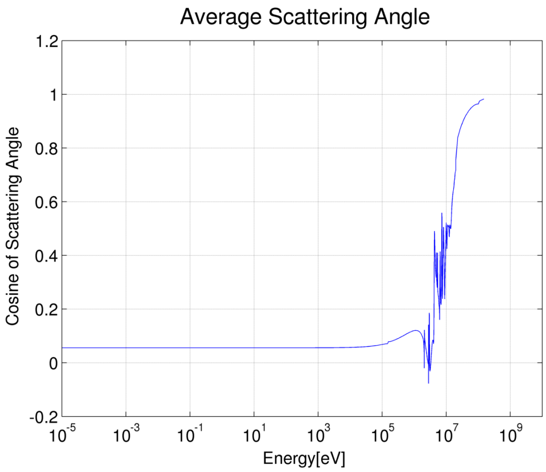

Figure 5.7: Average Cosine of the Scattering Angle.

It can be shown that for elastic scattering that is isotropic in the center-of-mass reference frame, the average cosine of the scattering angle reduces to $2/3A$ where A is the atomic mass. See section 2.9 of *Nuclear Reactor Theory* by John R. Lamarsh for derivation of this equality [17]. This isotropic limit is clearly seen at the lower energy of the average cosine of the elastic scattering angle in Figure 5.3. This was expected since isotropic scattering is dominant at lower energies as shown in Figure 5.8.

At higher energies, anisotropic scattering in the center-of-mass frame becomes significant, which is clearly seen in both the average cosine of the elastic scattering angle shown in Figure 5.3 and in the elastic differential scattering probability density function in the center-of mass frame, $P_C(\mu_{0C}, E)$, given in Figure 5.8. The average cosine of the inelastic scattering angles is seen to have a low-energy limit that approaches 1 and thus a scattering angle of 0, for energies just above the threshold for the reaction. This occurs at the threshold energy limits, because the neutron must lose all

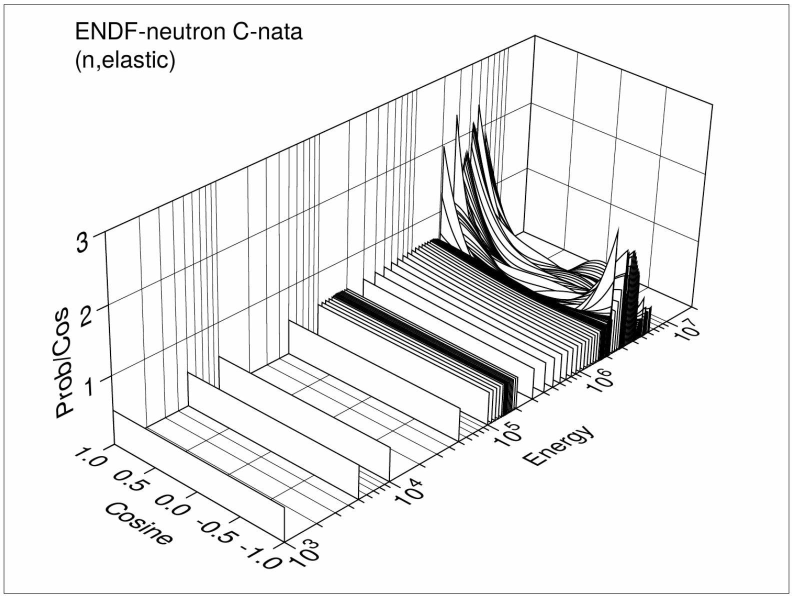

Figure 5.8: Elastic Differential Scattering Probability Density Function in the Center of Mass Frame, $P_C(\mu_{0C}, E)$, in Graphite.

of its kinetic energy in order to place the graphite nucleus in the associated excited state. The average cosine of the scattering angle, shown in Figure 5.7, is seen to be dominated by the elastic scattering component, which is expected since the elastic scattering cross-section is much larger than the inelastic scattering cross-section as shown in Figure 5.1.

It is convenient to describe neutron collisions in terms of a variable called lethargy denoted with u. Lethargy is defined in Equation 5.6:

$$u(E) = \ln\left(\frac{E_0}{E}\right) \tag{5.6}$$

where E is the corresponding energy and E_0 is the maximum energy. Converting the energy dependent diffusion equation to lethargy units, Equation 5.7 is obtained.

$$-D(u)\nabla^2\phi(\vec{r},u)+\sigma_t(u)\phi(\vec{r},u)=\int_0^u \sigma_s(u'\rightarrow u)\phi(\vec{r},u')+S(\vec{r},u) \tag{5.7}$$

When slowing down, neutrons gain almost equal amounts of lethargy per collision. CSDA pretends that neutrons slow down continuously such that there are no jumps in energy or lethargy. Given CSDA, neutron flux can be expressed in terms of slowing down density as shown in Equation 5.8:

$$q(\vec{r},u)=\phi(\vec{r},u)\bar{\xi}(u)\sigma_s(u) \tag{5.8}$$

where $q(\vec{r},u)$, the slowing down density, is the rate per cm^3 that neutrons are slowing down from $u_i < u$ to $u_f > u$; $\bar{\xi}(u)$ is the average lethargy gain in a collision at lethargy u; and $\sigma_s(u)$ is the macroscopic neutron scattering cross-section at lethargy u.

$\bar{\xi}(u)$ is calculated in Equation 5.9.

$$\begin{aligned}\bar{\xi}(u)=\overline{\Delta u}=\frac{\int_{4\pi} d\Omega\,\sigma(u,\theta_C)\Delta u(\mu_{0C})}{\int_{4\pi} d\Omega\,\sigma(u,\theta_C)} &= \frac{2\pi\sigma_s(E)\int_{-1}^{+1} d\mu_{0C}\,P_C(\mu_{0C})\Delta u(\mu_{0C})}{2\pi\sigma_s(E)\int_{-1}^{+1} d\mu_{0C}\,P_C(\mu_{0C})} \\ &= \int_{-1}^{+1} d\mu\,P_C(\mu_{0C})\Delta u(\mu_{0C})\end{aligned} \tag{5.9}$$

In Equation 5.9, θ_C is the scattering angle in the center of mass frame, $P_C(\mu_{0C})$ is the probability of the scattering angle occurring, and $\Delta u(\mu_{0C})$ is the change in lethargy for the specified scattering angle. The change in lethargy is calculated as shown in Equation 5.10.

$$\Delta u=u_f-u_i=\ln\left(\frac{E_i}{E_f}\right) \tag{5.10}$$

$\bar{\xi}(u)$ must be calculated for elastic and each level of inelastic scattering. The final average lethargy gain is computed with a cross-section weighted average of the elastic and inelastic average lethargy gain components.

$$\bar{\xi}(u) = \frac{\sigma_e(u)\bar{\xi}_e(u) + \sum_{l=1}^{3} \sigma_{il}(E)\bar{\xi}_{il}(u)}{\sigma_e(u) + \sum_{l=1}^{3} \sigma_{il}(u)} \tag{5.11}$$

The average lethargy gain for elastic and each inelastic scattering is depicted in Figures 5.9 through 5.13.

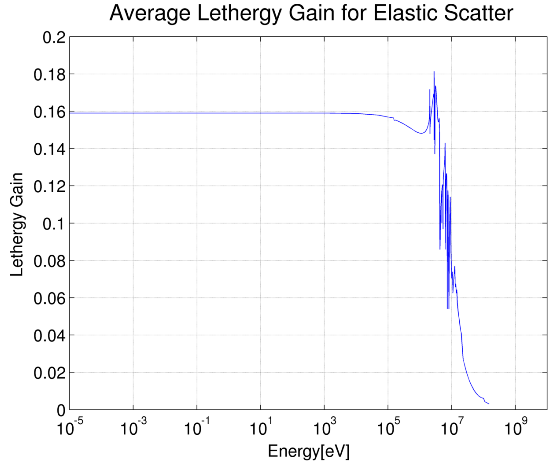

Figure 5.9: Elastic $\bar{\xi}(u)$

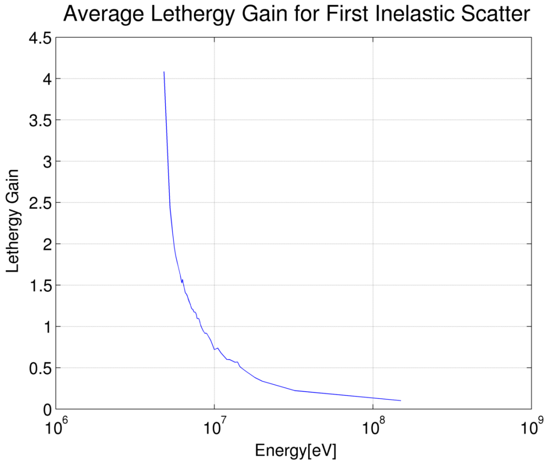

Figure 5.10: 1st Inelastic $\bar{\xi}(u)$

For elastic scattering, the average lethargy gain is seen to plateau at lower energies. This is due to Equation 5.9 being simplified to $2/(A + 2/3)$ for cases of isotropic scattering in the center-of-mass frame. This derivation can be found in section 6.4 of *Nuclear Reactor Theory* by John R. Lamarsh. For graphite, this limit comes out to be about 0.158 which is clearly shown in Figure 5.9. The effects of anisotropic scattering can be seen at the higher energies.

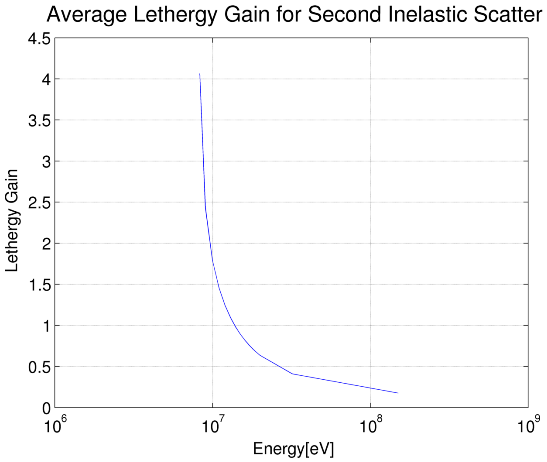

Figure 5.11: 2nd Inelastic $\bar{\xi}(u)$

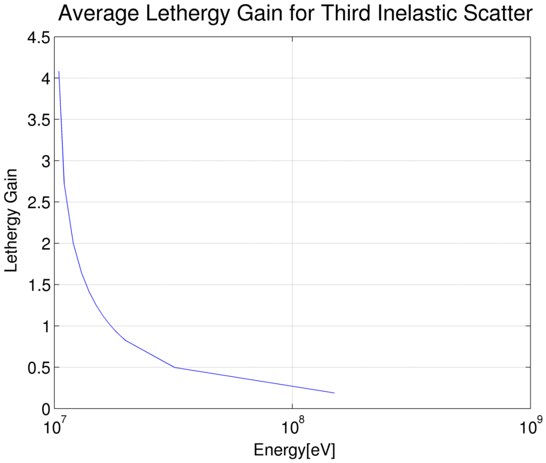

Figure 5.12: 3rd Inelastic $\bar{\xi}(u)$

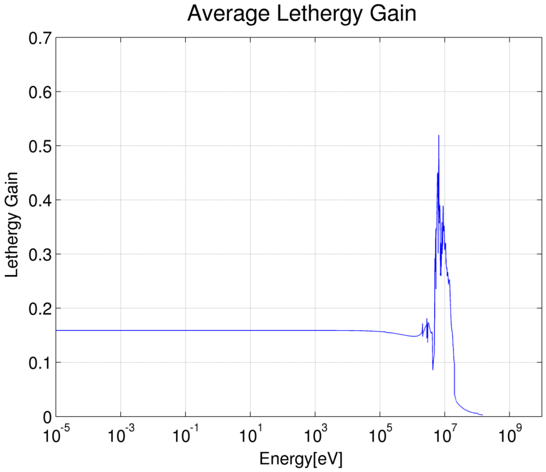

Figure 5.13: Average Lethargy Gain.

For inelastic scattering it is seen that near-threshold energies produce larger lethargy gain on average in a collision. This is due to the energy loss (or lethargy gain) due to excitation of the graphite nuclide becoming more significant as the energy of the particle approaches the energy threshold for excitation.

Using the slowing down density simplifies the diffusion equation into Equation 5.12.

$$\frac{-D(u)}{\bar{\xi}(u)\sigma_s(u)}\nabla^2 q(\vec{r},u) + \frac{\sigma_a(u)}{\bar{\xi}(u)\sigma_s(u)}q(\vec{r},u) = \frac{\partial q}{\partial u} + S(\vec{r},u) \tag{5.12}$$

Equation 5.12 is separable with lethargy and position as shown in Equations 5.13 and 5.14.

$$q(\vec{r},u) = \sum_n q_n(u)\psi(\vec{r}) \tag{5.13}$$

$$S(\vec{r},u) = \sum_n S_n(u)\psi(\vec{r}) \tag{5.14}$$

Assume eigenvalue functions shown in Equation 5.15.

$$-\nabla^2\psi_i(\vec{r},u) = B_i^2 q(\vec{r},u) \tag{5.15}$$

Inserting the separable eigenvalue solution into the CSDA diffusion equation, applying linear independence (i.e. each ψ_i is independent), and simplifying produces Equation 5.16.

$$\frac{dq_n(u)}{du} + \alpha_n(u)q_n(u) = S_n(u) \tag{5.16}$$

$$\alpha_n = \frac{D(u)B_n^2 + \Sigma_a(u)}{\bar{\xi}(u)\Sigma_s(u)} \tag{5.17}$$

Equation 5.16 can be solved using integrating factor $e^{\int_u^u du'\,\alpha_n(u')}$ to obtain Equation

5.18.

$$q_n(u) = q_n(0)e^{-\int_0^u du''\alpha_n(u'')} + \int_0^u du' e^{-\int_{u'}^u du''\alpha_n(u'')} S_n(u') \tag{5.18}$$

For a DT source, all neutrons are born with energy 14.1 MeV. As result there are no neutrons above 14.1 MeV ($u = 0$). In other words, there are no neutrons slowing down to 14.1 MeV and thus the initial condition will simply be: $q_n(0) = 0$.

To compute the source term. Equation 5.14 is multiplied by $\psi'(\vec{r})$ and integrated over the extrapolated domain:

$$\int_{V+} dV\, S(\vec{r}, u)\psi'_n(\vec{r}) = \sum_n \left[S_n(u) \int_{V+} dV\, \psi_n(\vec{r})\psi'_n(\vec{r}) \right] \tag{5.19}$$

We know from the theory of Laplacian eigenfunctions that ψ'_n and ψ_n are orthogonal such that:

$$\int_{V+} dV\, \psi'_n(\vec{r})\psi_n(\vec{r}) = \begin{cases} \int_{V+} dV\, \psi_n(\vec{r})^2 & \text{if } n = n' \\ 0 & \text{if } n \neq n' \end{cases} \tag{5.20}$$

Applying Equation 5.20 simplifies equation 5.19 as shown in Equation 5.21.

$$\int_{V+} dV\, S(\vec{r}, u)\psi'_n(\vec{r}) = S_n(u) \int_{V+} dV\, \psi_n(\vec{r})^2 \tag{5.21}$$

The spatial solution, $\psi_n(\vec{r})$, can be solve as in standard 1 group diffusion equations. Equation 5.22 outlines the spatial solution for the infinite, 2D, and 3D geometry problems discussed in the Methods section. See Section 5.3 of *Nuclear Reactor Analysis* by James Duderstadt and Louis Hamilton for the derivation of 1 group diffusion solutions in basic geometries [11].

$$\psi_n(\vec{r}) = \begin{cases} C & \text{for } n=0\text{, Infinite Medium Geometry} \\ C\cos\left(\frac{i\pi}{\tilde{a}}x\right)\cos\left(\frac{j\pi}{\tilde{b}}y\right) & \text{for } i,j = \text{odd, 2D Geometry} \\ C\cos\left(\frac{i\pi}{\tilde{a}}x\right)\cos\left(\frac{k\pi}{\tilde{c}}y\right)\cos\left(\frac{j\pi}{\tilde{b}}z\right) & \text{for } i,j,k = \text{odd, 3D Geometry} \end{cases} \tag{5.22}$$

In Equation 5.22, C is a constant and $\tilde{a}, \tilde{b}$, and $\tilde{c}$ are the extrapolated widths. n is the shorthand index notation for the eigenvalue functions. In 2D geometry, the eigenvalue functions have 2 indexes (i, j). 3D geometry has eigenvalue functions with 3 indexes (i, j, k). Extrapolated boundaries are the surfaces on which the scalar flux in the interior of a problem would become zero if smoothly extrapolated outside of the physical boundary. The extrapolated widths are:

$$\tilde{a} = a + 4.26D, \quad \tilde{b} = b + 4.26D, \quad \tilde{c} = c + 4.26D \tag{5.23}$$

where $\pm\tilde{a}/2$, $\pm\tilde{b}/2$, and $\pm\tilde{c}/2$ are the extrapolated boundaries, and $\pm a/2$, $\pm b/2$, and $\pm c/2$ are the geometry boundaries [11].

The needed "buckling" eigenvalues for Equation 5.17 are given in Equation 5.24 [11].

$$B_n^2 = \begin{cases} 0 & \text{Infinite Medium Geometry} \\ B_x^2 + B_y^2 = \left(\frac{i\pi}{\tilde{a}}\right)^2 + \left(\frac{j\pi}{\tilde{b}}\right)^2 & \text{for } i,j = \text{odd, 2D Geometry} \\ B_x^2 + B_y^2 + B_z^2 = \left(\frac{i\pi}{\tilde{a}}\right)^2 + \left(\frac{j\pi}{\tilde{b}}\right)^2 + \left(\frac{k\pi}{\tilde{c}}\right)^2 & \text{for } i,j,k = \text{odd, 3D Geometry} \end{cases} \tag{5.24}$$

Recall that the source is a uniform source in the infinite medium geometry, a line source in the 2D geometry, or a point source in the 3D geometry. Computing the integral in Equation 5.21 and inserting the solution for $S_n(u)$ into Equations 5.18 yields the final solution for $q_n(u)$ for the three geometry cases.

$$q_n(u) = \begin{cases} S_0 & \text{for } n = 0\text{, Infinite Medium Geometry} \\ \frac{4}{\tilde{a}\tilde{b}} S_0 e^{-\int_{u'}^{u} du'' \alpha_n(u'')} & \text{2D Geometry} \\ \frac{8}{\tilde{a}\tilde{b}\tilde{c}} S_0 e^{-\int_{u'}^{u} du'' \alpha_n(u'')} & \text{3D Geometry} \end{cases} \tag{5.25}$$

The slowing down density can now be simply calculated using $q(\vec{r}, u) = \sum_n q_n(u)\psi(\vec{r})$. Using the definition for slowing down density given in Equation 5.8, the neutron flux solution can be computed.

The big assumption in the CSDA solution is that neutrons slow down continuously such that there are no jumps in energy. This CSDA assumption is relatively correct in the slowing down region, but is completely inaccurate in the thermal energy range. This is because thermal neutrons achieve thermal equilibrium with the background media allowing them to up-scatter which is characterized by a Maxwellian distribution. For 2D and 3D geometries, the CSDA solution does not account for uncollided flux since CSDA assumes that particles collide as soon as they move in order to continuously slow down. This error becomes more severe where significant streaming occurs (relative low scatter cross-section). The coding language MATLAB was utilized to perform the CSDA calculations for the infinite medium, 2D, and 3D geometry problems.

5.2 MCNP

MCNP is a general purpose Monte Carlo code developed and maintained at Los Alamos National Laboratory. MCNP is a well recognized and widely used code for neutron, photon, and electron transport. MCNP has undergone extensive verification and validation testing and is well documented. Unlike deterministic methods where the transport equation (or an approximation of it) is solved, MCNP uses Monte Carlo which is a stochastic method. Monte Carlo works by simulating individual particles' paths and interactions through a medium. Many particles are simulated and the average behaviour of some desired aspect, such as neutron flux, is tallied [32].

In Monte Carlo, a particle is tracked from source throughout its life to its death. As a particle is tracked, each step of its life is randomly sampled from probability distributions using particle transport data. These distributions include the energy and direction of a particle born from a source, the distance a particle travels between collisions with the medium, the interaction that occurs in a collision, and the scattering angle and energy loss of the particle if scattering occurred in the collision. Additional particles can be born from an interaction which are then also tracked until death [32]. The average behaviour of the tracked particles in the physical system is then inferred using the central limit theorem. The central limit theorem states that the mean of sufficiently large independent random variables will be approximately normally distributed [20].

The following math outlines the fundamental formulation of the Monte Carlo method. For simplicity, a simple slab geometry case will be assumed. First lets introduce two simple concepts. A probability density function (PDF), $p(x_s)$, is the probability of x assuming a value within $[x_s, x_s + dx]$. PDFs are always non-negative and are normalized such that they vary from 0 to 1. A cumulative density function (CDF), $P(x_s)$, is the probability of x not exceeding x_s. $P(x_s)$ is the integral of $p(x)$ from the minimum x value up to x_s. CDFs are always non-negative and are non-decreasing functions from 0 to 1. A CDF can be randomly sampled using a randomly generated number, η, from 0 to 1 [20].

Consider a neutron particle with energy E in the slab at position x_n. The first variable sampled would be the distance the neutron travels until a collision occurs. The probability of no collision in distance r will be $e^{-\sigma_t(E)r}$. Additionally, the probability of collision in a distance dr is $\sigma_t(E)dr$. Using these two terms, a probability density distribution function can be written:

$$p(r)dr = \sigma_t(E)e^{-\sigma_t(E)r}dr \tag{5.26}$$

The CDF for a distance r_s is obtained by integrating the PDF.

$$P(r_s) = \int_0^{r_s} dr\,\sigma_t(E)e^{-\sigma_t(E)r} = 1 - e^{-\sigma_t(E)r_s} = \tilde{\eta} \tag{5.27}$$

The position r_s corresponding to the random number η would be:

$$r_s = -\frac{\ln(1-\tilde{\eta})}{\sigma_t(E)} = -\frac{\ln(\eta)}{\sigma_t(E)} \tag{5.28}$$

In Equation 5.28, the replacement $\eta = 1 - \tilde{\eta}$ can be made since both are random numbers from 0 to 1 [27].

The position of the neutron would be calculated as follows:

$$x_n = x_{n-1} + r_s\mu_{ang} \tag{5.29}$$

In Equation 5.29, x_{n-1} is the previous x-coordinate and $\mu_{ang} = \cos\theta$ where θ is the angle of the direction of travel relative to the x-axis.

Next, the type of reaction must be sampled. The probability of absorption in a collision will be:

$$p(x_a) = \frac{\sigma_a(E)}{\sigma_t(E)} \tag{5.30}$$

Similarly, the probability of scattering in a collision will be:

$$p(x_s) = \frac{\sigma_s(E)}{\sigma_t(E)} = 1 - \frac{\sigma_a(E)}{\sigma_t(E)} = 1 - p(x_a) \tag{5.31}$$

Taking a random number, η, the neutron reaction will be as given in Equation 5.32 [27]:

$$\eta \begin{cases} \leq \frac{\sigma_a}{\sigma_t}, & \text{absorption occurs} \\ > \frac{\sigma_a}{\sigma_t}, & \text{scattering occurs} \end{cases} \tag{5.32}$$

If scattering occurs, the scattering direction must be sampled. This requires sampling of two separate angles as shown in Figure 5.14. The PDF for scattering angle,

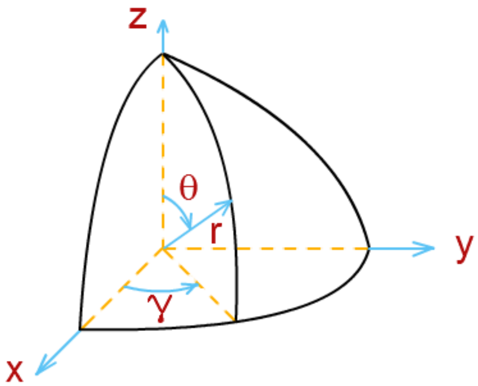

Figure 5.14: Spherical Coordinates.

$\mu_0 = \cos(\theta)$, can be expressed with:

$$f(\mu_0)d\mu' d\gamma = \frac{\sigma_s(\mu_0, E)d\mu' d\gamma}{\sigma_s(E)} \tag{5.33}$$

Integrating Equation 5.33 over γ yields:

$$\int_0^{2\pi} f(\mu_0)d\mu_0 d\gamma = 2\pi \frac{\sigma_s(\mu_0, E)d\mu_0}{\sigma_s(E)} = p(\mu_0)d\mu_0 \tag{5.34}$$

The CDF for specific scattering angle $\mu_{0,s}$ is calculated in Equation 5.35.

$$P(\mu_{0,s}) = \eta = \int_{-1}^{\mu_{0,s}} p(\mu_0)d\mu_0 = \frac{2\pi}{\sigma_s(E)} \int_{-1}^{\mu_{0,s}} \sigma_s(\mu_0, E)d\mu_0 \tag{5.35}$$

For simplicity, lets consider isotropic scattering.

$$\sigma_s(\mu_0, E) = \frac{1}{4\pi}\sigma_s(E) \tag{5.36}$$

Using isotropic scattering, the CDF simplifies to Equation 5.37.

$$P(\mu_{0,s}) = \frac{1}{2}(\mu_{0,s} + 1) = \eta \tag{5.37}$$

The sampled scattering angle $\mu_{0,s}$ is given in Equation 5.38 [27]:

$$\mu_{0,s} = 2\eta - 1 \tag{5.38}$$

The PDF for scattering angle γ is simply:

$$p(\gamma)d\gamma = k d\gamma = \frac{1}{2\pi}d\gamma \tag{5.39}$$

where $k = \frac{1}{2\pi}$ is a constant because each angle has equal probability of occurring within the range $[0, 2\pi]$. The CDF for specific scattering angle γ_s is shown in Equation 5.40.

$$P(\gamma_s) = \int_0^{\gamma_s} p(\gamma) d\gamma = \frac{1}{2\pi} \int_0^{\gamma_s} d\gamma = \frac{\gamma_s}{2\pi} = \eta \tag{5.40}$$

The scattering angle γ_s is sampled using Equation 5.41 [27].

$$\gamma_s = 2\pi\eta \tag{5.41}$$

After scattering, this process is repeated with the free flight distance and then the reaction type being sampled. This continues until the particle is lost either from absorption or leakage. MCNP6 models 3D geometry and will take into account additional effects such as anisotropic scattering, $S(\alpha, \beta)$ thermal treatment, production of additional particles, and more. However, the same concept applies that was shown in the above derivations. Although neutron transport was used in this research, MCNP is also capable of the transport of photons, electrons, protons, and various heavy charged particles along with coupled neutron/photon/electron/heavy charge particle transport.

One advantage of MCNP6 is that continuous energy cross-section libraries can be sampled while deterministic codes typically utilize multi-group cross-sections. The primary sources of nuclear data for MCNP6 are from the Evaluated Nuclear Data File (ENDF) system, Advance Computational Technology Initiative (ACTI), the Evaluated Nuclear Data Library (ENDL), Evaluated Photon Data Library (EPDL), the Activation Library (ACTL), and data evaluations from the Nuclear Physics (T-16) group at Los Alamos National Laboratory. Los Alamos National Laboratory developed code, NJOY 2012, is utilized to format the evaluated data into an appropriate form for MCNP [22,32].

Being a statistical process, there is statistical error in the recorded averages. The relative precision of a Monte-Carlo tally will scale as follows:

$$R = C/\sqrt{N} \tag{5.42}$$

where R is the relative error, C is a constant depending on the specified geometry and tally, and N is the number of simulated particles. Thus in order to reduce the error by 50%, 4 times more particles must be simulated. For a given MCNP job, the required computer time, T, is proportional to N:

$$R = C/\sqrt{T} \tag{5.43}$$

The two methods of reducing the error are either using more computer time (simulate more particles) or somehow reduce C. MCNP has developed variance reduction techniques used for decreasing C. The simplest variance reduction method is to truncate the simulated geometry where it does not contribute significantly to the solution. Another commonly used variance reduction technique is particle splitting and russian roulette. In regions of more importance, a particle will be split into additional particles that are tracked. The "weight" of the particle is adjusted accordingly to prevent an unbiased solution. Similarly for regions of less importance, a fraction of the particles will be killed while the remaining particles will have an increased "weight". Other variance reduction techniques include energy splitting/roulette, time splitting/roulette, source direction biasing, and others. When used properly these variance reduction techniques can reduce the required computation time [32].

MCNP is capable of tallying many quantities. MCNP tallies are given in a quantity per source particle (SP) and thus must be normalized with the desired source strength. The tally of interest for this research was the F4 tally. The F4 tally is the average flux in a cell with units $[\# particles/(cm^2 \cdot SP)]$. Suppose a particle with weight W and energy E has a track-length T within a specified tally volume V. This particle makes a WT/V contribution to the flux in the cell. The F4 tally sums all the particles contributions within a specified volume [28].

One weakness of MCNP is when the tally region of interest is located many mean free paths away from the particle source. Since MCNP is a statistical process, the more particles that are tallied in a specific region, the more the relative error will be reduced. For example, in our 2D and 3D problems of interest, a neutron flux result will have larger relative error the farther it is away from the center line or point source. The previously described variance reduction techniques can be used to alleviate some of this deficiency.

5.3 PDT

PDT is a massively parallel discrete ordinates deterministic transport code developed and maintained at Texas A&M University. The origin of PDT traces back to 1998 when funding was obtained through the Advance Simulation and Computing (ASC), Office of Defense campaign of the NNSA, under its Academic Strategic Alliances Program (ASAP) [26]. PDT capabilities have dramatically improved over the years. PDT includes solvers for neutronics, gamma transport, radiative transfer, and charged-particle transport problems. This section will give a quick overview of

PDT methods and capabilities.

In PDT, energy is discretized using multigroup method. In multigroup method, the energy range is divided into G intervals. Standard notation defines group $g = 0$ as the highest energy group. The subsequent energy groups are at decreasing energy up to group $g = G$, for the lowest energy group. Angular group flux is defined as the angular flux integrated over the energy group interval:

$$\psi_g\left(\vec{r}, \vec{\Omega}, t\right) = \int_{E_g}^{E_{g-1}} dE\, \psi\left(\vec{r}, \vec{\Omega}, E, t\right) \tag{5.44}$$

Neutron cross-sections must be approximated into energy-averaged cross-sections. Energy averaged cross-sections are shown in Equations 5.45 and 5.46 [11].

$$\sigma_{t,g} = \frac{\int_{E_g}^{E_{g-1}} dE\, \sigma_t(E)\phi(\vec{r}, E, t)}{\int_{E_g}^{E_{g-1}} dE\, \phi(\vec{r}, E, t)} \tag{5.45}$$

$$\sigma_{x,g'\to g}(\vec{\Omega}' \to \vec{\Omega}) = \frac{\int_{E_g}^{E_{g-1}} dE \int_{E_{g'}}^{E_{g'-1}} dE'\, \sigma_x(E' \to E, \vec{\Omega}' \to \Omega)\phi(\vec{r}, E', t)}{\int_{E_{g'}}^{E_{g'-1}} dE'\, \phi(\vec{r}, E', t)} \tag{5.46}$$

NJOY 2012 was utilized to computed the required group cross-sections. The multigroup neutron transport equation is obtained by integrating the neutron transport equation, Equation 2.18, over the gth energy interval and substituting in the definitions for the energy averaged cross-sections. The multigroup neutron transport equation in shown in Equation 5.47 [11].

$$\vec{\Omega} \cdot \nabla\psi_g\left(\vec{r}, \vec{\Omega}\right) + \sigma_{t,g}\psi_g\left(\vec{r}, \vec{\Omega}\right) = \int_{4\pi} d\Omega' \sum_{g'=1}^{G} \sigma_{s,g'\to g}\psi_{g'}\left(\vec{r}, \vec{\Omega}\right) + S_{ext,g}(\vec{r}, \vec{\Omega}) \tag{5.47}$$

With the multigroup method, approximating the cross-sections as shown in Equations 5.45 and 5.46 will introduce discretization error into the solution. As the energy intervals get smaller (i.e. G increases), this error will be reduced. The energy range should not be divided up equally. Instead, the thermal region, slowing down region, and fast energy region should be considered separately. For the thermal region, energy groups of similar width should be used to accurately capture the Maxwellian spectrum because the actual neutron distribution is nearly Maxwellian in this range in many problems of interest. In the slowing down region, the flux often has an energy dependence that is almost proportional to 1/E. In this region, energy groups can be best broken up using an equal number of groups per energy decade (logarithmic spacing in energy, or equal spacing in lethargy). Last, in the fast energy range, there will be cross-section resonances in the cross sections of nuclides with low to intermediate atomic weight, such as the carbon and oxygen in many problems addressed in the present work. The graphite cross-section resonances are seen for energies above 1 MeV in Figure 5.1. A well designed energy group set would use additional groups with smaller energy widths where resonances are located in order to obtain accurate group cross-sections. The accuracy of the multigroup approximation depends on the number energy regions and on how well the spectrum used for averaging matches the spectrum in the actual problem.

PDT allows users to coallesce energy groups into data structures called group sets where the grouping can be as fine as every energy group having its own group set or as coarse as all energy groups gathered into one group set. Group sets have two main purposes. First, group sets can speed up computation time, for example by placing all thermal energy groups into one group set and ignoring upscattering between group sets during the transport sweep. Second, group sets allow different quadrature sets to be utilized for different energy groups, which is crucial in efficiently resolving ray effect anomalies often seen in discrete ordinate solutions, mostly in the higher energy groups.

PDT uses discrete-ordinates (S_N) to discretize the angle or direction. S_N method approximates the angular integrals using a variety of choices for the quadrature set. A quadrature set is a set of weights, w_m, and directions (ordinates), $\vec{\Omega}_m$, used to approximate the angular integrals in the transport equation [16, 19]:

$$\phi(\vec{r}, E, t) = \int_{4\pi} d\Omega\, \psi\left(\vec{r}, \vec{\Omega}, E, t\right) \approx \sum_{m=1}^{N_{dir}} w_m \psi_m\left(\vec{r}, \vec{\Omega}\right) \tag{5.48}$$

In Equation 5.48, N_{dir} is the number of angular directions. The multigroup S_N transport equation for specific energy group g and angular direction m is given in Equation 5.49 [33].

$$\vec{\Omega}_m \cdot \nabla + \sigma_{t,g}\psi_{m,g}(\vec{r}) = \sum_{g'=1}^{G}\sum_{n=0}^{N} \frac{2n+1}{4\pi}\sigma_{s,n,g'\to,g} \sum_{k=-n}^{n} \phi_{g'}^{k,n} Y_{k,n}(\vec{\Omega}_m) + S_{ext,m,g}(\vec{r}) \tag{5.49}$$

In Equation 5.49, the group scattering term has been expanded using Legendre polynomial expansion. Y_{kn} are spherical harmonics which were given in Equation 2.36. See Chapter 3 in *Nuclear Reactor Theory* by George Bell and Samuel Glasstone for more information regarding Legendre polynomial expansion of the neutron transport equation [7].

With the S_N method in 3D geometry, each direction is described using direction of cosines as shown in Figure 5.15. Since $\hat{\Omega}$ is a unit vector, the following condition must be satisfied.

$$\mu^2 + \eta^2 + \xi^2 = 1 \tag{5.50}$$

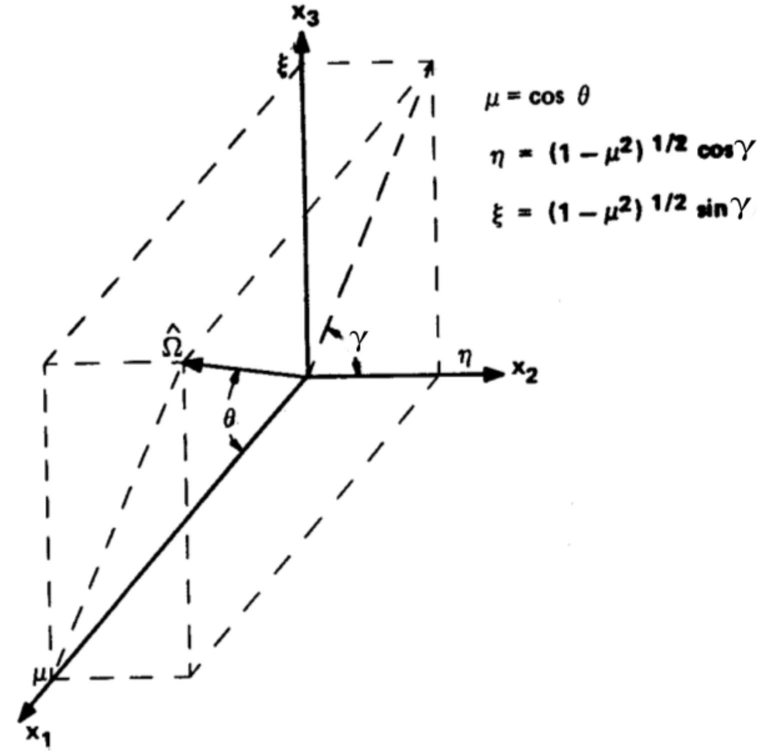

Figure 5.15: Angular Coordinate System [20].

There are many quadrature sets that have been developed and applied towards neutron transport problems. One popular quadrature set used in transport problems is level symmetric (LS) quadrature sets. In a S_N LS quadrature set, the same set of $N/2$ positive values of the direction cosines are used for each axes (μ, η, ξ) [20]. In other words, the set of directions is rotationally symmetric about each axes. The LS quadrature will have $N(N+2)/8$ ordinates per octant. An example of a S_{16} LS quadrature set is shown in Figure 5.16 [16]. Other common quadrature sets include Gauss-Chebyshev quadrature sets and Quadruple Range quadrature sets. Each quadrature set will have limitations. For example, after 55 directions in a octant, the LS quadrature sets will contain negative weights which can lead to a unphysical non-smooth angular flux solution. See *Discrete-Ordinates Quadrature Sets Based on Linear Discontinous Finite Elements* by Joshua J. Jarrell and Marvin L. Adams or *Discrete-Ordinates Quadratures Based on Linear and Quadratic Discontinuous Finite Elements Over Spherical Quadrilaterals* by Cheuk Y. Lau and Marvin L. Adams for more in depth detail regarding common quadrature sets used in S_N transport problems [16, 19].

S_N methods suffer an undesirable phenomena known as ray effects when the angular variables are under resolved. Ray effects are spatial oscillations in the neutron flux solution due to the discrete nature of the angular approximation. In discrete ordinate methods, particles travel along certain directions or rays. Thus the flux will be greater along these allowed directions connecting a source to a point and lower where there are fewer directions connecting a source to a point. The ray effects will become less dominant in mediums where significant scattering occurs since the uncollided flux from a neutron source along these allowed quadrature directions become less dominant. In other words, ray effects become more dominant in scenarios

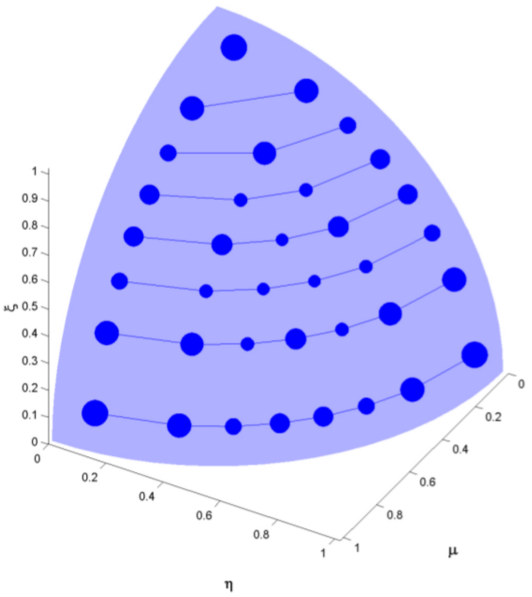

Figure 5.16: Level Symmetric LS_{16} Quadrature Set [16].

where significant streaming occurs [10]. Since the neutron scattering cross-section in graphite is larger at thermal energies and lower at fast energies, the ray effects will be more dominant at higher neutron energies in graphite. Thus more quadrature directions will be needed in the fast neutron energy groups. As described in the Methods Section, an independent angular analysis was performed in various energy ranges in order to compute the solution's angular sensitivity in different energy ranges.

In each spatial cell, each iteration employs a "sweep" along each of the discrete ordinates, or angular directions, requested in a quadrature set. For each angular direction, a sweep begins at the spatial boundary where the incident angular flux is specified by a boundary condition. The exiting angular flux is then computed which then becomes the boundary condition for the neighboring cells. For specific angles and cells, the exact formulation of the exiting flux depends on the spatial discretization method [30].

Currently PDT uses piecewise linear discontinuous (PWLD) finite-element method (FEM) for the spatial discretization of arbitrary polygonal (2D) or polyhedral (3D) cells. PWLD FEM is a numerical technique that utilizes discontinuous basis functions to describe the spatial dependence of the solution [6]. Compared to standard FEMs, discontinuous FEMs have the advantage of relaxed continuity at inter-element boundaries. This allows decoupling of the local individual cell problems from the global problem. As result, no global matrix assembly is required reducing the in-core memory demand. This local formulation also makes it easier for parallel algorithms to be utilized [21]. In standard PWLD FEM, the multigroup SN neutron transport equation, Equation 5.49, is multiplied by a test function, w, and integrated over the spatial domain. The transport solution is then expanded in terms of the finite element basis functions, $b_j(\vec{r})$.

$$\psi_m^g(\vec{r}) = \sum_j^N \psi_{m,j}^g b_j(\vec{r}) \tag{5.51}$$

Piecewise linear describes the specific type of basis function employed. Other basis functions such as linear discontinuous FEM on triangle and tetrahedral meshes, bilinear discontinuous FEM on quadrilateral meshes, and tri-linear discontinuous FEM on hexahedra meshes have all shown to be computationally efficient. However, these methods can only be used for their specific grid types when the problem requires the method to satisfy the diffusion limit. Another method is Wachspress discontinuous FEM, which utilizes rational-polynomial basis functions that can be does satisfy the diffusion limit for most polygonal and polyhedral meshes. The Wachspress method has the advantage of its Galerkin FEM formulation yielding a symmetric positive definite matrix. However, the Wachspress method has the major disadvantage of requiring the integrals of the basis functions to be solved numerically, which results in significant computational expense. In comparison, PWLD FEM which was developed by Stone and Adams [29] has been shown to perform well in the diffusion limit on arbitrary polygonal and polyhedral cells. In addition, PWLD FEM integrals are simple to compute analytically and its Galerkin formulation results in a symmetric positive definite matrix [5].

Lets consider the Galerkin method, where the test and basis functions span the same space in every cell. Piece-wise linear basis functions are designed to linearly interpolate functions on arbitrary polygonal (2D) or polyhedral (3D) cells. Lets first consider the 2D polygonal case. To build the basis functions, the polygonal cell is first divided into subcells called sides. A side is created by choosing and connecting a center point to two adjacent vertices forming a triangle. Figure 5.17 shows an example of a side in a hexagonal cell [5, 29].

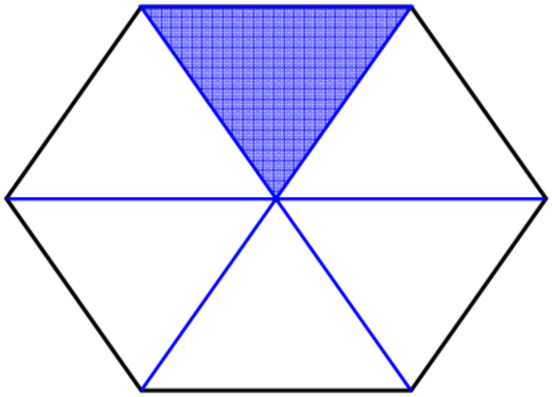

Figure 5.17: A Side (Shaded Triangle) within a 2D Hexagonal Cell [5]

The general mathematical form of the 2D PWL basis functions for cell c and vertex

i is given in Equation 5.52.

$$b_{c,i}(x,y) = t_i(x,y) + \beta_{c,i} t_c(x,y) \tag{5.52}$$

In Equation 5.52, the t functions are standard linear functions such that t_i is equal to 1 at the i-th vertex and decreases linearly to zero at the center and at each cell vertex of each side that touches point i. Similarly, t_c is equal to 1 at the center c and linearly decreases to 0 at each vertex in the cell. β_i are weighting parameters for the cell center points that are defined for each vertex such that the sum of all weighting parameters in a cell is equal to 1.

$$\sum_{i=1}^{N_i} \beta_i = 1 \tag{5.53}$$

In Equation 5.53, N_i is the number of vertices in cell c. The coordinates of c is the weighted average of the vertex coordinates as shown in Equation 5.54.

$$x_c = \sum_{i=1}^{N_i} \beta_i x_i, \quad y_c = \sum_{i=1}^{N_i} \beta_i y_i \tag{5.54}$$

The linear functions t_i and t_c are illustrated in Figures 5.18 and 5.19 respectively. Recall that t_c will be multiplied by the weighting function β_i. Linearly combining these two components, the PWL basis function for vertex i in cell c is obtained as seen in Figure 5.20 [5, 29].

3D PWL basis functions are built similarly to the 2D basis functions. An arbitrary 3D tetrahedral is divided up in sets of subcell volumes, called sides, and linear functions are utilized on each side. In 3D, a side is constructed using two adjacent vertices, a cell center point, and a face center point. An example of a side in a hexahedral

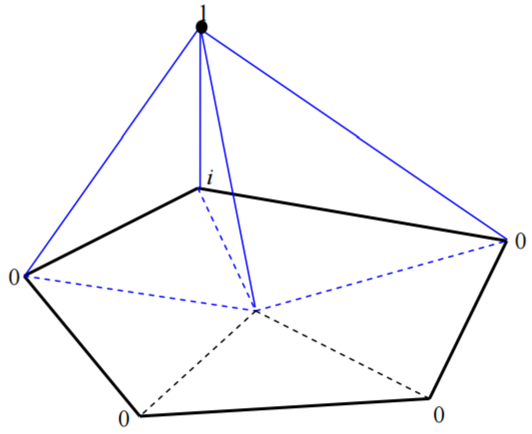

Figure 5.18: t_i Component of the 2D PWL Basis Function $b_{c,i}$ [5]

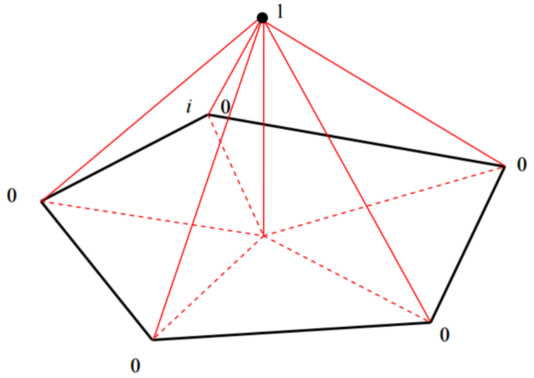

Figure 5.19: t_c Component of the 2D PWL Basis Function $b_{c,i}$ [5]

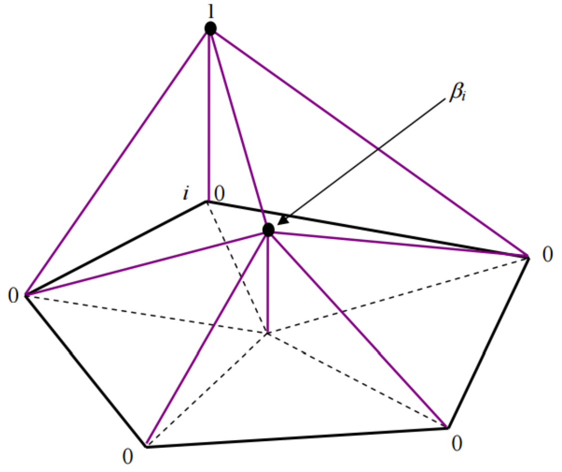

Figure 5.20: 2D PWL Basis Function $b_{c,i}$ for Vertex i in Cell c [5]

cell is given in Figure 5.21. The 3D PWL basis function for vertex i can written as

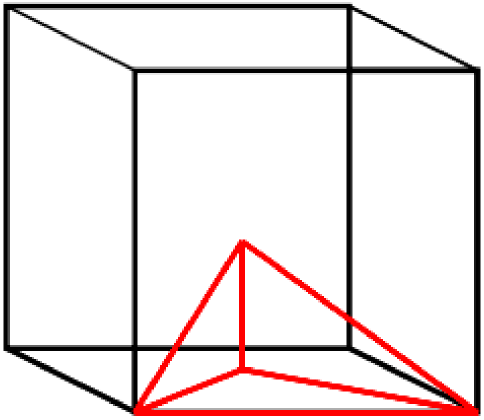

Figure 5.21: A Side within a 3D Hexahedral Cell [5]

follows:

$$b_{c,i}(\vec{r}) = t_i(\vec{r}) + \sum_{faces\,at\,i} \beta_{f,i} t_f(\vec{r}) + \alpha_{c,i} t_c(\vec{r}) \tag{5.55}$$

In Equation 5.55, the t functions are the standard linear functions that are unity at the specified point/vertex and decreases linearly to zero at the neighboring points/vertices. $\alpha_{c,i}$ and $\beta_{f,i}$ are the weights for the cell midpoint and for the face midpoints. The coordinates of the cell midpoint $\vec{r_c}$ and the face midpoint $\vec{r_f}$ are computed as weighted averages of the vertices' weights [5, 29].

$$\vec{r_c} = \sum_{i}^{N_i} \alpha_{c,i} \vec{r_i} \tag{5.56}$$

$$\vec{r_f} = \sum_{i}^{N_f} \beta_{f,i} \vec{r_i} \tag{5.57}$$

Due to the discontinuous nature of the basis functions, there can be discontinuities in the flux solution in both magnitude and slope across the cell boundaries. A more in depth derivation of discontinuous FEM applied to the neutron transport equation can be found in *Discontinuous Finite-Element Transport Solution in the Thick Diffusion Limit in Cartesian Geometry* by Marvin L. Adams [1], in *Adaptive Mesh Refinement Solution Techniques for the Multigroup SN Transport Equation Using a Higher-Order Discontinuous Finite Element Method* by Yaqi Wang [33], and in *The Piecewise Linear Discontinuous Finite Element Method Applied to the RZ and XYZ Transport Equations* by Teresa S. Bailey [5].

In each spatial cell, in order to compute the neutron angular flux, the addition of neutrons from scattering and from fission and other neutron-emitting reactions (when applicable) must be computed. However in order to solve for the scattering and fission source terms, the neutron angular flux is required. PDT solves this problem using a source iteration scheme. For each iteration, the previous iteration flux solution is utilized to compute the current iteration's source term from scattering and fission. This iterative procedure is shown in Equation 5.58 [30].

$$\Omega \cdot \nabla \psi^l + \sigma_t \psi^l = S_S(\psi^{l-1}) + S_F(\psi^{l-1}) + S_{ext} \tag{5.58}$$

In Equation 5.58, l represents the current iteration and S_S and S_F are the scattering and fission source terms respectively. For the first iteration, an initial guess is used for the flux solution. For example, if $\psi^0 = 0$, then the computed ψ^1 would be the uncollided flux of the neturons emitted from the fixed source S_{ext}. Next, ψ^2 would also include the once-collided flux from neutrons scattering once or from a fission event. The convergence for this source iteration scheme can be slow for highly diffusion mediums where neutrons undergo many scattering events before leaking or being absorbed. Part of CERT research is the development of scalable advanced iterative techniques in problems containing highly diffusive regions in order to improve convergence speed. Various iterative algorithms are available in PDT including richardson, generalized minimal residual (GMRES), and conjugate gradient (CG), with or without diffusion-based preconditioners. Derivation, discussion, and analysis of transport-based iterative algorithms can be found in *Fast Iterative Methods for Discrete-Ordinates Particle Transport Calculations* by Marvin L. Adams and Edward W. Larsen [2].

Implicit time discretization is almost always used for time dependent neutron transport calculations due to the very small time scales on which particles traverse computational cells. PDT time discretization options include backward-Euler, Crank-Nicholson, and backward difference formula of order 2 (TBDF-2) [23].

Another research focus of the CERT team is on Adaptive Mesh Refinement (AMR) techniques for space and angle. In a radiation tranport problem, there are often certain regions where higher order of angular quadrature sets and/or finer spatial refinement is needed to reduce the numerical error efficiently. AMR methods in space and angle are being developed by the CERT team. These AMR methods would have the capability of identifying these important regions and implementing additional refinement in angle and space. AMR methods can significantly reduce the computational requirements to meet target accuracies. Angular adaptivty could also resolve a lot of the ray effects that are seen in current S_N methods [33].

Efficient and massively parallel transport sweeps have been developed for PDT which have shown excellent scaling results with more than one million parallel processes.

Figure 5.22 outlines recent PDT scaling results out to 1.5 million parallel processes. This test problem used 3 energy groups, 80 total directions (S8 level-symmetric), and 4096 spatial cells (3D) per parallel process. Additional energy groups and/or discrete angles would lead to even better results. This optimal sweep scalability dispels previous beliefs that transport sweeps cannot scale well past a few thousand cores. Continue optimization is being performed on PDT sweeps. PDT design and initial algorithms have been well verified as part of NNSA PSAAP-1 CRASH project and other projects [3, 4, 13, 26].

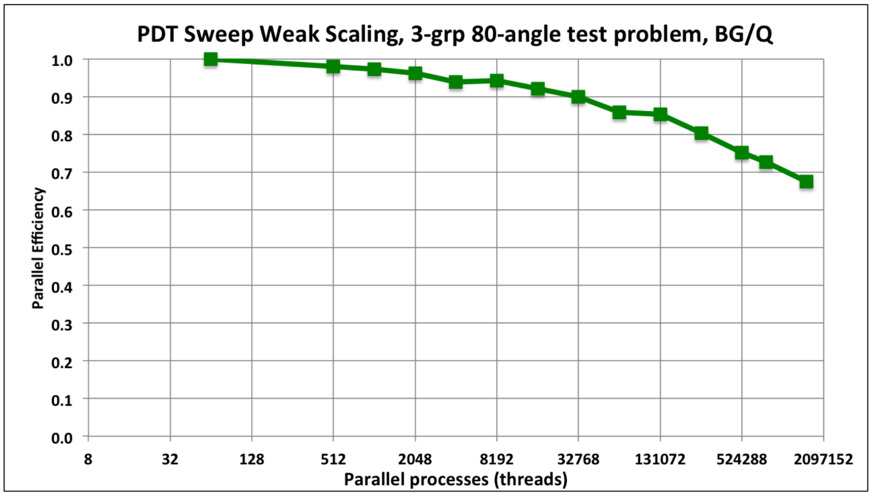

Figure 5.22: PDT Sweep Scalability [14].

There are two kinds of error in the deterministic transport solution. First is the iteration error, which arises from the source iterative algorithm terminating after a finite number of iterations. The second is truncation error, which is an inherent error in discretization from the fact that a continuous variable is represented by a finite number of discrete values [25]. As discussed in the Methods section, the L2 error will be calculated by refining one variable while the other variables are held constant. For example, the number of spatial cells can be increased while the number of energy groups and discrete ordinates are held constant.

The development of PDT to achieve efficient exascale computing of thermal radiative transport problems is a major focus of the CERT project. PDT utilizes the Standard Template Adaptive Parallel Library (STAPL) to employ an architecture-independent execution of its tasks and their interdependencies. STAPL provides parallel data structures and various capabilities for both MPI and multi-threading [8, 9, 12, 31]. Comparison among PDT, MCNP, and CSDA solutions has provided valuable solution verification analysis for CERT and for the further development of PDT.

6. RESULTS

In this section, the PDT discretization error as function of energy, space, and angle resolution is analysed. The discretization error was computed using a L2 error norm given in Equation 4.1.

Recall from the Methods section that a hierarchical approach is taken towards increasingly complex geometry problem sets. The first problem set consists of infinite graphite medium with a uniformly distributed source, which only has energy dependence. The infinite medium geometry is used to compute and analyse the discretization error as function of the energy resolution. The second problem set uses 2D geometry with an approximate infinite line source. The last problem models 3D geometry with an approximate point source. The 2D and 3D geometry problem sets are used to compute the discretization error as function of space and angle resolution.

6.1 Infinite Homogeneous Medium Results

The first set of problems consisted of an infinite graphite medium with a uniform source. AmBe and DT source spectra were considered. In infinite medium geometry, the solution is spatially flat and angularly isotropic. This means that P0 scattering can be used, any quadrature set can be used, and even a single cell with reflecting boundaries can be used to simulate the problem. Since the solution to these problems only have energy dependence, this section outlines the results of the discretization error analysis as function of the energy resolution.

As was discussed in the Methods section, 10 energy group structures were considered with varying numbers of groups in the thermal region, transition region from thermal to slowing down, slowing down region, and fast region. The energy discretization analysis was performed independently in each region. For each region, the number of energy groups were varied in that specific region while keeping constant the number of energy groups in the other energy regions. See Table 4.1 in the Methods section for a breakdown of these energy group structures. Table 4.1 includes energy boundaries for each region along with how many energy groups were used in each region for each group structure. NJOY 2012 was utilized to compute the energy average cross-sections for the tested group structures listed in 4.1. The energy error analysis led to the discovery of several bugs in NJOY 2012. These bugs were submitted to Los Alamos National Laboratory for review, where they were confirmed to be bugs in NJOY. NJOY has been implemented with corrections to the discovered bugs resulting in more accurate energy average cross-sections.

Each PDT solution was compared to the MCNP solution tallied on the same group structure. For example, the 99 group PDT solution is compared to the MCNP solution tallied on the identical 99 group structure. The error between the MCNP and PDT neutron flux solution was computed using the relative L2 error norm whose formula is given in Equation 4.1. The MCNP flux results were obtained with relative statistical errors less than 0.001 for any energy group. The goal of this energy discretization analysis is to investigate how the number of energy groups in each energy region affects the discretization error. A sufficient group set will be constructed based on the energy discretization analysis to use in the following space and angle discretization error calculations in 2D and 3D geometry. The goal of this group set is to minimize the energy resolution error while keeping the number of groups as low as reasonable possible in order to reduce the computational requirements for the 2D and 3D PDT calculations.

6.1.1 Thermal Region

In the thermal region, 0.5 eV was used for the upper energy boundary. The number of thermal groups within this region was varied such that the total number of groups were 73, 99, and 125. The PDT results from the 73, 99, and 125 group structures were compared to the MCNP results. The MCNP results were tallied for those same group structures. The thermal region flux results are shown in Figures 6.1 and 6.2 for AmBe and DT sources respectively. From Figures 6.1 and 6.2 we see that there

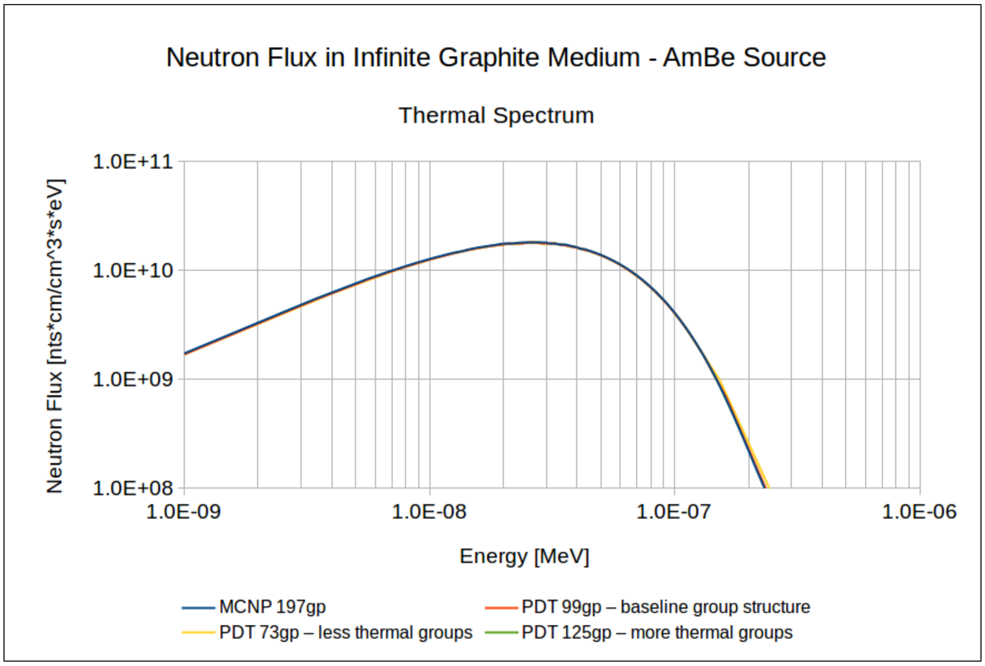

Figure 6.1: Thermal Region Neutron Flux in Infinite Graphite Medium with Uniform AmBe Source.

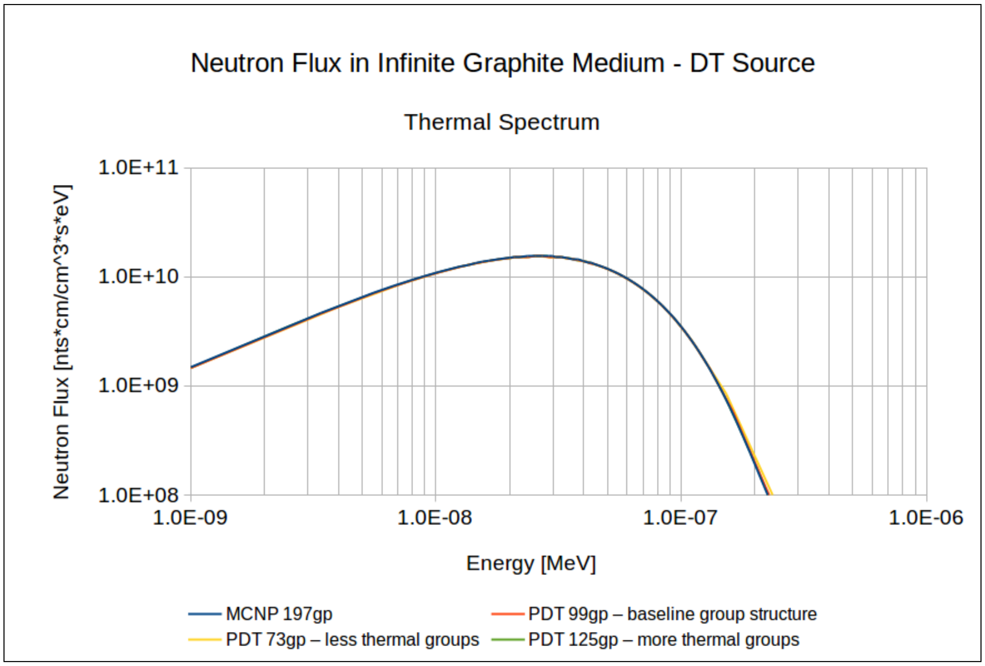

Figure 6.2: Thermal Region Neutron Flux in Infinite Graphite Medium with Uniform DT Source.

are visible differences between the PDT 73 group and the MCNP results where the PDT flux results are greater in the high-energy end of the Maxwellian curve. In comparison, there are very little noticeable differences between the PDT 99 and 125 group results from the MCNP results.

The L2 error calculations, using Equation 4.1, for these group structures are given in Figures 6.3 and 6.4 for the AmBe and DT sources respectively. It is apparent from Figures 6.3 and 6.4 that reducing the number of thermal groups introduced error. However, adding additional thermal groups did not reduce the error. In other words, the 99 group structure contained sufficient number of energy groups in the thermal region.

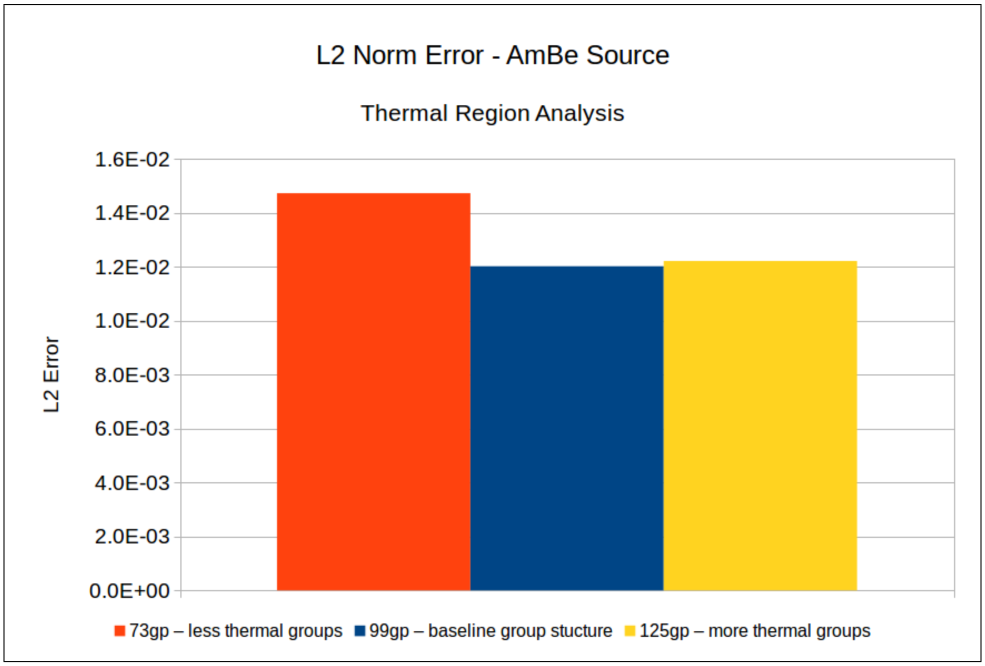

Figure 6.3: Thermal Region L2 Norm Error in Infinite Graphite Medium with AmBe Source.

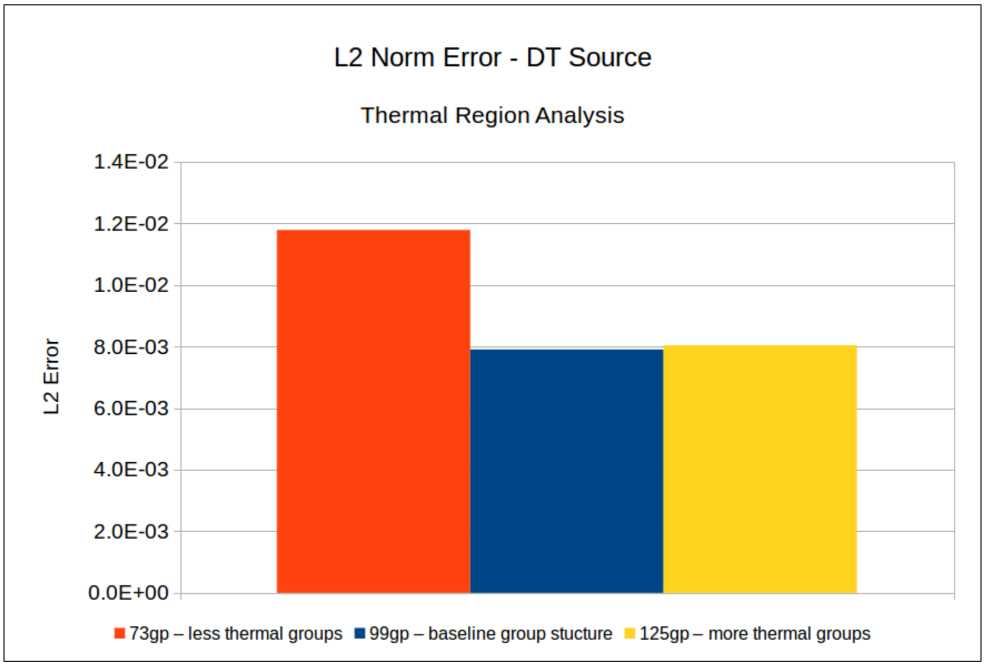

Figure 6.4: Thermal Region L2 Norm Error in Infinite Graphite Medium with DT Source.

6.1.2 Transition Region

The transition region between the thermal region and the slowing down region was found to be between $0.1eV$ and $0.5eV$. In this region, additional energy groups were added to obtain a total number of groups of 107, 115, and 138. Once again, the number of energy groups outside of this transition energy range was held constant. The 99, 107, 115, and 138 PDT group structures were compared to the MCNP results tallied in those same energy group structures. The transition region flux results for the AmBe and DT sources are given in Figures 6.5 and 6.6. The transition region analysis revealed noticeable error when using the PDT 99 baseline group structure. It was found that adding additional transition region groups significantly reduced

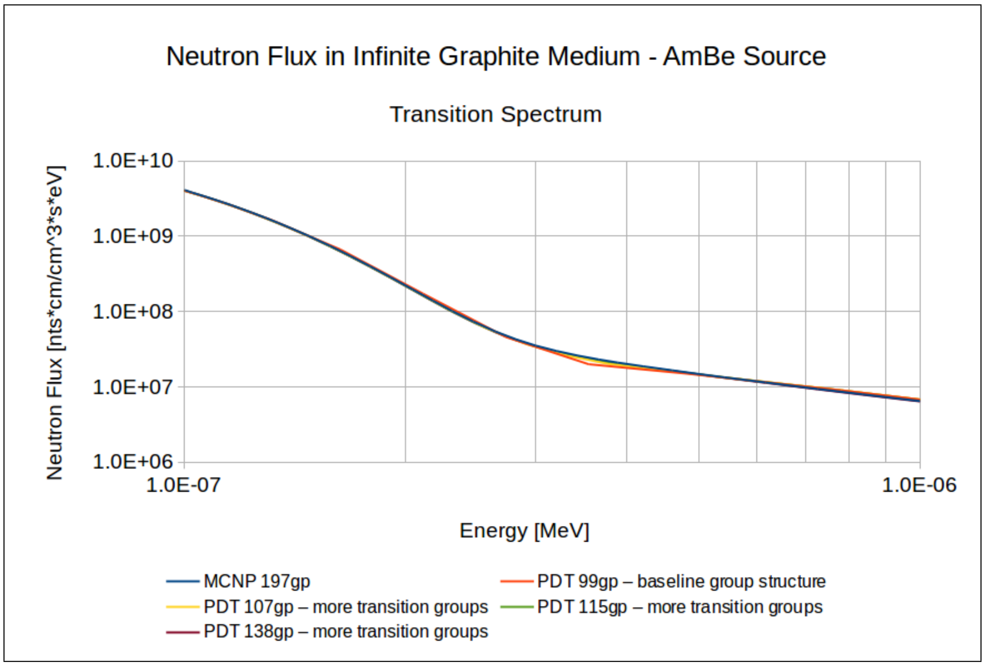

Figure 6.5: Transition Region Neutron Flux in Infinite Graphite Medium with Uniform AmBe Source.

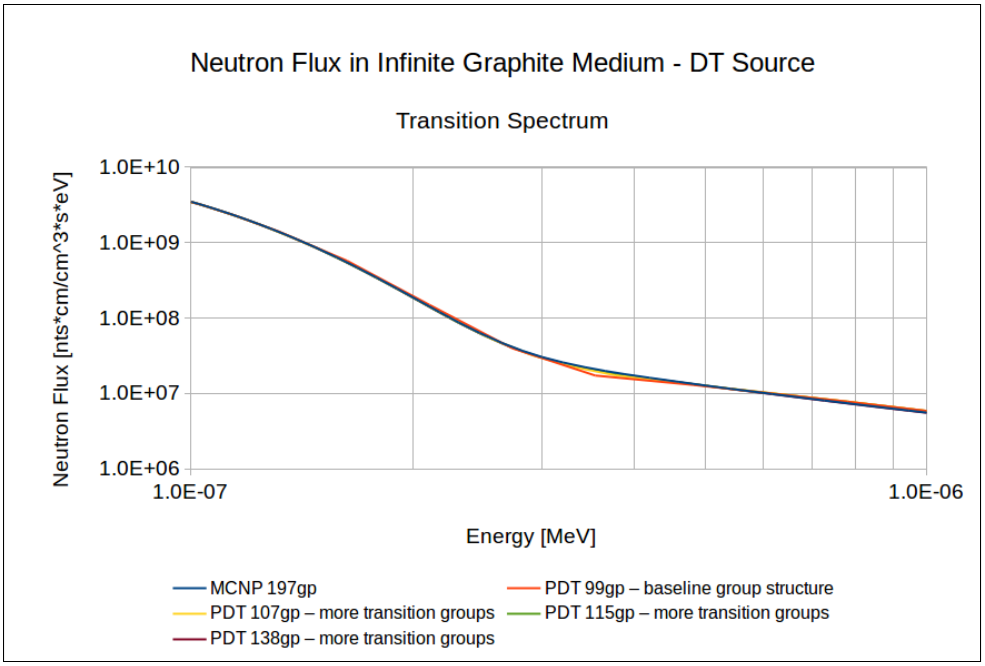

Figure 6.6: Transition Region Neutron Flux in Infinite Graphite Medium with Uniform DT Source.

this error.

The L2 error results for the transition region is shown in Figures 6.7 and 6.8 for the AmBe and DT source spectra respectively. As was also seen in the flux plots, it was found that adding 8 additional transition region groups to the 99 gp baseline structure significantly reduced the error between PDT and MCNP. However, adding additional transition region groups did not significantly further reduce this error. Thus, the 8 additional transition region groups found in the 107 group structure will be included in the optimal energy group structure to be used in the space and angle resolution calculations.

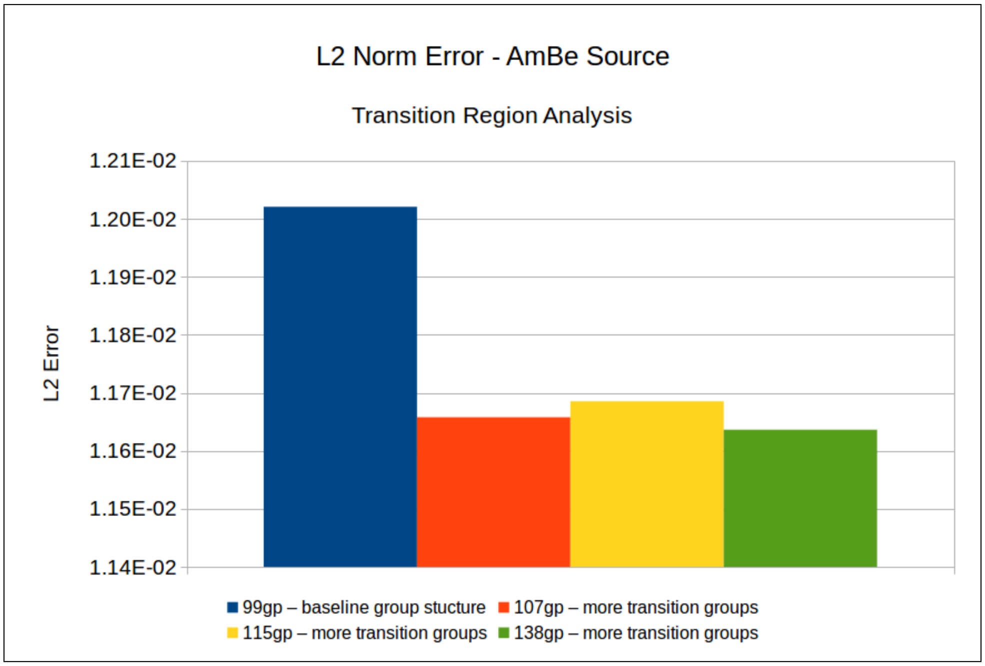

Figure 6.7: Transition Region L2 Norm Error in Infinite Graphite Medium with AmBe Source.

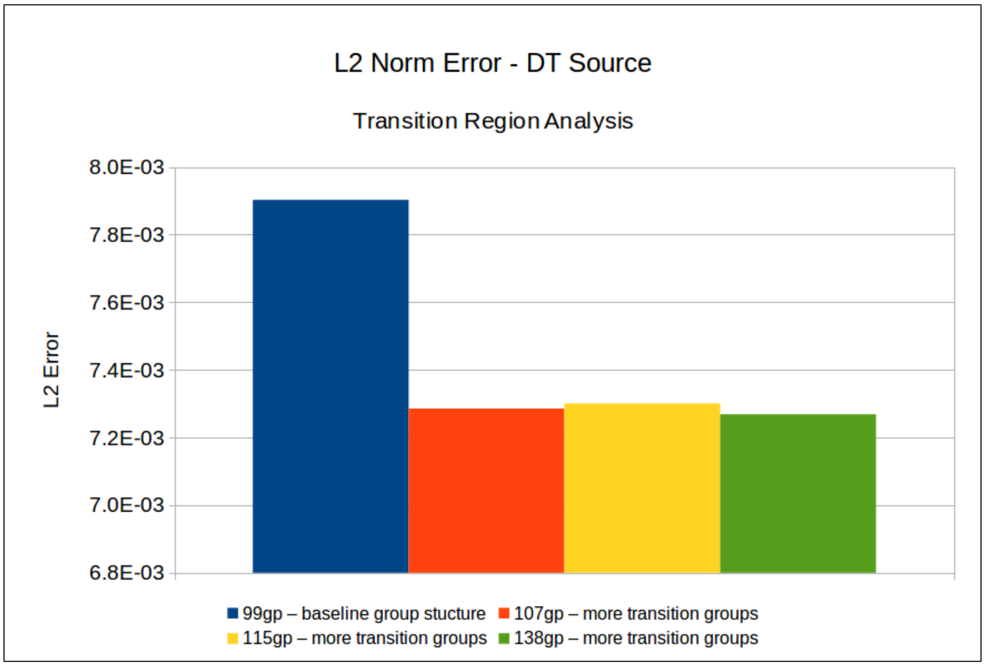

Figure 6.8: Transition Region L2 Norm Error in Infinite Graphite Medium with DT Source.

6.1.3 Slowing Down Region

The slowing down region used a lower energy boundary of 0.5 eV and a upper boundary of 1.0 MeV. Within this region, the number of groups were varied while the number of groups was held constant in the other energy regions. The slowing down region analysis was done using the 87 group structure containing fewer slowing down region groups and the 112 group structure containing additional slowing down region groups compared to the 99 group baseline structure. The neutron flux results in the slowing down region is displayed in Figures 6.9 and 6.10. As seen in Figures 6.9 and 6.10, using fewer slowing down region groups introduced some differences between the MCNP and PDT results. On the other hand, adding additional slowing

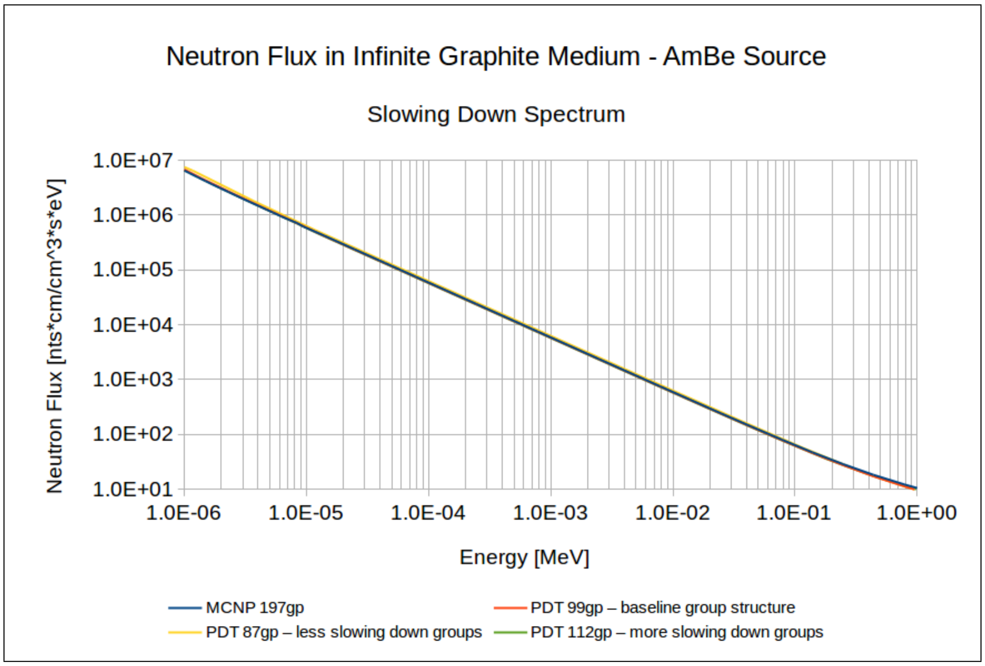

Figure 6.9: Slowing Down Region Neutron Flux in Infinite Graphite Medium with Uniform AmBe Source.

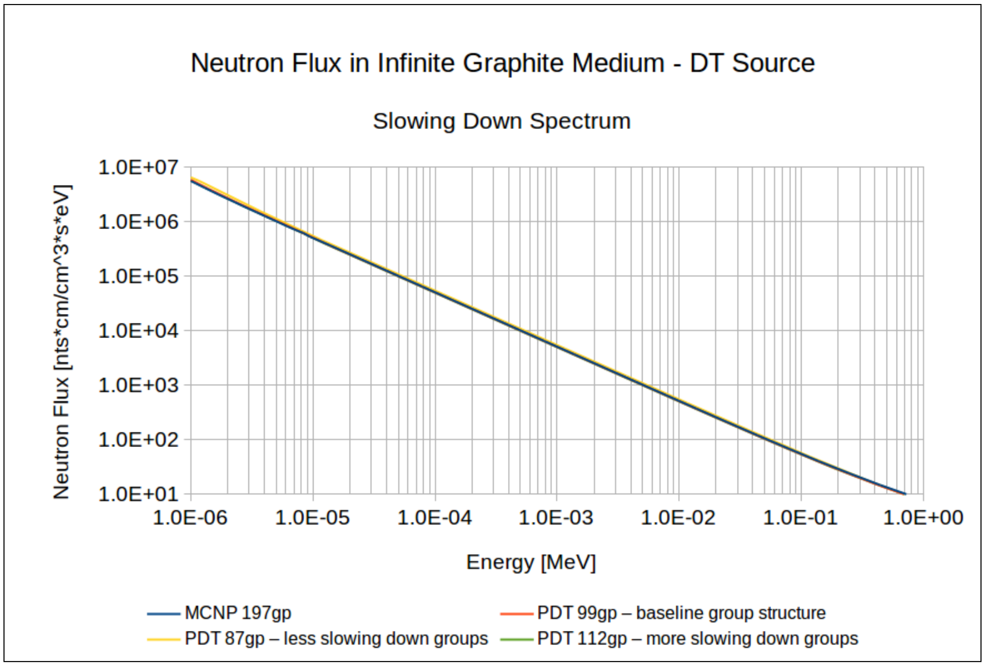

Figure 6.10: Slowing Down Region Neutron Flux in Infinite Graphite Medium with Uniform DT Source.

down region groups did not produce visible differences in the neutron flux solution compared to the 99 group PDT and MCNP results.

The L2 error norm analysis for the slowing down region is given in Figures 6.11 and 6.12. As was noted in the neutron flux figures, using fewer slowing down region groups introduced notable error between PDT and MCNP. Using additional slowing down region groups slightly reduced the L2 error compared to the baseline group structure.

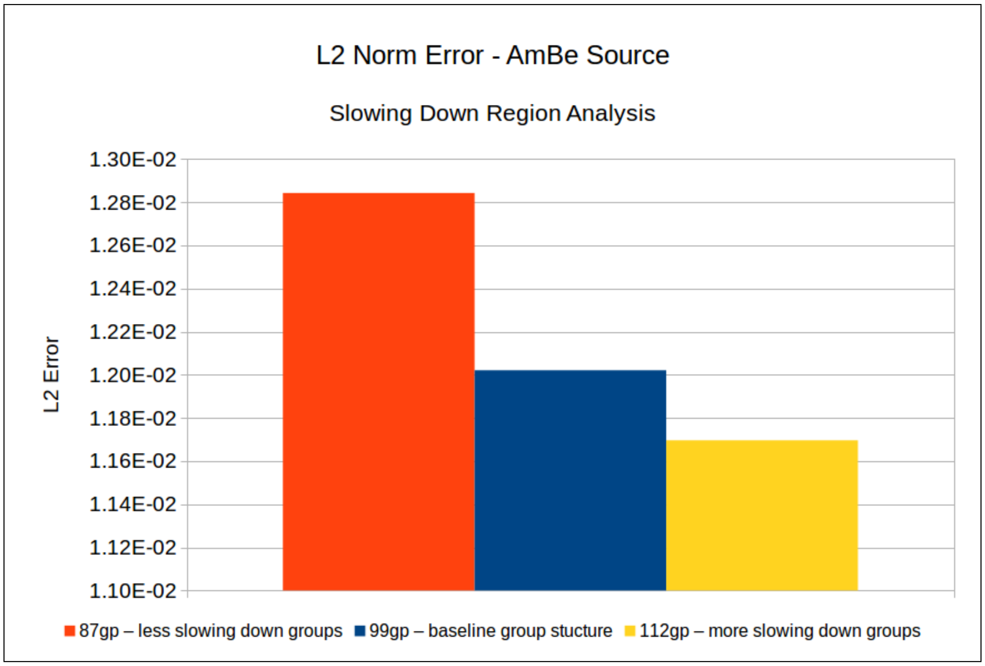

Figure 6.11: Slowing Down Region L2 Norm Error in Infinite Graphite Medium with AmBe Source.

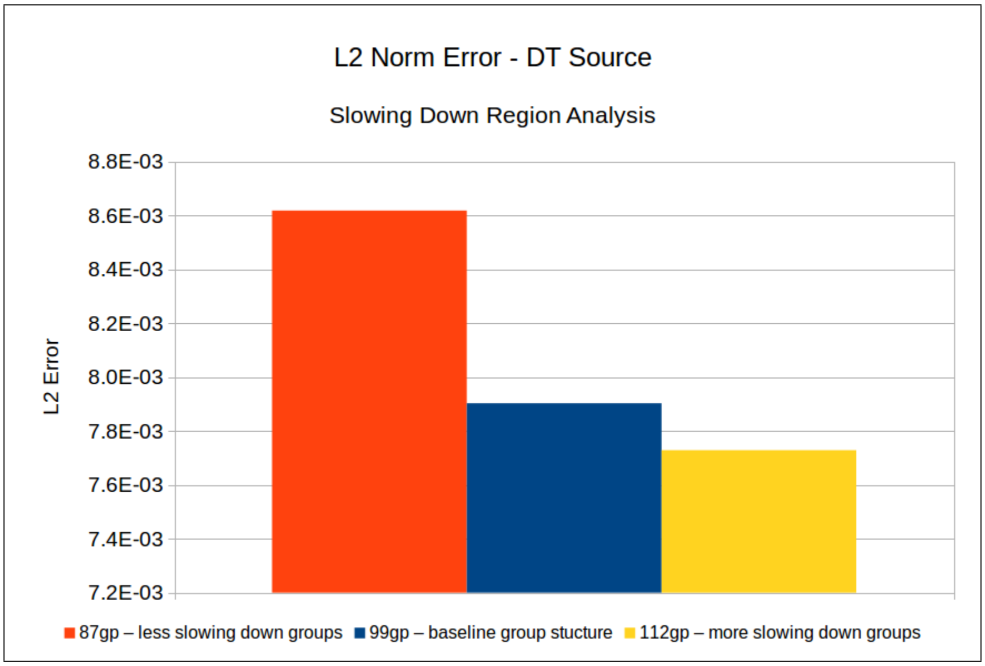

Figure 6.12: Slowing Down Region L2 Norm Error in Infinite Graphite Medium with DT Source.

6.1.4 Fast Region

The fast energy region analysis looked at the solution sensitivity to the number of energy groups above 1.0 MeV. Varying number of fast energy groups, PDT results for 99, 119, and 159 group structures were compared to MCNP results tallied in the same group structures. The fast neutron flux is plotted in Figures 6.13 and 6.14 for the AmBe and DT sources. It is seen in the fast neutron flux figures that the difference between the MCNP and PDT neutron flux reduces with additional fast energy groups.

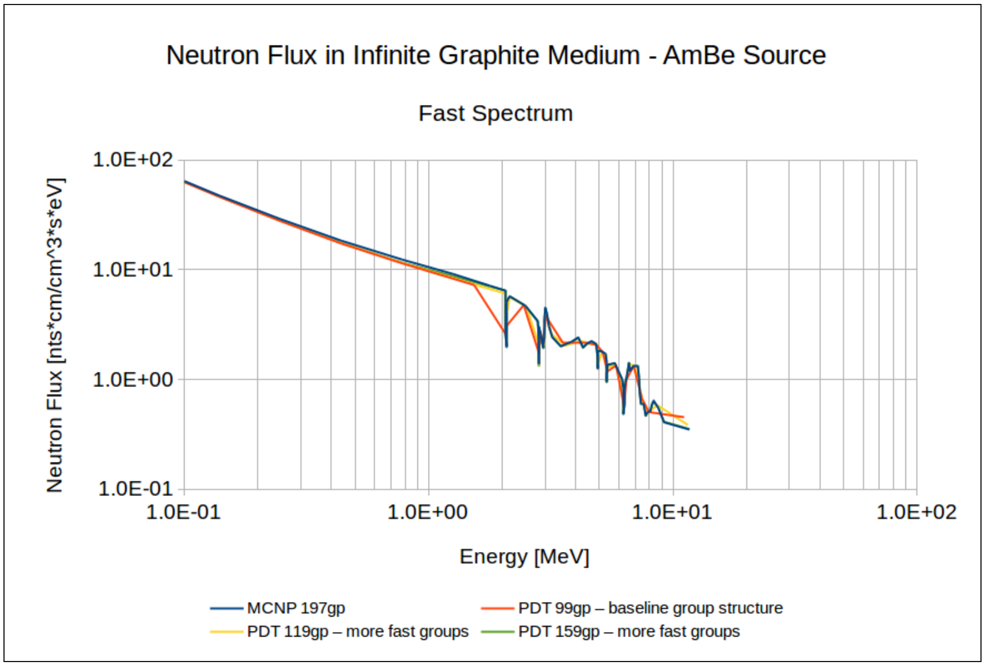

Figure 6.13: Fast Region Neutron Flux in Infinite Graphite Medium with Uniform AmBe Source. Plotted Points are Averages over Energy-Group Intervals Plotted at the Interval Midpoints. The Connecting Straight Line Segments are not Meaningful; only *Points* are.

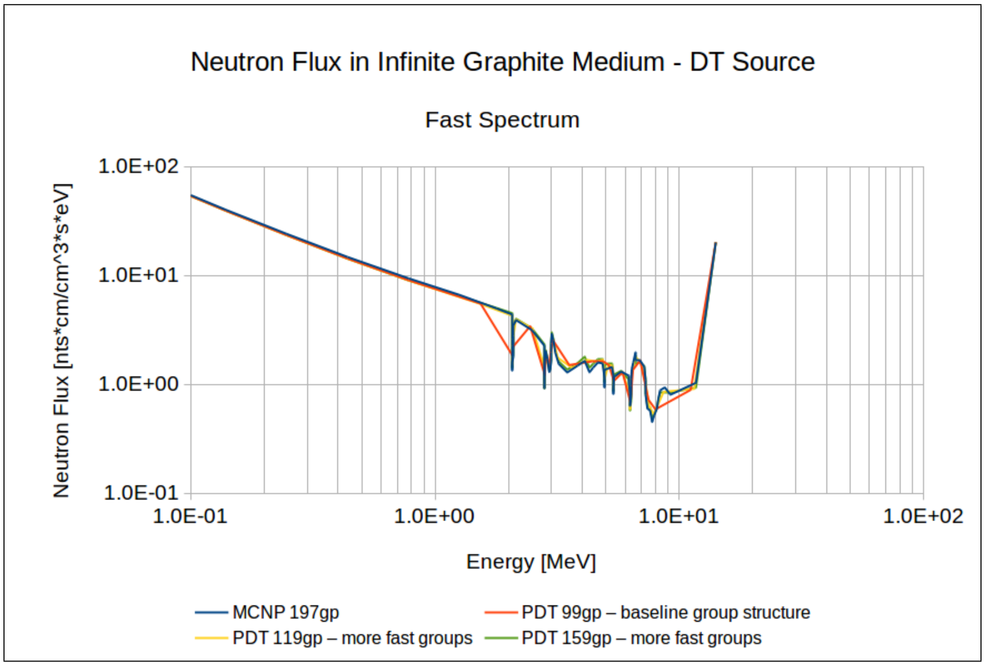

Figure 6.14: Fast Region Neutron Flux in Infinite Graphite Medium with Uniform DT Source. Plotted Points are Averages over Energy-Group Intervals Plotted at the Interval Midpoints. The Connecting Straight Line Segments are not Meaningful; only *Points* are.

The L2 error computations are shown in Figures 6.15 and 6.16. With 20 additional fast energy groups, the L2 error for the 119 group flux is reduced significantly compared to the 99 group structure. The 159 group structure reduces the L2 error further. However, it is apparent that there is less of an error reduction going from 119 to 159 groups compared to going from 99 to 119 groups.

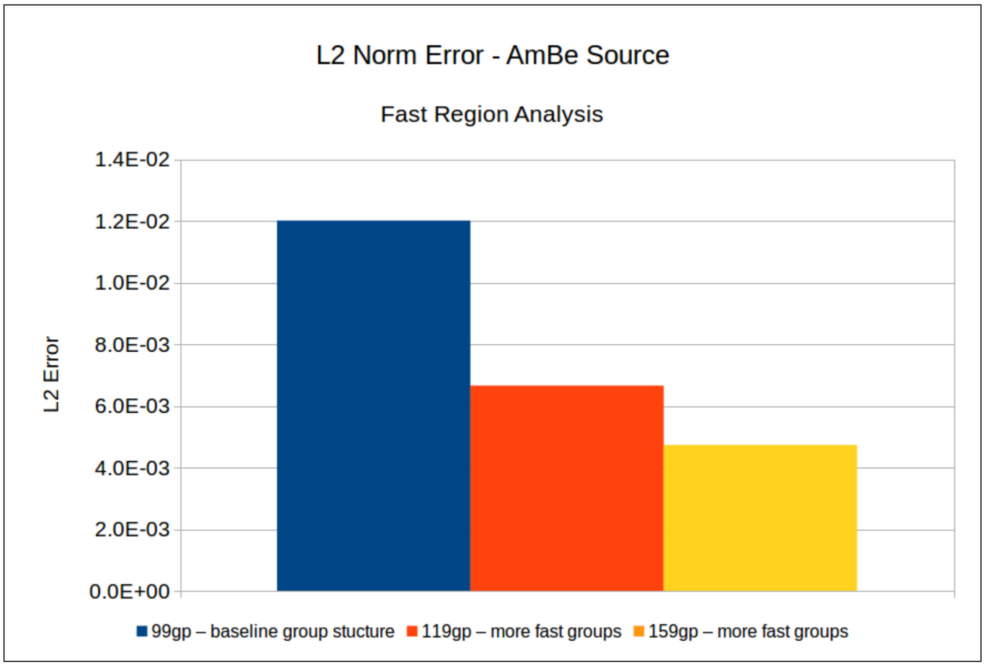

Figure 6.15: Fast Region L2 Norm Error in Infinite Graphite Medium with AmBe Source.

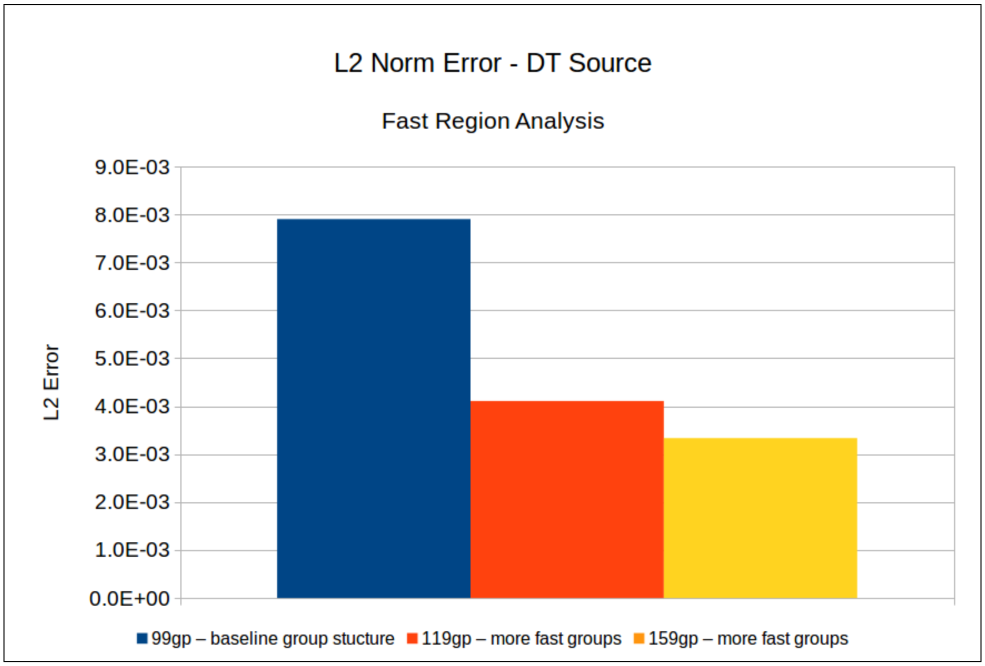

Figure 6.16: Fast Region L2 Norm Error in Infinite Graphite Medium with DT Source.

6.1.5 *Sufficient Group Structure*

Using the results of each energy region analysis, a group structure sufficient for the spatial and angular error analysis was constructed. This group structure contained 127 energy groups which included 8 additional transition region groups and 20 additional fast region groups compared to the initial 99 baseline group structure. To minimize the number of groups, it was decided to not use the additional slowing down region groups or the 40 additional fast groups, despite the additional error reduction. This decision was made to reduce the computation requirements for the 2D and 3D geometry PDT calculations where the angular and spatial resolution study was performed. The neutron flux results for the 127 group structure is shown in Figures 6.17 and 6.18. In Figures 6.17 and 6.18, the difference between MCNP and

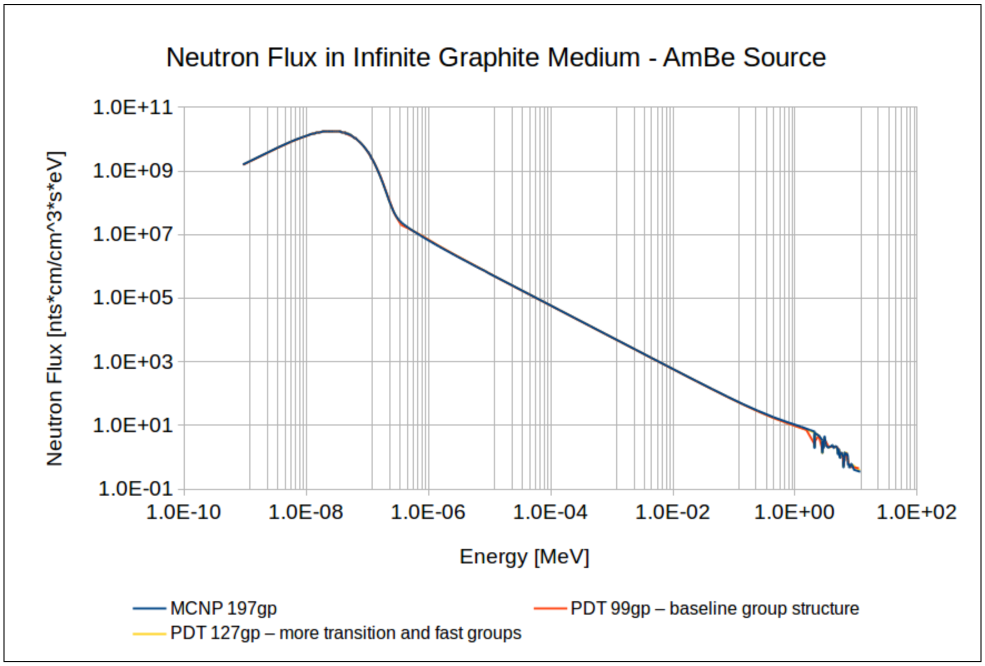

Figure 6.17: Neutron Flux in Infinite Graphite Medium with Uniform AmBe Source. The PDT 127-Group Line is Obscured by the MCNP Line.

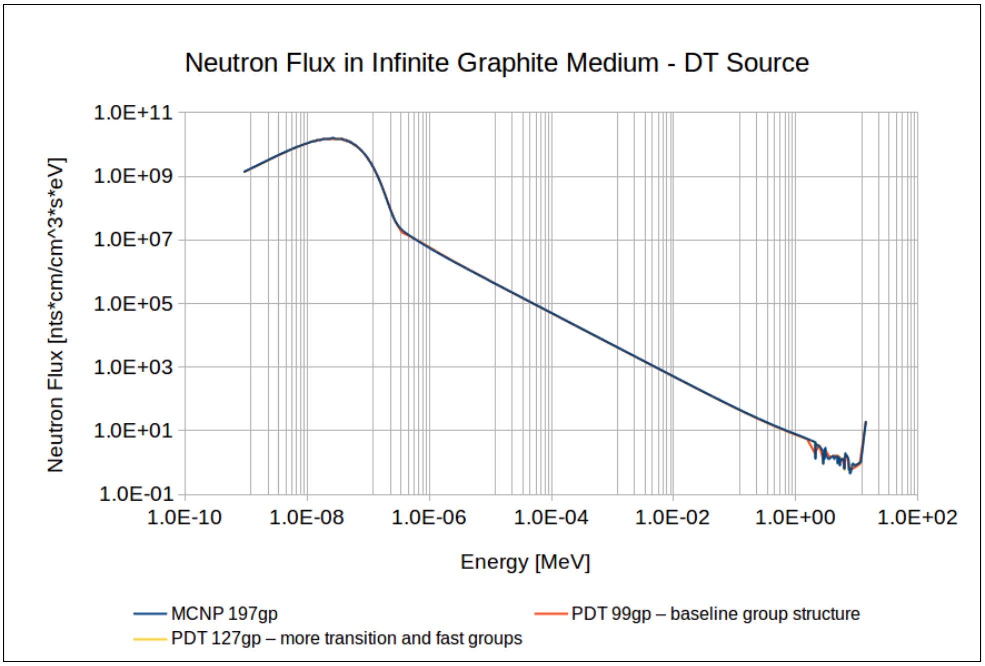

Figure 6.18: Neutron Flux in Infinite Graphite Medium with Uniform DT Source. The PDT 127-Group Line is Obscured by the MCNP Line.

the 99 group PDT results are apparent. On the other hand, the 127 group PDT solution is similar enough to the MCNP solution such that its yellow line is obscured by the MCNP blue line. This group structure produced L2 errors $5.85 \cdot 10^{-3}$ and $3.79 \cdot 10^{-3}$ for the AmBe and DT source solutions respectively.

6.2 2D Geometry Results

The second problem set considered 2D geometry where length in the x and y axes was bounded, but was infinite in the z axis. These problems utilized an approximate infinite AmBe line source parallel to the z-axis centered in the middle of the x and y axes geometry. The approximate line source had dimensions of $1cm \times 1cm$ in the x and y dimensions. $1m \times 1m$ and $10m \times 10m$ geometries were modelled. For the $1m \times 1m$ and $10m \times 10m$ geometries, a spatial and angular analysis was performed to investigate the solution sensitivity to the spatial and angular resolution.

6.2.1 Spatial Analysis

The spatial analysis looked at 4^2, 8^2, 16^2, 32^2, and 64^2 spatial cell refinement. For these calculations, 2048 discrete angles were used for all energy groups. Our study of angular discretization errors, described below, indicated that this number of angles generates an angular discretization error that is small compared to the spatial discretization error we study here. Spatial flux distributions are illustrated for both PDT and MCNP by plotting the cell-averaged flux solution at the cell-center points and then connecting these points to make surface plots. Figure 6.19 shows a quarter slice of the MCNP total flux solution for the $1m \times 1m$ geometry plotted on a 64^2 cell grid. The MCNP neutron flux solution shows an expected peak where the central line source is located. The neutron flux sharply decreases non-linearly away from

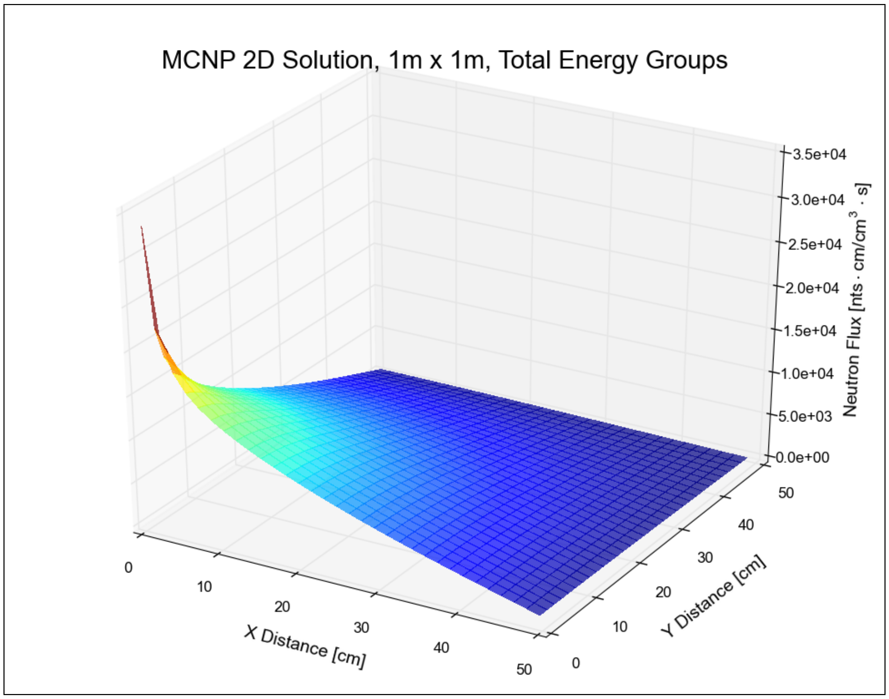

Figure 6.19: 2D MCNP Neutron Flux Solution in $1m \times 1m$.

the source. The slope of the spatial neutron flux distribution becomes less steep the farther it is away from the source. Figures 6.20 through 6.24 depict the PDT solutions for the 4^2, 8^2, 16^2, 32^2, and 64^2 spatial resolutions respectively.

As expected, the difference between PDT and MCNP decreases with additional spatial refinement. The 64^2 cell PDT and MCNP solution is also plotted on a logarithmic z-axis shown in Figures 6.25 and 6.26 respectively. In these figures, it is apparent that using 64^2 cells produced PDT and MCNP solutions that are in very close agreement.

The L2 error was computed assuming that the MCNP solution was the true solution as outlined in Equation 4.1. MCNP was tallied on a matching spatial grid in order to compute the L2 error. The L2 error for the varying spatial refinement for the 2D

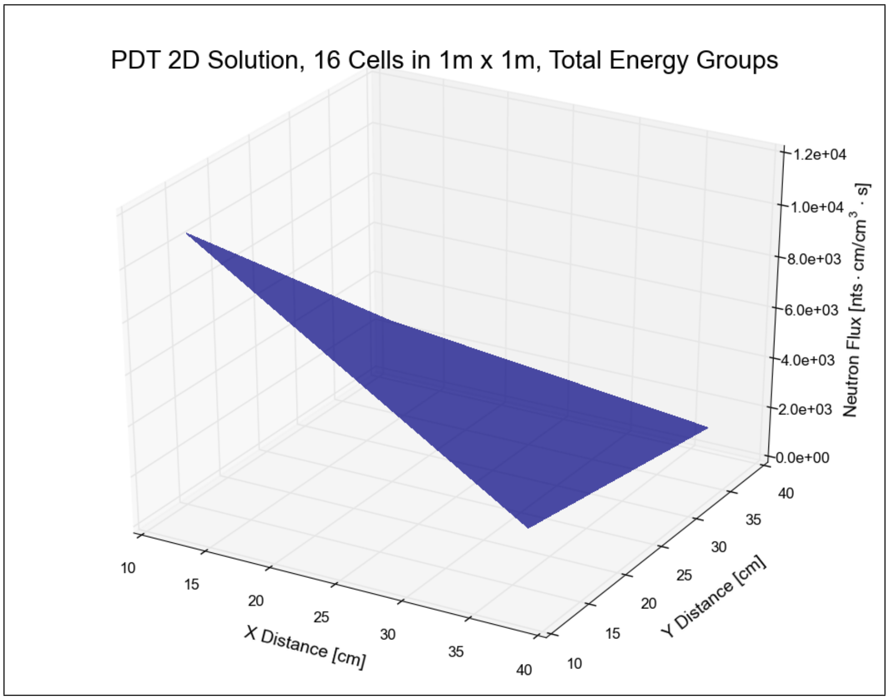

Figure 6.20: 2D PDT Neutron Flux Solution in $1m \times 1m$ using 4^2 Cells.

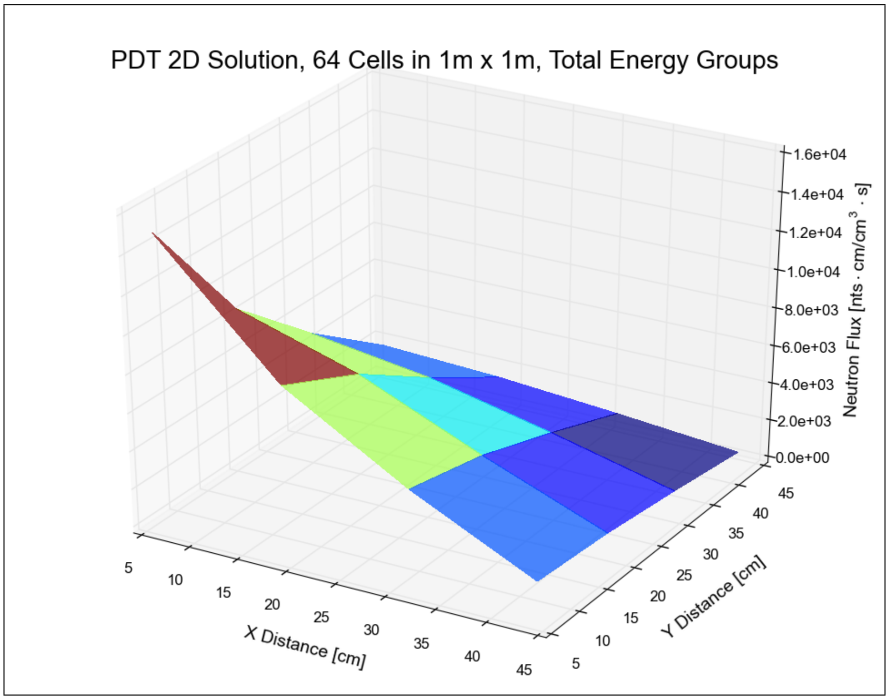

Figure 6.21: 2D PDT Neutron Flux Solution in $1m \times 1m$ using 8^2 Cells.

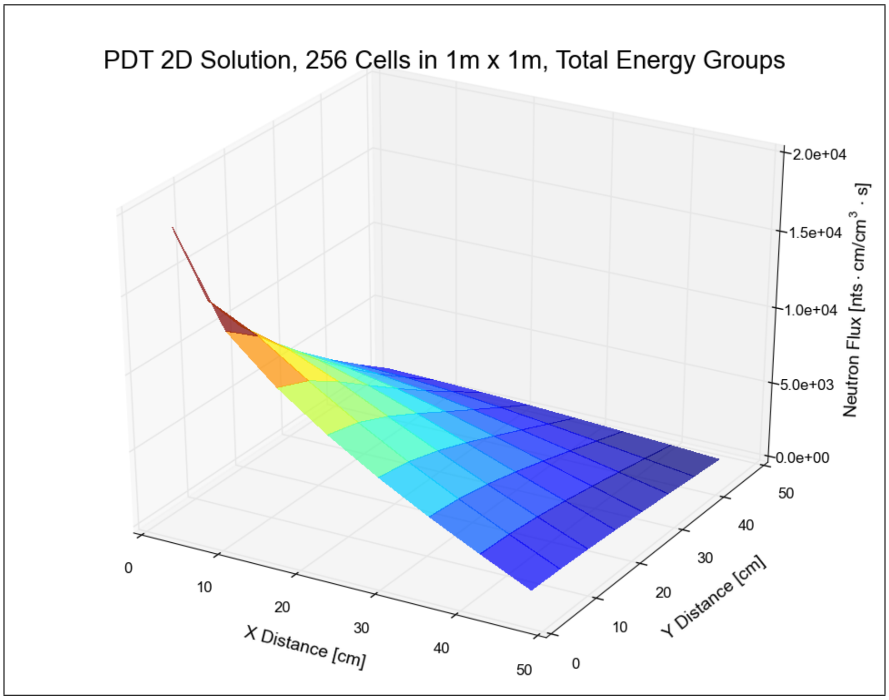

Figure 6.22: 2D PDT Neutron Flux Solution in $1m \times 1m$ using 16^2 Cells.

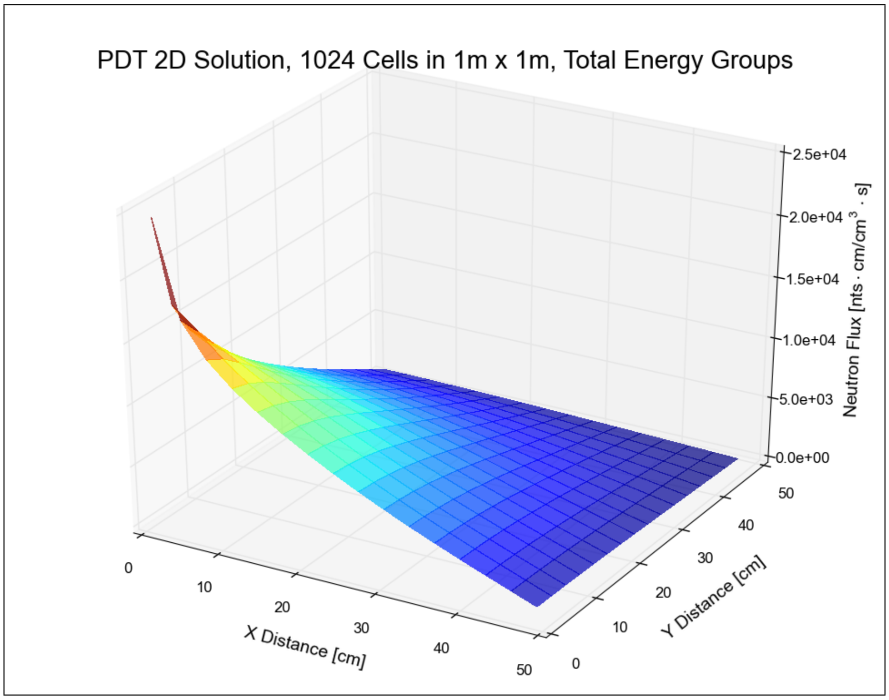

Figure 6.23: 2D PDT Neutron Flux Solution in $1m \times 1m$ using 32^2 Cells.

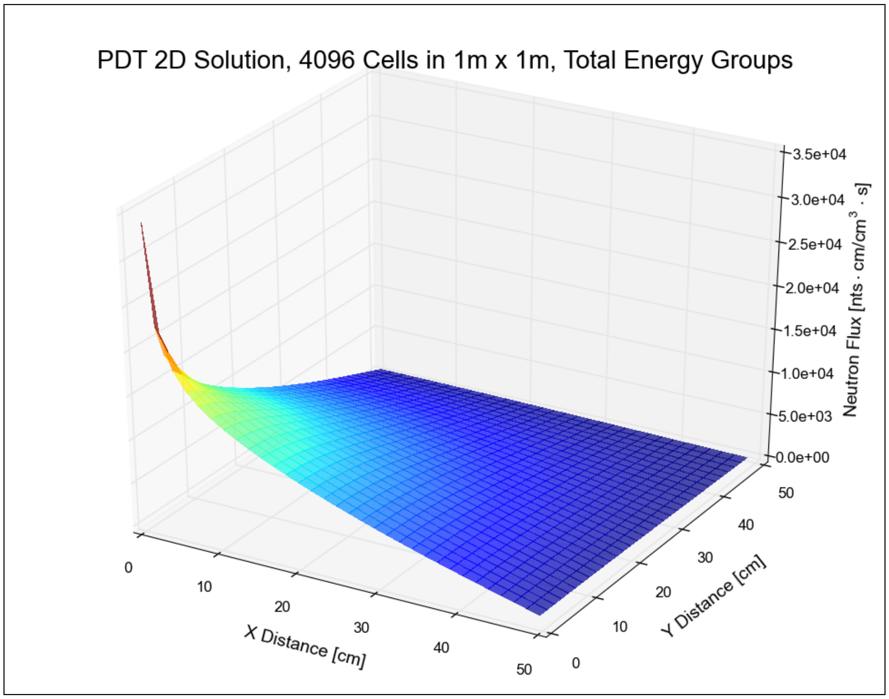

Figure 6.24: 2D PDT Neutron Flux Solution in $1m \times 1m$ using 64^2 Cells.

$1m \times 1m$ geometry is outlined in Table 6.1. In Table 6.1, the "Convergence Rate"

Table 6.1: L2 Error Spatial Analysis in $1m \times 1m$.

Problem	Cells	Cell Width [m]	L2 error	Convergence Rate	Error Ratio
4x4	16	0.2500	0.5265		
8x8	64	0.1250	0.3536	0.5745	1.4891
16x16	256	0.0625	0.2455	0.5265	1.4405
32x32	1024	0.0313	0.1589	0.6272	1.5445
64x64	4096	0.0156	0.0529	1.5871	3.0043

and "Error Ratio" are computed as shown in Equations 6.1 and 6.2.

$$Convergence\,Rate = \frac{\log(\epsilon_{i-1}) - \log(\epsilon_i)}{\log(2)} \tag{6.1}$$

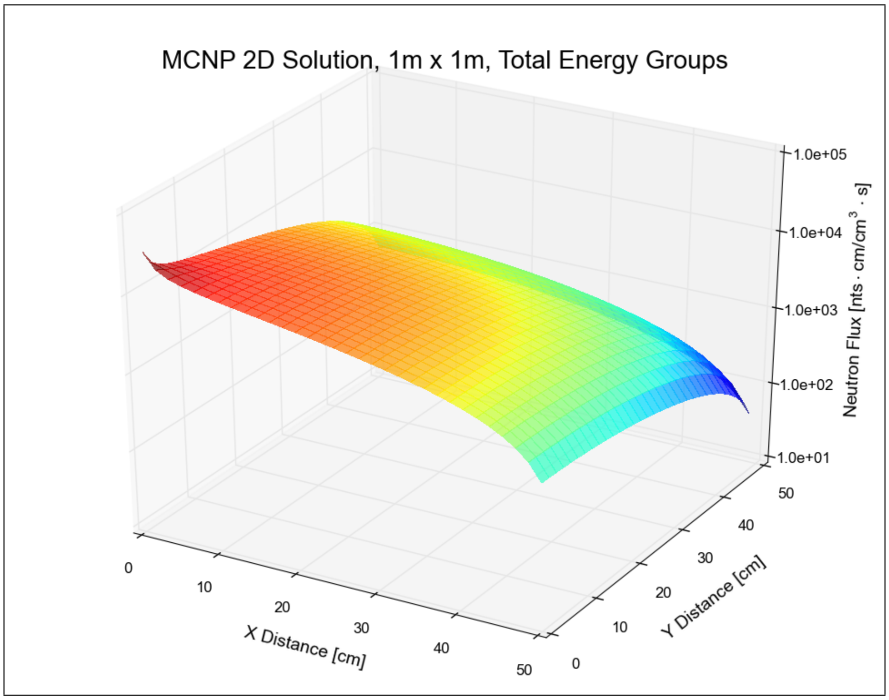

Figure 6.25: 2D MCNP Neutron Flux Solution in $1m \times 1m$.

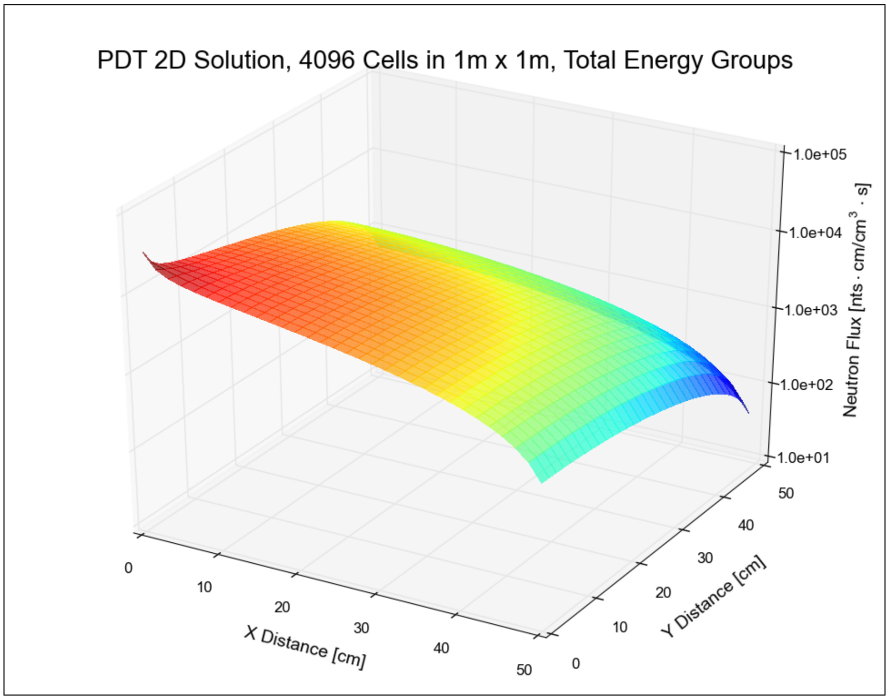

Figure 6.26: 2D PDT Neutron Flux Solution in $1m \times 1m$ using 64^2 Cells.

$$Error\ Ratio = \frac{\epsilon_{i-1}}{\epsilon_i} \tag{6.2}$$

where ϵ_i refers to the current spatial refinement error and ϵ_{i-1} refers to the previous spatial refinement error. It is seen that the L2 error decreases with increasing spatial refinement. From Table 6.1, it is seen the convergence rate is initially low, with not even a first-order convergence, due to its extreme coarse spatial mesh. However, the convergence rate is seen to increase as the spatial mesh is further refined. Going from the 32x32 to 64x64 spatial refinement saw a convergence of 1.59. For smooth solutions, theory predicts that the PWLD spatial discretization will produce second-order errors (convergence rate = 2 and error ratio = 4) in the fine-mesh limit. In our test problem the solution is dominated by smooth components, so we would expect to see second-order behaviour if we continued to refine the mesh. Limited computational resources for this study prevented further refinement at this time. The L2 error is plotted in Figure 6.27 along with a dashed line showing a second-order slope.

The MCNP solution for the $10m \times 10m$ geometry plotted on a 64^2 cell grid is depicted in Figure 6.28. As was seen in the previous $1m \times 1m$ solutions, the flux is seen to peak where the source is located and decrease non-linearly away from the source. The PDT solutions for the $10m \times 10m$ geometry are given in Figures 6.29 through 6.33.

Once again the PDT solution is seen to approach the MCNP solution with additional spatial refinement. The 64^2 cell PDT and MCNP solutions, plotted on a logarithmic z-axis in Figures 6.34 and 6.35, show close agreement between MCNP and PDT.

PDT and MCNP results on matching spatial grids were used to compute the L2

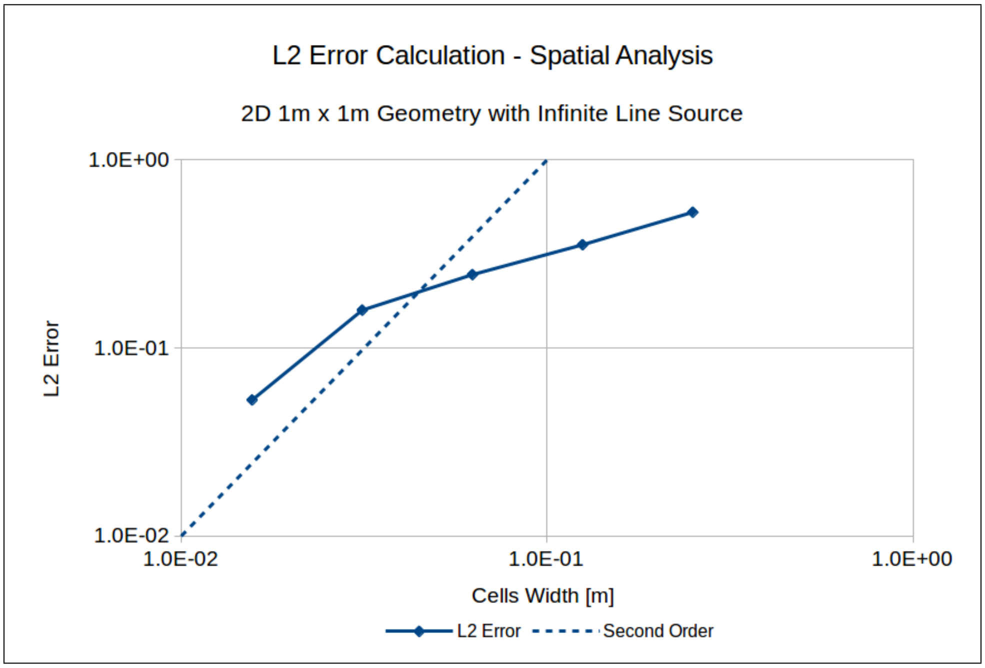

Figure 6.27: L2 Norm Error Spatial Analysis in $1m \times 1m$ on Log-Log Axes.

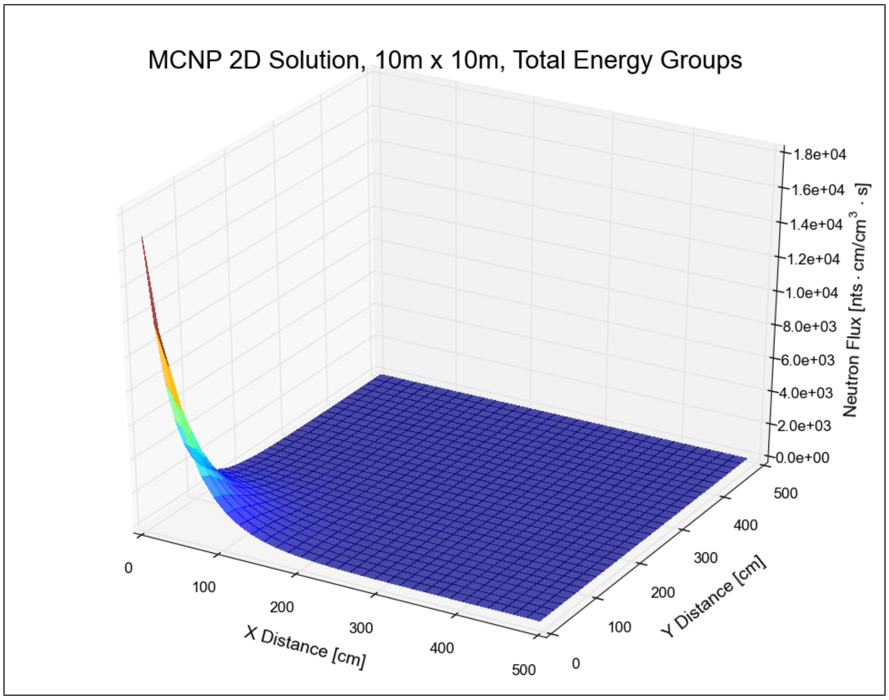

Figure 6.28: 2D MCNP Neutron Flux Solution in $10m \times 10m$.

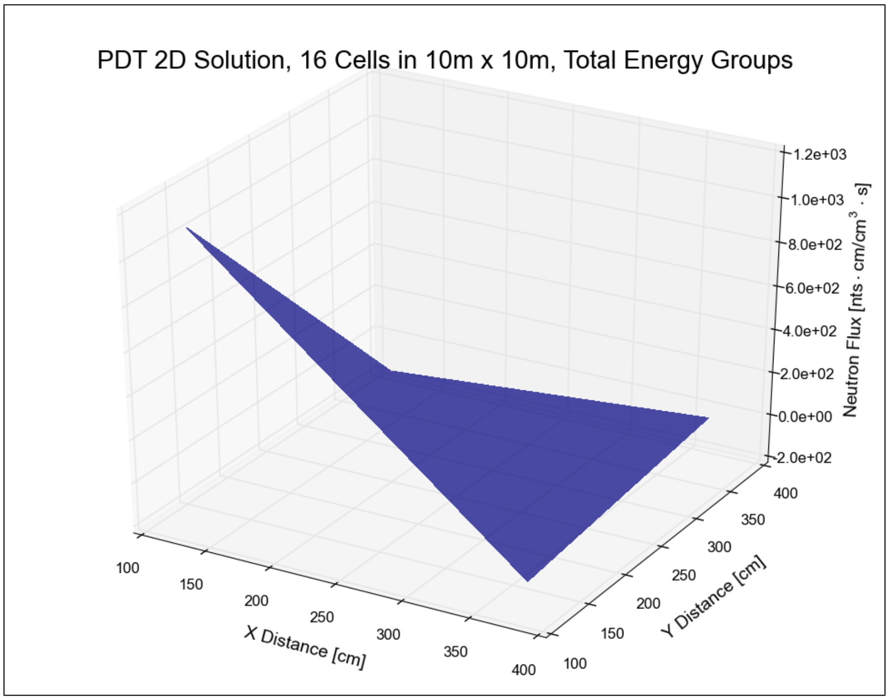

Figure 6.29: 2D PDT Neutron Flux Solution in $10m \times 10m$ using 4^2 Cells.

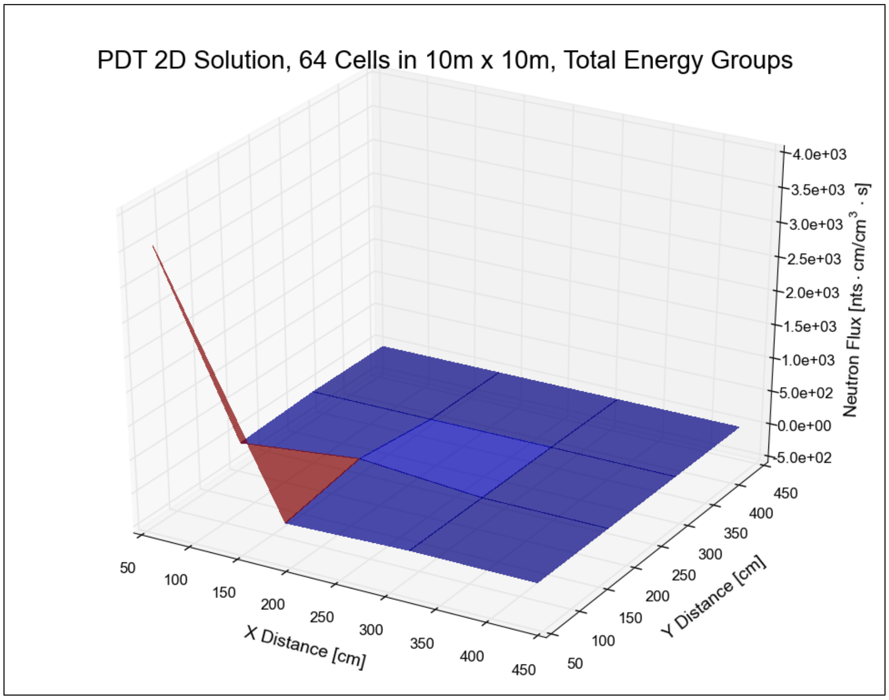

Figure 6.30: 2D PDT Neutron Flux Solution in $10m \times 10m$ using 8^2 Cells.

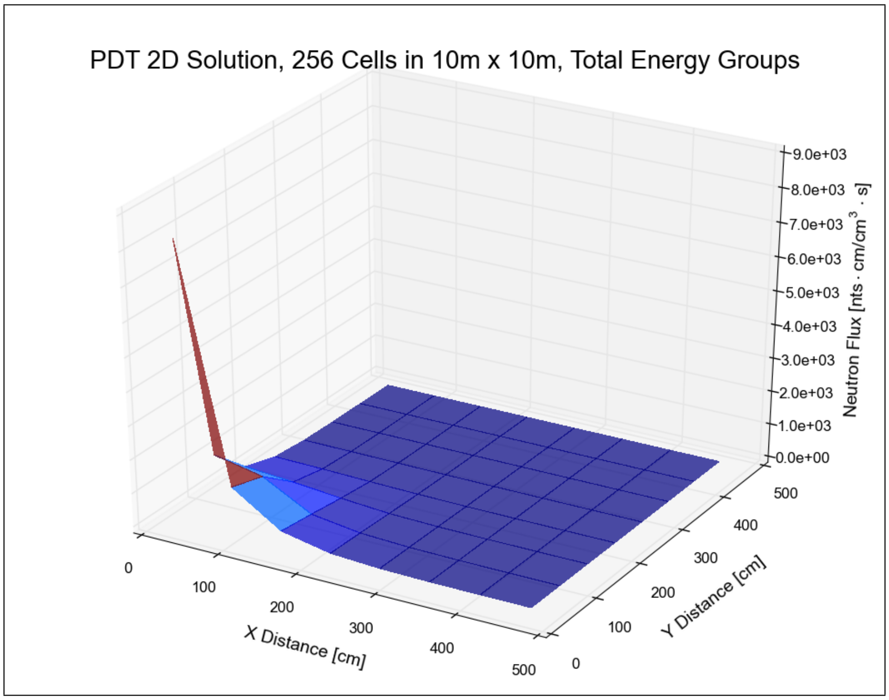

Figure 6.31: 2D PDT Neutron Flux Solution in $10m \times 10m$ using 16^2 Cells.

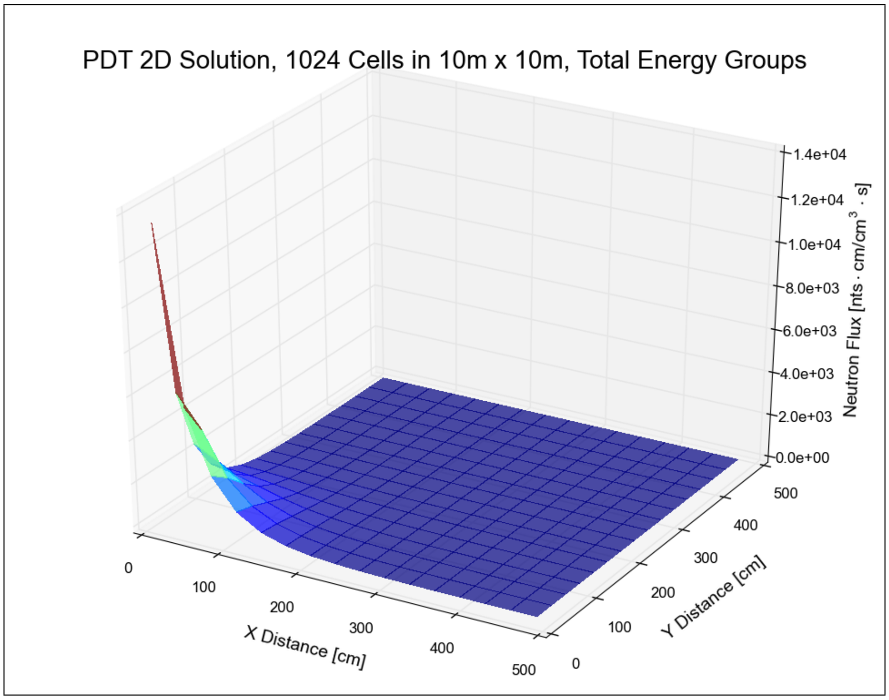

Figure 6.32: 2D PDT Neutron Flux Solution in $10m \times 10m$ using 32^2 Cells.

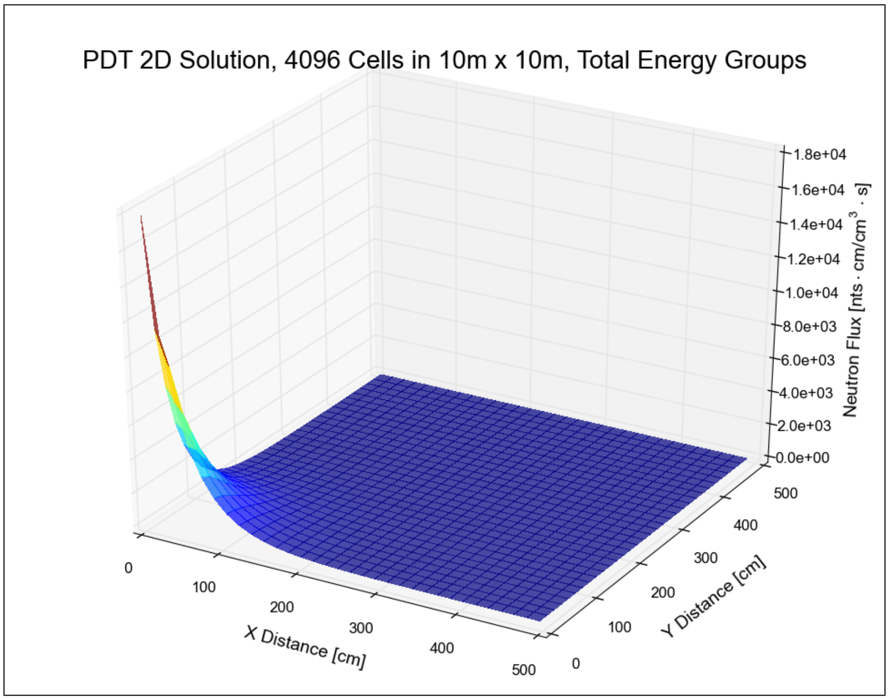

Figure 6.33: 2D PDT Neutron Flux Solution in $10m \times 10m$ using 64^2 Cells.

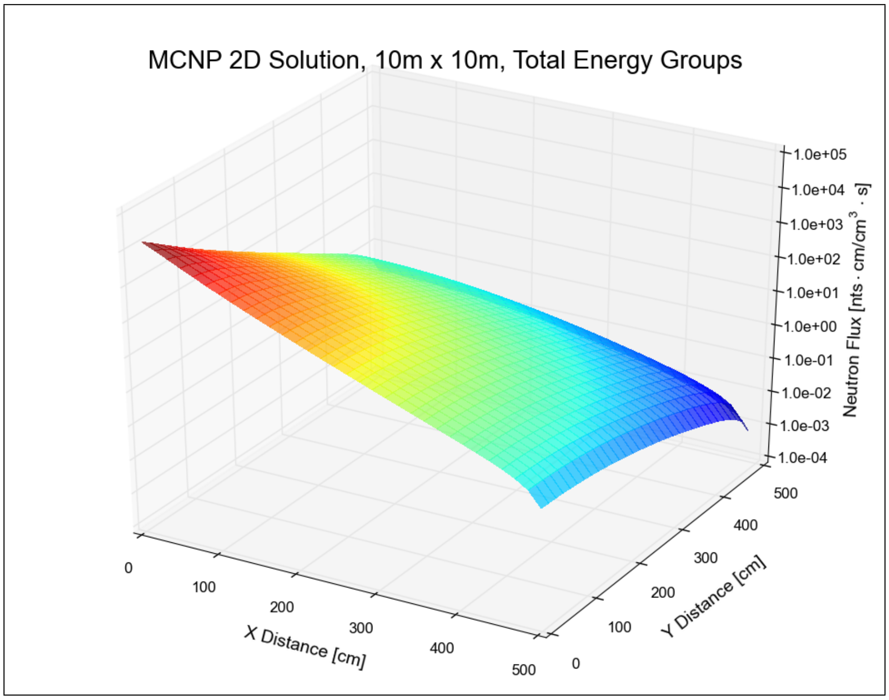

Figure 6.34: 2D MCNP Neutron Flux Solution in $10m \times 10m$.

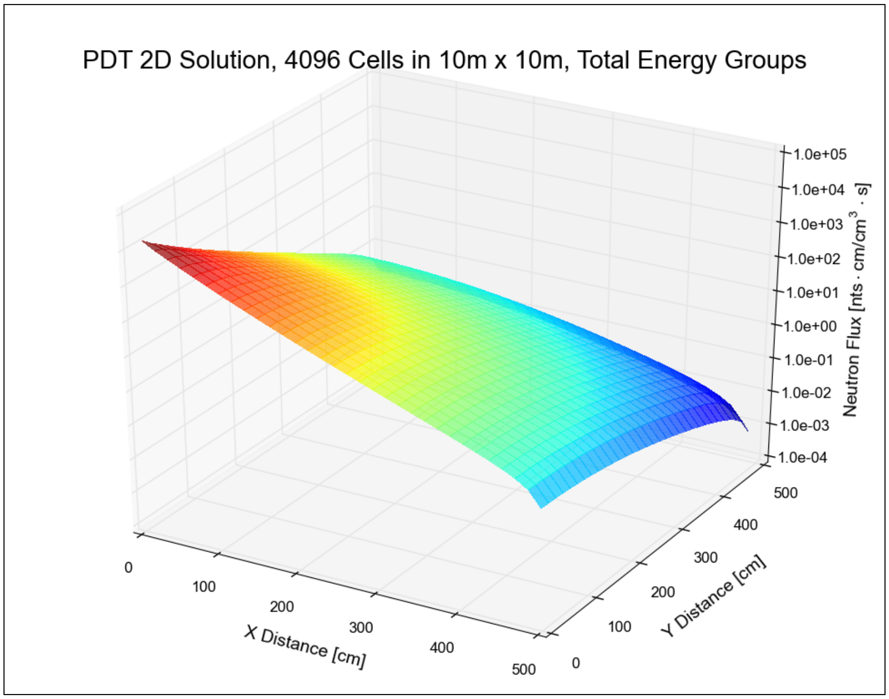

Figure 6.35: 2D PDT Neutron Flux Solution in $10m \times 10m$ using 64^2 Cells.

error using Equation 4.1. The $10m \times 10m$ 2D geometry L2 error as function of spatial refinement is given in Table 6.2. As expected the L2 error decreases for

Table 6.2: L2 Error Spatial Analysis in $10m \times 10m$.

Problem	Cells	Cell Width [m]	L2 error	Convergence Rate	Error Ratio
4x4	16	2.5000	0.9076		
8x8	64	1.2500	0.7024	0.3699	1.2923
16x16	256	0.6250	0.4429	0.6653	1.5859
32x32	1024	0.3125	0.2428	0.8671	1.8240
64x64	4096	0.1563	0.0579	2.0673	4.1910

increasing spatial refinement. Just as was seen in the $1m \times 1m$ geometry spatial analysis, the convergence rate for the $10m \times 10m$ geometry starts very low for an extremely coarse mesh. As the spatial distribution was refined, the convergence rate approached approximately 2nd order, which is the theoretical expected fine-mesh convergence rate for the smooth portion of the analytic solution. The error is seen to decrease by a factor of 4 when going from 32x32 to 64x64 spatial refinement. The L2 errors are plotted in Figure 6.36.

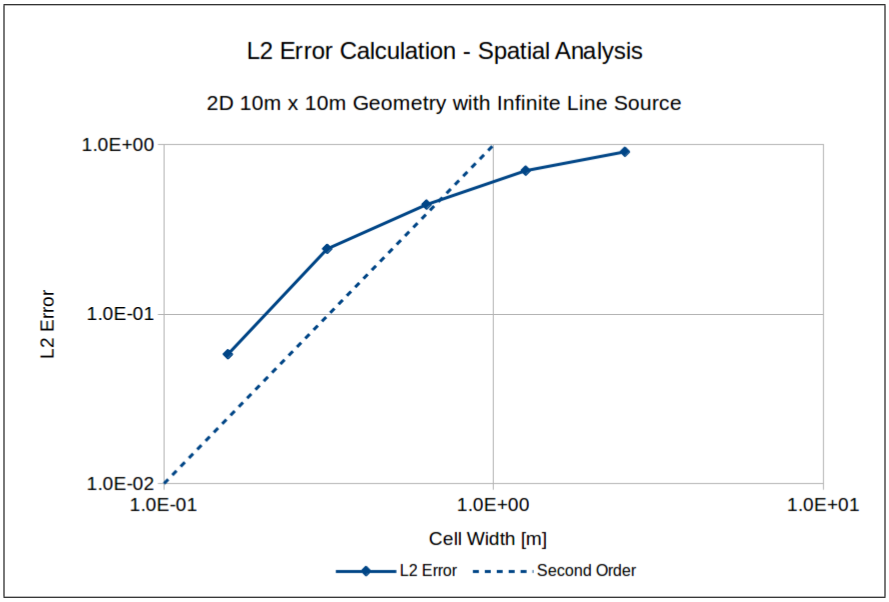

Figure 6.36: L2 Norm Error Spatial Analysis in $10m \times 10m$ on Log-Log Axes.

6.2.2 *Angular Analysis*

As was discussed in the Computation Methods section, S_N methods suffer an undesirable phenomena known as ray effects. Ray effects are spatial oscillations in the neutron flux solution that occur when the angular variables are under resolved [10]. The ray effects are more dominant at higher neutron energies and thus more quadrature directions will be needed in order to reduce the discretization error within an acceptable margin. This section outlines the angular analysis for the 2D geometry which investigates the angular discretization error at various energy levels.

As was discussed in the Methods section, the angular analysis was performed by varying number of polar angles per hemisphere and azimuthal angles per quadrant independently in 7 energy ranges with the following energy divisions: $1 \times 10^{-11} MeV$, $1.78 \times 10^{-5} MeV$, $1 \times 10^{-3} MeV$, $0.1 MeV$, $1.0 MeV$, $4.94 MeV$, $9.0 MeV$, and $14.1 MeV$. 128, 512, 2048, 8192, and 32768 angle quadrature sets were considered. These angular quadrature sets are outlined in Table 4.2. The 2048 angle quadrature set was utilized in energy groups where the angle set was being held constant. 32^2 spatial cells and 127 energy groups were utilized in the 2D angular analysis.

Figure 6.37 shows the MCNP neutron flux solution in the highest energy range, $9.0 MeV$ to $14.1 MeV$. The PDT solution using the 128 angle set is shown in Figure 6.38. Spatial oscillations from ray effects are clearly seen in the PDT flux using 128 angles. Thus it can be concluded that a higher quadrature set is needed. The PDT solution using the 512 angle quadrature set is displayed in Figure 6.39. With 512 angles, the majority of the spatial osculations that were previously seen have been resolved. However, there are still some slight oscillations apparent, for example along $y = 0$. The PDT solution using the 2048 angle quadrature set, shown in Figure 6.40, does not have any more perceivable spatial oscillations and close agreement is seen between the MCNP and PDT solutions.

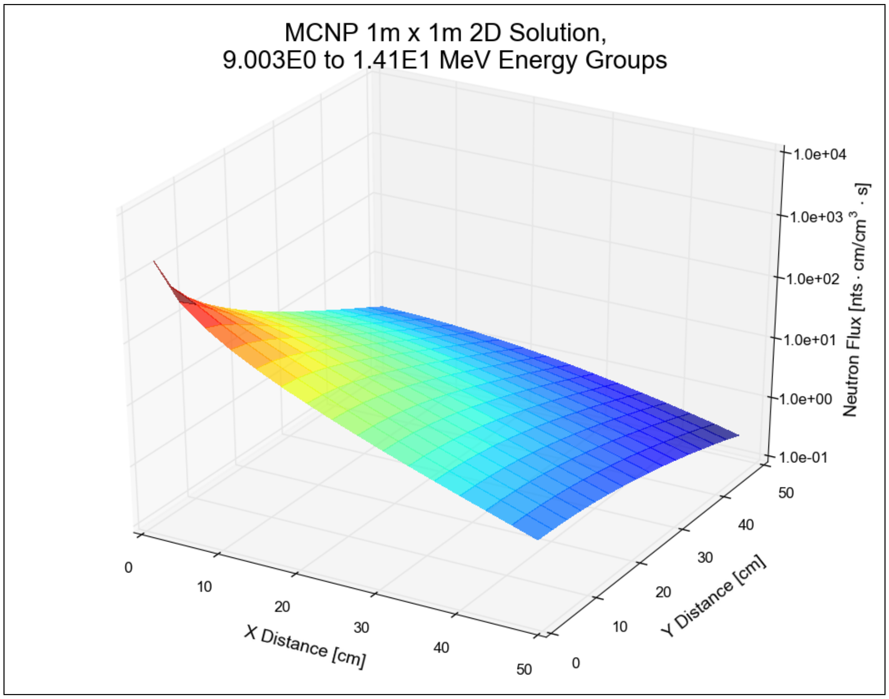

Figure 6.37: MCNP $1m \times 1m$ 2D Neutron Flux Solution in $9.0MeV$ to $14.1MeV$ Energy Groups.

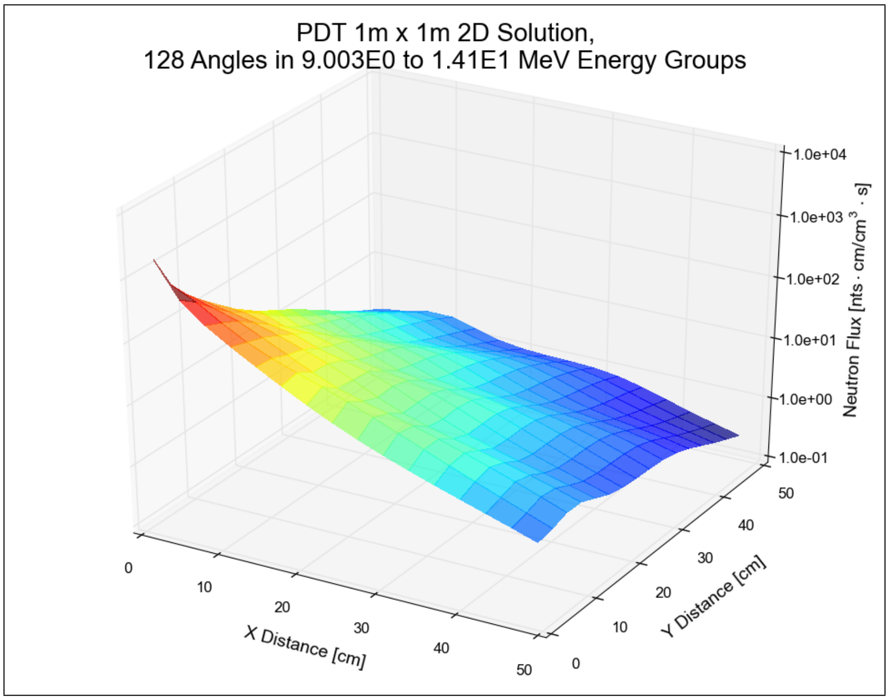

Figure 6.38: PDT $1m \times 1m$ 2D Neutron Flux Solution in $9.0MeV$ to $14.1MeV$ Energy Groups using 128 Angles.

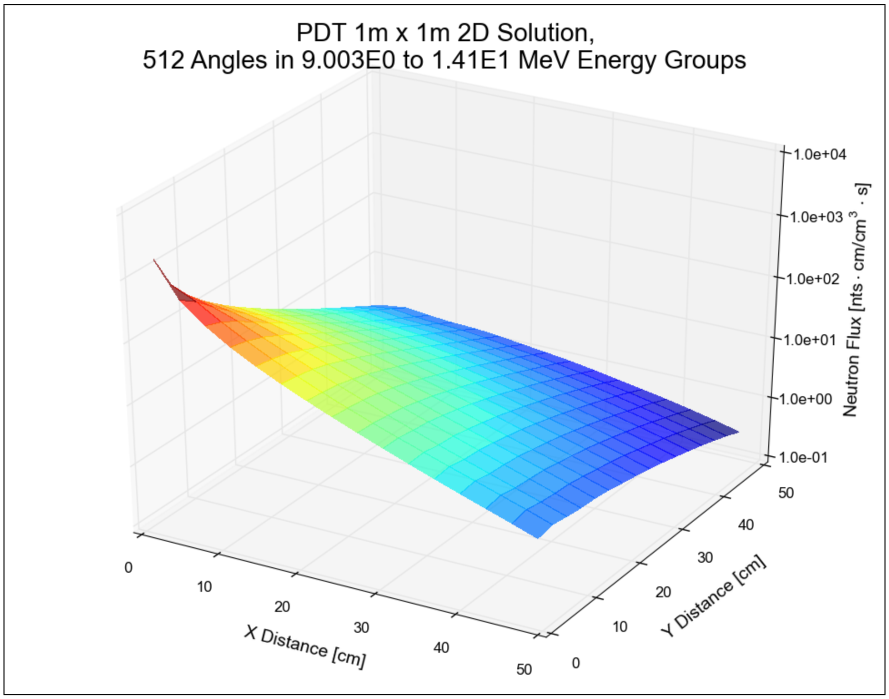

Figure 6.39: PDT $1m \times 1m$ 2D Neutron Flux Solution in $9.0MeV$ to $14.1MeV$ Energy Groups using 512 Angles.

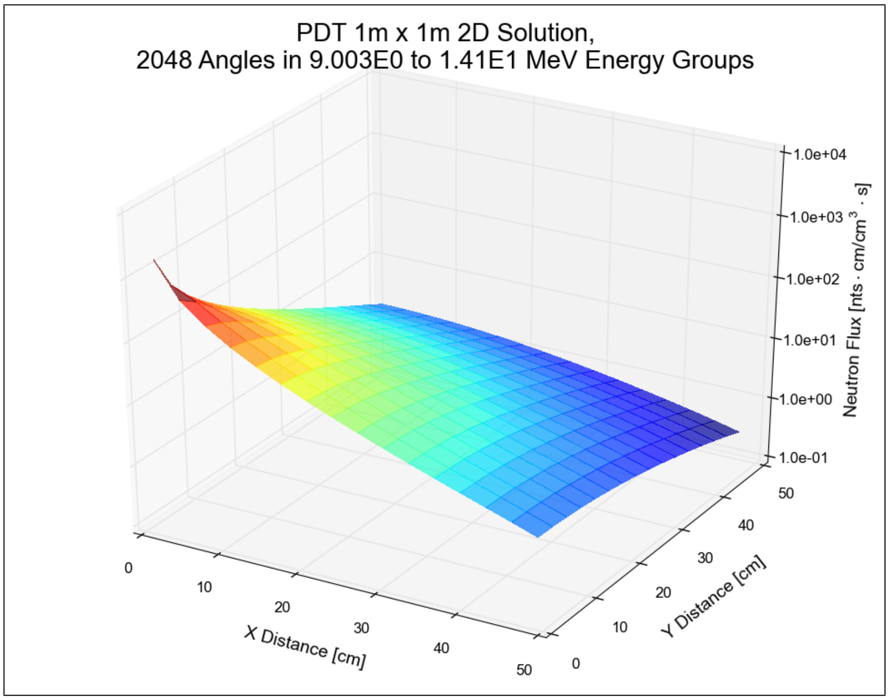

Figure 6.40: PDT $1m \times 1m$ 2D Neutron Flux Solution in $9.0MeV$ to $14.1MeV$ Energy Groups using 2048 Angles.

The MCNP solution for the 4.9MeV to 9.0MeV energy range is given in Figure 6.41. The PDT solution using 128 angles, shown in Figure 6.42, has distinct spatial oscillations from ray effects. Once again using a higher quadrature set of 512 angles resolved the majority of the ray effects, which is seen in Figure 6.43. The last of the noticeable ray effects of the PDT solution are resolved using the 2048 angle quadrature set, as seen in Figure 6.44, and thus achieving close agreement with MCNP.

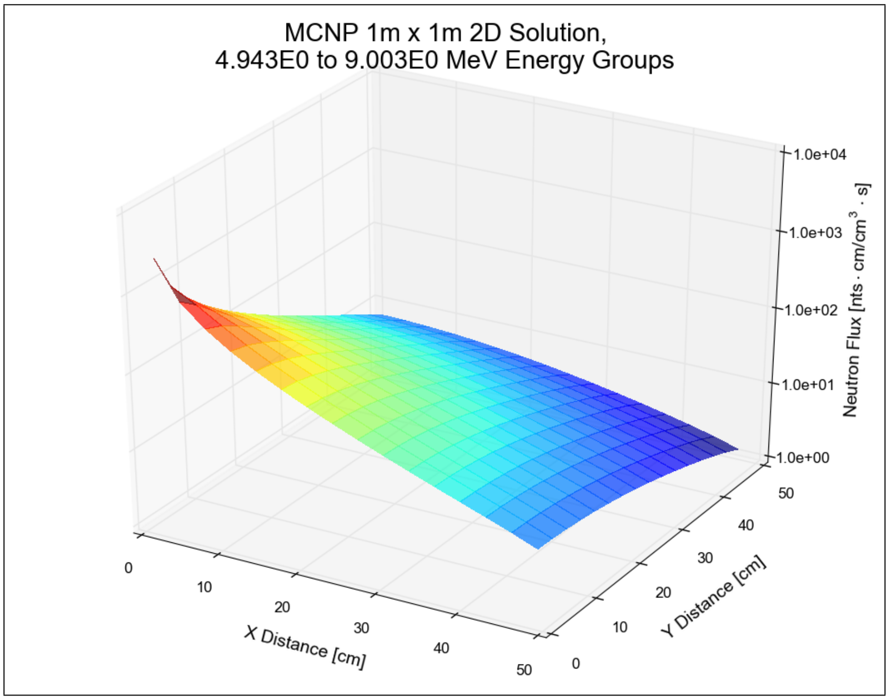

Figure 6.41: MCNP $1m \times 1m$ 2D Neutron Flux Solution in 4.9MeV to 9.0MeV Energy Groups.

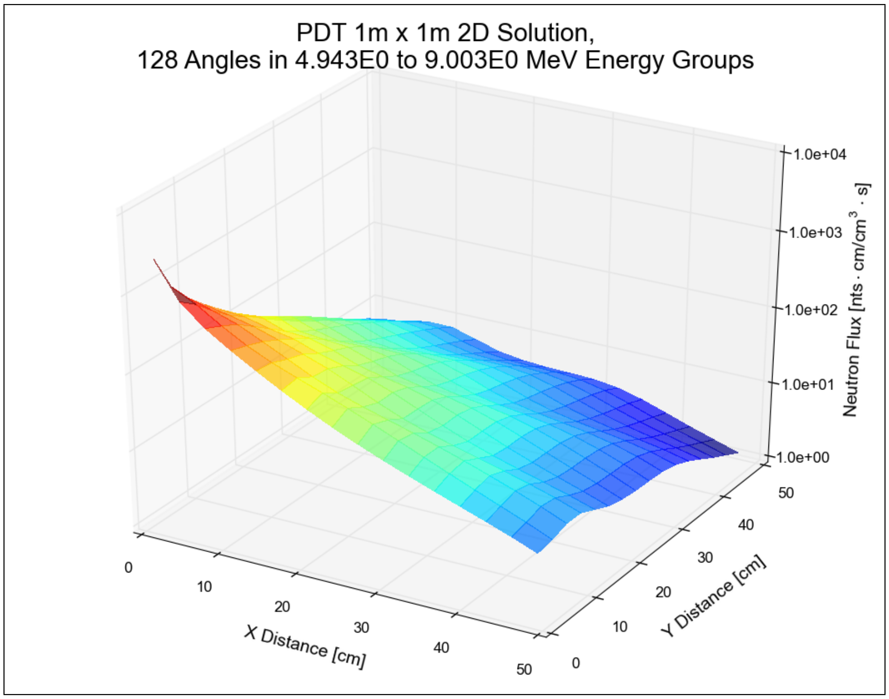

Figure 6.42: PDT $1m \times 1m$ 2D Neutron Flux Solution in $4.9MeV$ to $9.0MeV$ Energy Groups using 128 Angles.

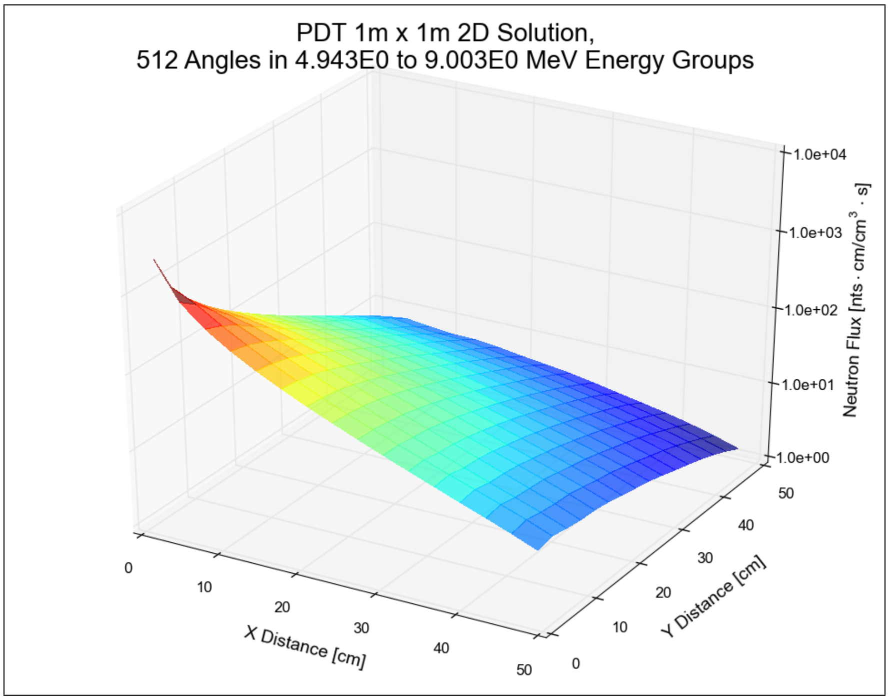

Figure 6.43: PDT $1m \times 1m$ 2D Neutron Flux Solution in $4.9MeV$ to $9.0MeV$ Energy Groups using 512 Angles.

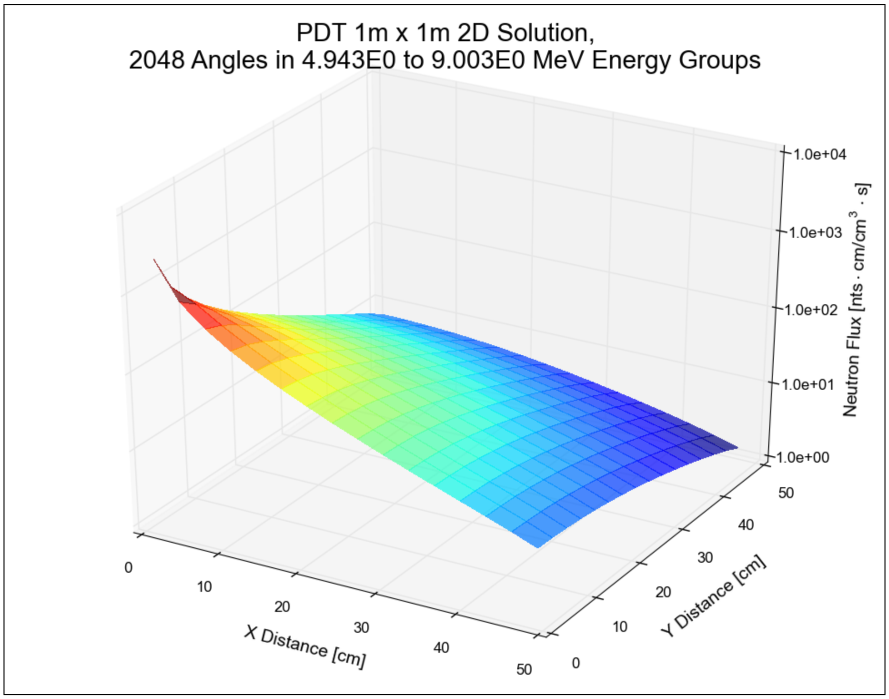

Figure 6.44: PDT $1m \times 1m$ 2D Neutron Flux Solution in $4.9MeV$ to $9.0MeV$ Energy Groups using 2048 Angles.

The MCNP results for the energy group set, $1.0MeV$ to $4.9MeV$, is shown in Figure 6.45. The PDT flux using 128 angles, plotted in Figure 6.46, does not show perceivable ray effects in the spatial neutron flux solution, unlike the higher energy groups.

The flux is also seen to become less peak compared to the higher energy neutron flux solutions. Energy loss in an elastic scattering event is dependent on the initial energy of the neutron. The higher the initial neutron energy is, the more energy a neutron loses on average in an elastic scatter event. At higher neutron energies, there will be fewer neutrons that have scattered down from even higher energies. On the other hand, at lower neutron energies there will be more accumulation of neutrons away from the source that have scattered down from higher energies. This effectively works to flatten the flux distribution at lower energies. In addition, at thermal energies upscattering occurs, which would work to flatten the flux distribution further. Thus it is expected that the higher the neutron energy is, the quicker the neutron group flux will drop off heading away from the source.

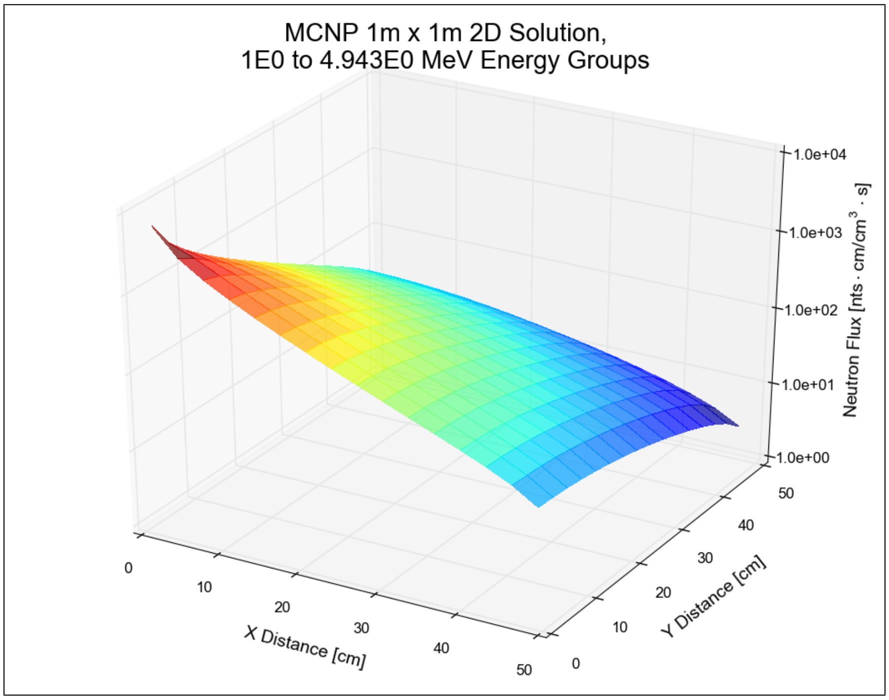

Figure 6.45: MCNP $1m \times 1m$ 2D Neutron Flux Solution in $1.0MeV$ to $4.9MeV$ Energy Groups.

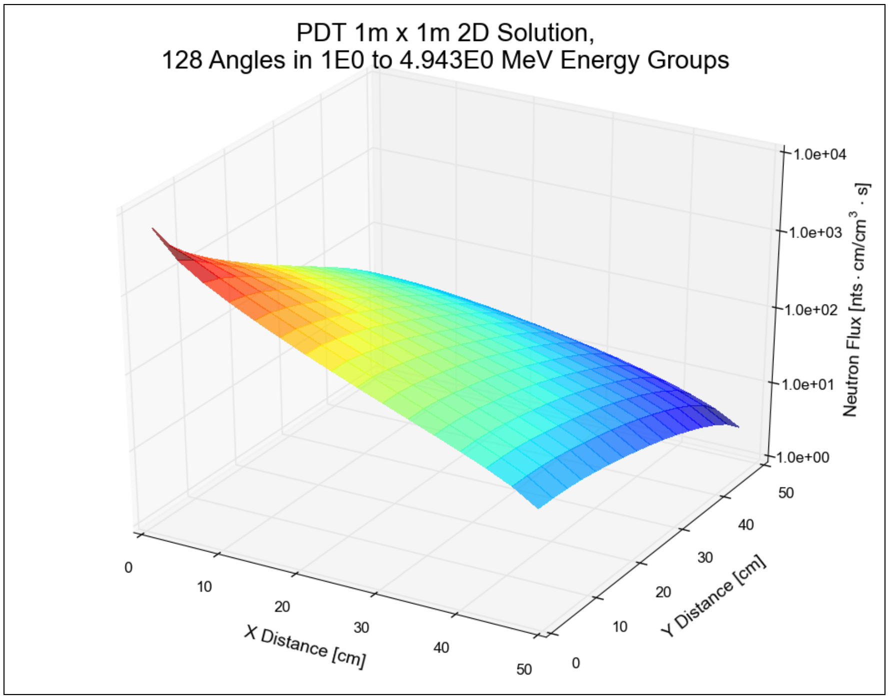

Figure 6.46: PDT $1m \times 1m$ 2D Neutron Flux Solution in $1.0 MeV$ to $4.9 MeV$ Energy Groups using 128 Angles.

Since ray effects are less dominant as neutron energy decreases, there are also no noticeable spatial oscillations from ray effects using 128 angles in energy groups lower than 1.0 MeV. Thus, the spatial flux plots for the next several energy groups are not shown, except for the lowest (thermal) energy group. Figure 6.47 outlines the MCNP neutron flux solution in the $1 \times 10^{-11} MeV$ to $1.78 \times 10^{-5} MeV$ energy range. The PDT solutions using 128 angles is shown in Figure 6.48. As expected, no spatial oscillations are present in the PDT solution using 128 angles. Once again, the neutron flux is seen to be much flatter compared to the neutron flux at higher energies.

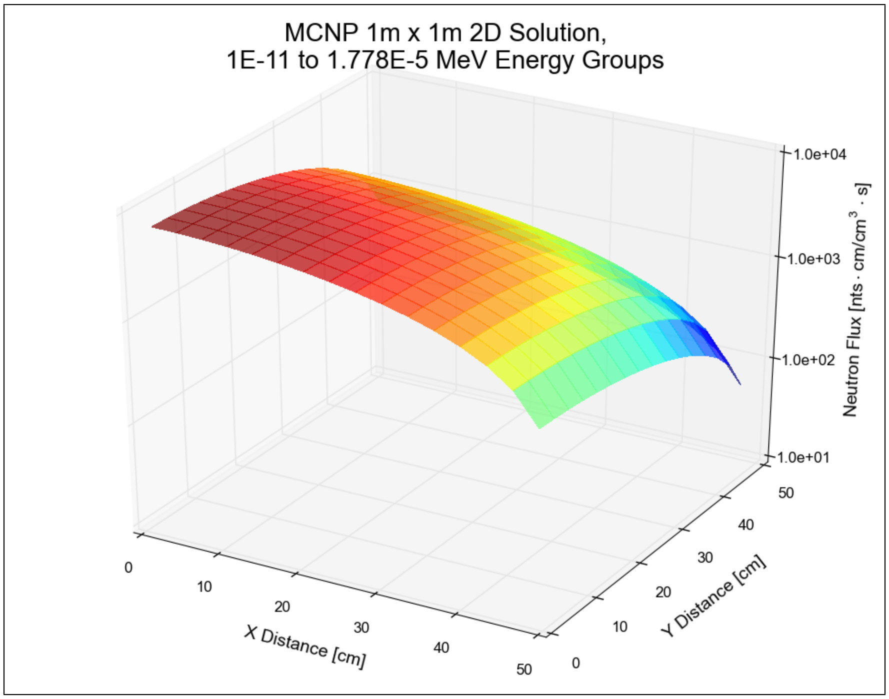

Figure 6.47: MCNP $1m \times 1m$ 2D Neutron Flux Solution in $1 \times 10^{-11} MeV$ to 1.78×10^{-5} Energy Groups.

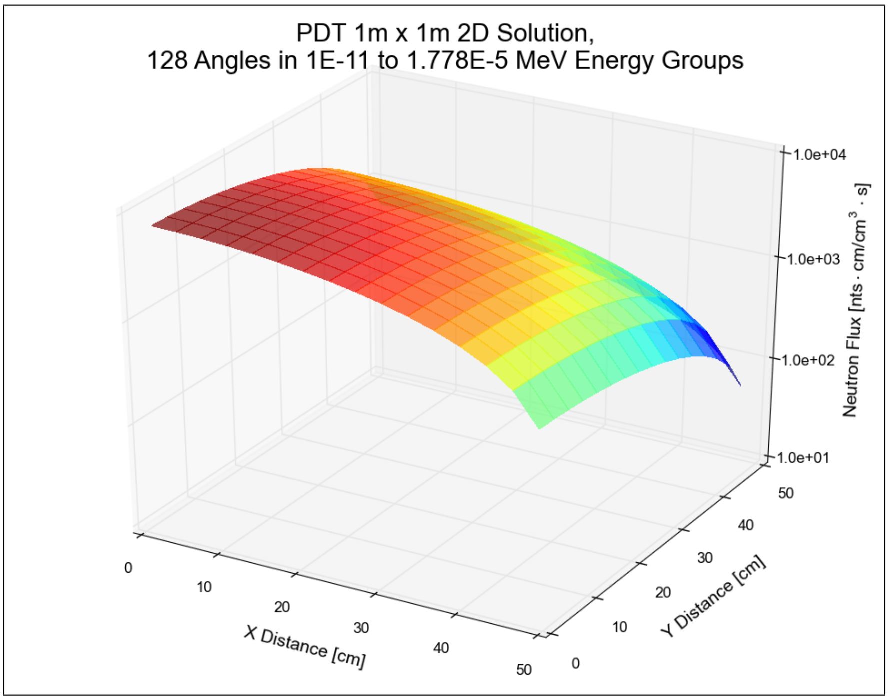

Figure 6.48: PDT $1m \times 1m$ 2D Neutron Flux Solution in $1 \times 10^{-11} MeV$ to 1.78×10^{-5} Energy Groups using 128 Angles.

Additional insight on the angular analysis results and the ray effects can be gained by looking at the neutron flux along one of the outer edges of the $1m \times 1m$ graphite. Figure 6.49, 6.50, and 6.51 depicts the neutron flux in fast energy groups $4.9MeV$ to $9.0MeV$ using 128, 512, and 2048 angles respectively. Using 128 angles, the ray effects are clearly seen. As expected, most of these ray effects were resolved in the 512 angle quadrature set. Last, close agreement in seen between MCNP and PDT in the 2048 angle set.

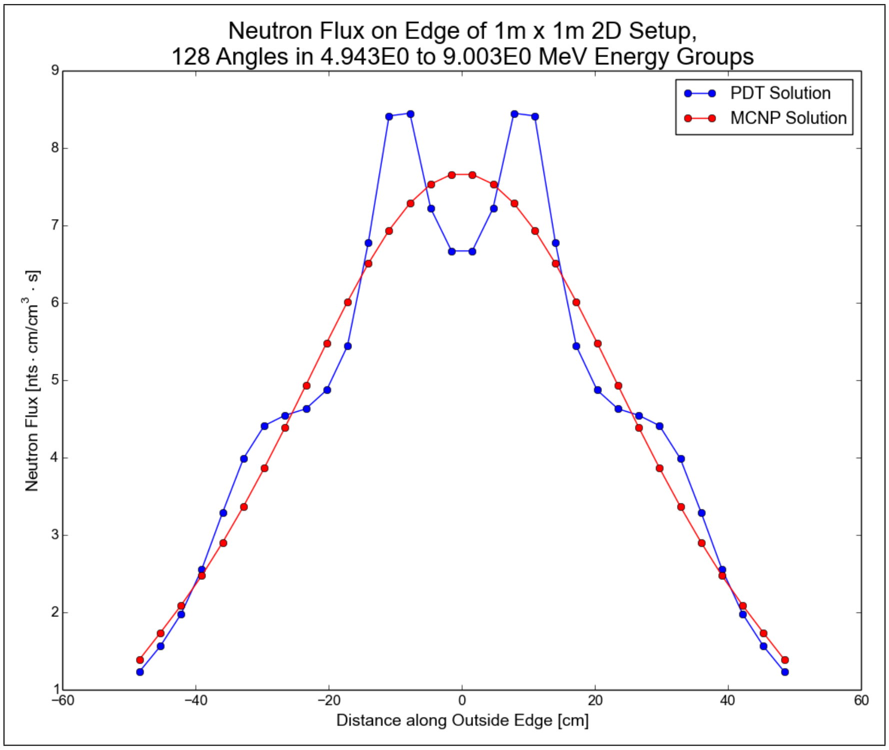

Figure 6.49: Neutron Flux on Edge of $1m \times 1m$ 2D Setup in $4.9MeV$ to $9.0MeV$ Energy Groups using 128 Angles.

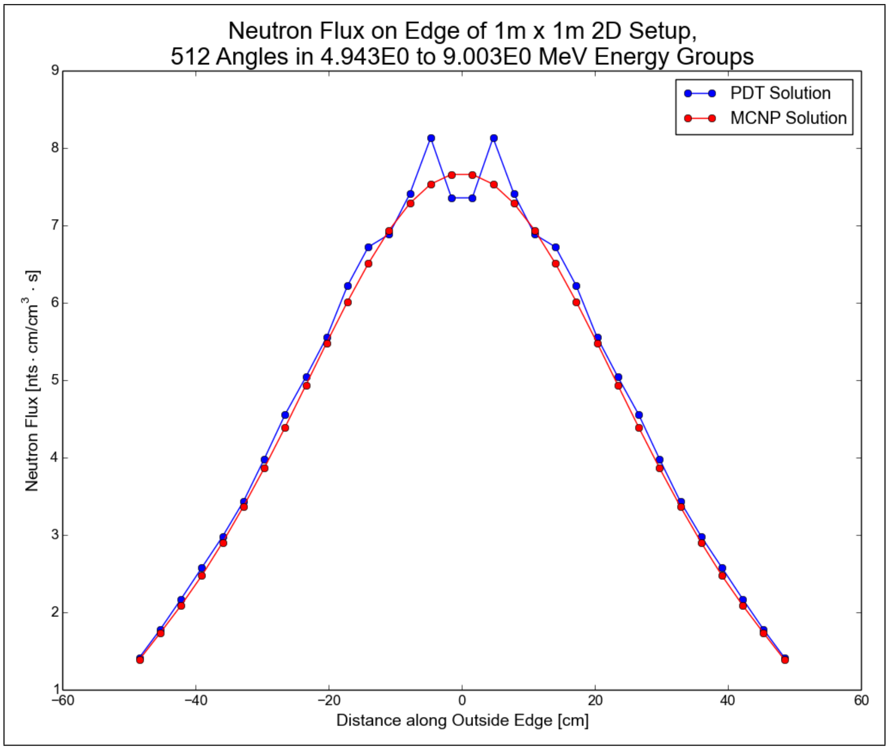

Figure 6.50: Neutron Flux on Edge of $1m \times 1m$ 2D Setup in $4.9MeV$ to $9.0MeV$ Energy Groups using 512 Angles.

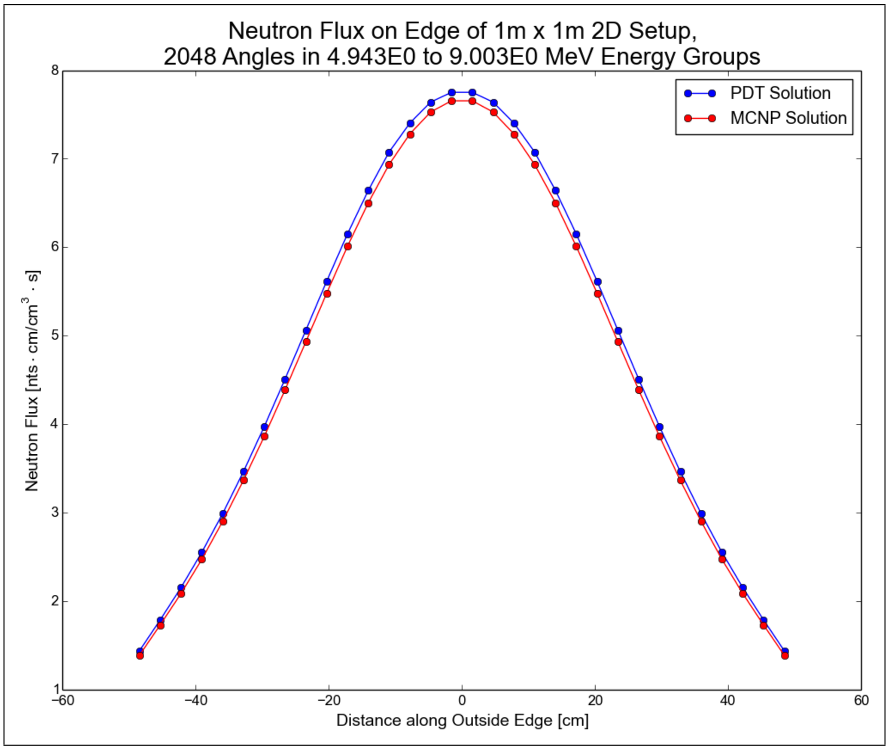

Figure 6.51: Neutron Flux on Edge of $1m \times 1m$ 2D Setup in $4.9MeV$ to $9.0MeV$ Energy Groups using 1024 Angles.

In comparison, the neutron flux for thermal groups $1\times10^{-11}MeV$ to $1.78\times10^{-5}MeV$ along side the outer edge of the $1m\times1m$ geometry is shown Figure 6.52. In contrast to what was seen with the fast energy groups, using the 128 angle quadrature set produced very similar MCNP and PDT results with no perceivable ray effects.

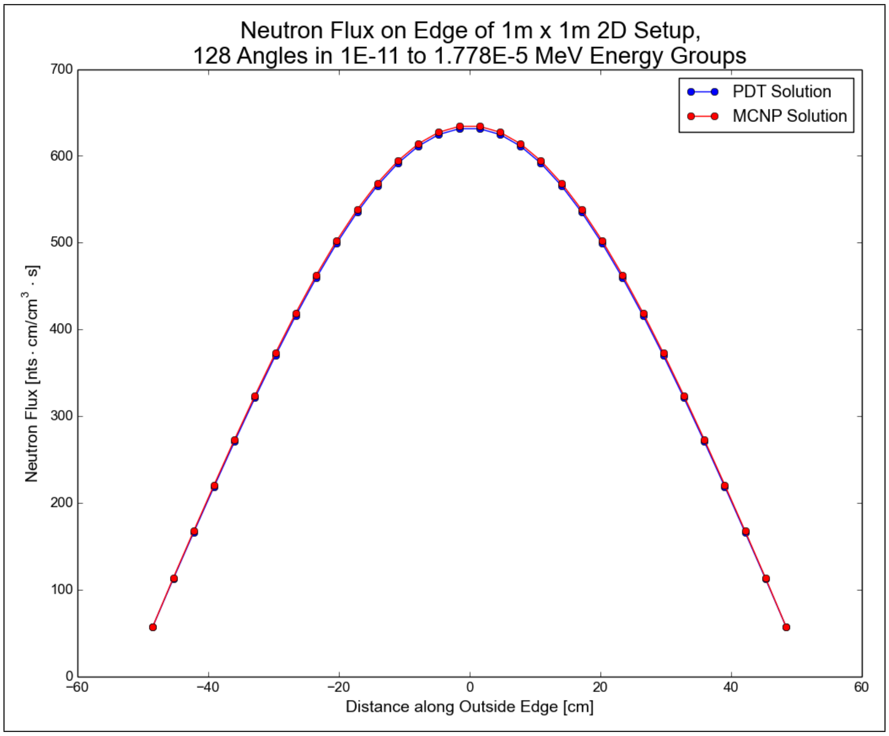

Figure 6.52: Neutron Flux on Edge of $1m\times1m$ 2D Setup in $1\times10^{-11}MeV$ to $1.78\times10^{-5}MeV$ Energy Groups using 128 Angles.

Additional insight into the discritization error as function of angular resolution can be gained by computing a L2 error norm where the PDT solution with 32768 discrete ordinates in the energy interval of interest is treated as the reference true solution instead of the MCNP solution. If MCNP was used as the reference solution there would be no way to isolate the angular-discretization error from the errors introduced by spatial and energy discretization. These errors plotted on logarithmic axes is given in Figure 6.53 for the $1m \times 1m$ geometry where the angular mesh width axis is defined as $\sqrt{\frac{4\pi}{\# angles}}$. sing the 32k angle quadrature set as the reference true solution, the

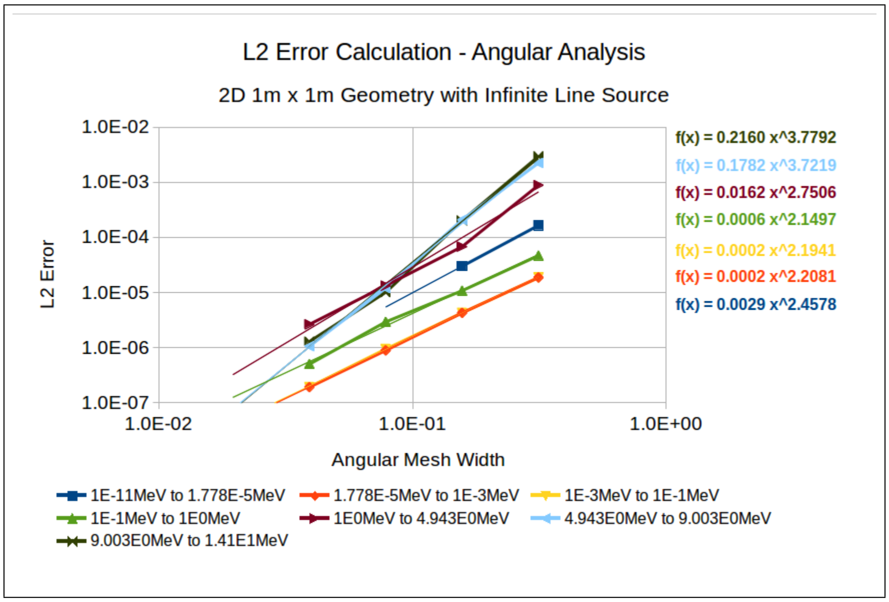

Figure 6.53: L2 Error Angular Analysis using PDT Solution with 32k Discrete Ordinates as Reference Solution in $1m \times 1m$.

L2 errors as function of angular resolution can be closely approximated with power functions. In general, the angular discretization errors are observed to be larger for the higher energy intervals. Additionally, the convergence rates are seen to be larger for higher energy intervals. One notable exception is seen with the thermal energy region, $1 \times 10^{-11} MeV$ to $1.78 \times 10^{-5} MeV$. It is currently unknown why the angular discretization error in the thermal energy interval is as large as it is, given that it visually looks smaller in the plots.

Similar results were seen in the $10m \times 10m$ geometry. The L2 error analysis for each energy interval using the 32k discrete ordinate PDT solution in that specified energy interval as the reference true solution is depicted in Figure 6.54. These L2 errors are seen to be closely approximated with power functions.

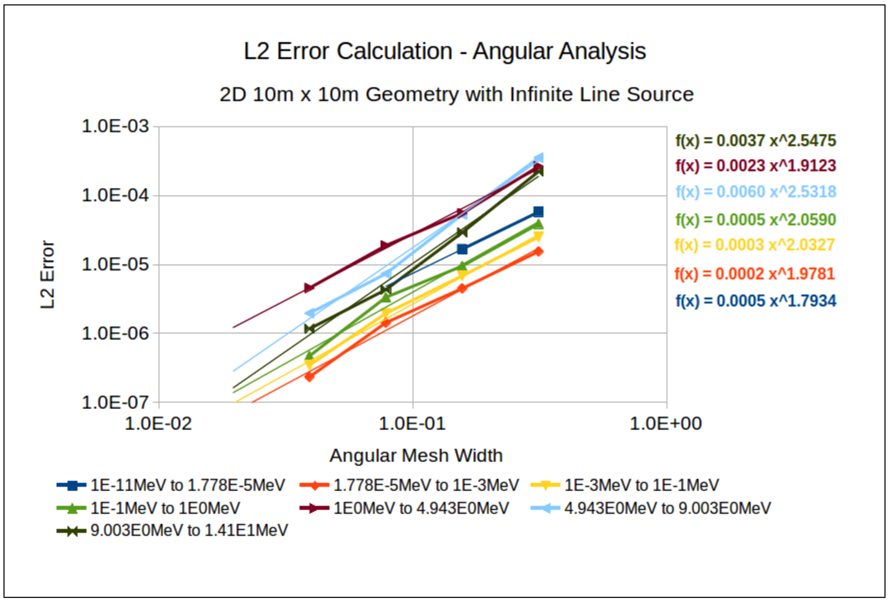

Figure 6.54: L2 Error Angular Analysis using PDT Solution with 32k Discrete Ordinates as Reference Solution in $10m \times 10m$.

6.2.3 Energy Dependent Flux

Taking another look at the energy group structure, the energy dependent flux was plotted at the center cell and at the outer corner cell of both the $1m \times 1m$ and $10m \times 10m$ 2D geometries. The data was obtained from simulations using 64^2 cells, 127 energy groups, and adequate angular resolution based on the angular analysis. For the angular resolution, 128 discrete angles were used for energy groups up to $1.78 \times 10^{-5} MeV$, 512 discrete angles were used for energy groups within $1.78 \times$

$10^{-5} MeV$ to $4.94 MeV$, 2048 discrete ordinates for energy groups from $4.94 MeV$ to $7.33 MeV$, and 8192 discrete angles for energy groups above $7.33 MeV$. Figures 6.55 and 6.56, outlines the energy dependent flux in the center and corner cells of the $1m \times 1m$ geometry. Although there are some slight differences present, overall good agreement is seen between the MCNP and PDT solutions.

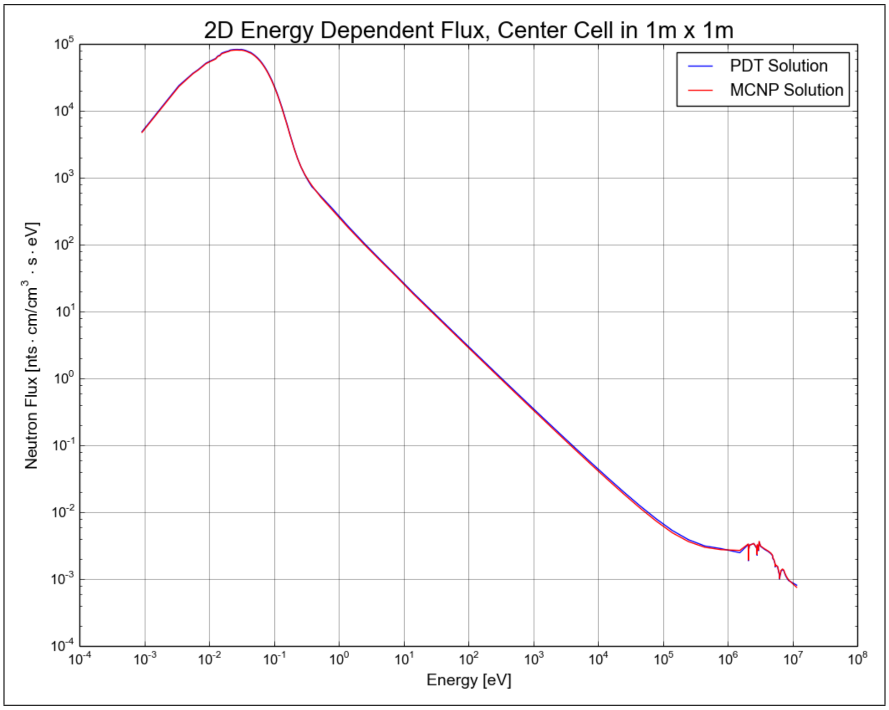

Figure 6.55: Energy Dependent Flux in Center Cell of $1m \times 1m$.

The energy dependent flux in the corner cell revealed non-smooth characteristics in the thermal range. At thermal energies, the kinetic energy of the neutrons are similar to energies of excitation in molecules and crystalline lattices. As result, the binding energies of molecular or crystalline lattices must be taken into account and the free-gas model is no longer appropriate. In Figure 5.2, it was seen that the elastic

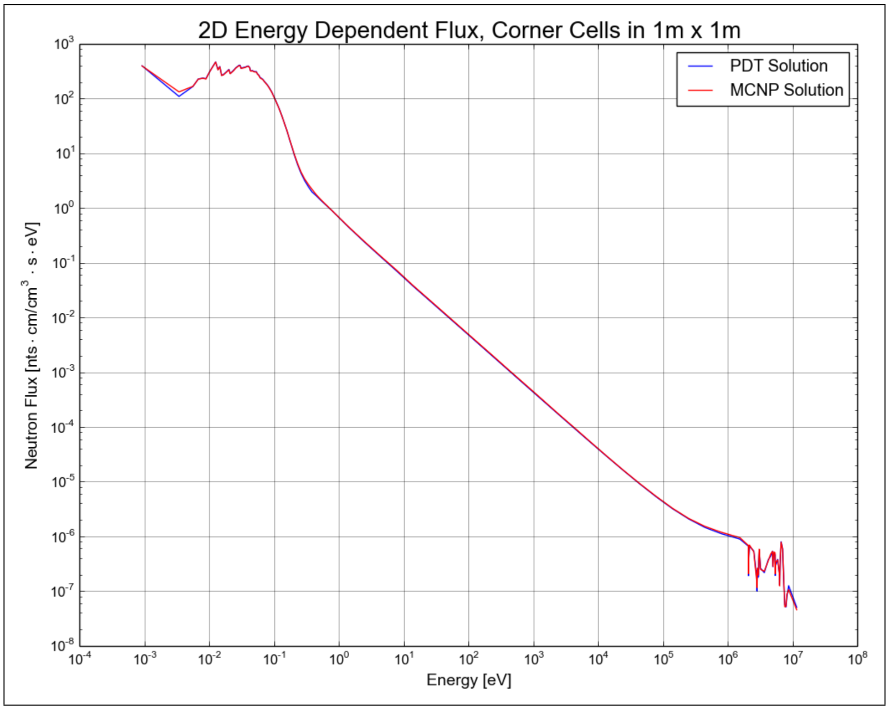

Figure 6.56: Energy Dependent Flux in Corner Cell of $1m \times 1m$.

coherent scattering cross-section for graphite has discontinuities, which are known as “Bragg edges”. These discontinuities perturb the shape of the energy dependent flux away from a Maxwellian in the corner cells where leakage is more dominant. In comparison, the jagged peaks are not present for the center cell. This is because in regions for which neutrons are far more likely to scatter than to leak or be absorbed, as is true near the center of this problem, the thermal flux must obtain a Maxwellian distribution, independent of the features of the total cross section. However, where neutrons have a higher probability of leaking, as is true near the corners, the flux spectrum is affected by the energy shape of the total cross section.

The energy dependent flux for the $10m \times 10m$ geometry is given in Figures 6.57 and 6.58 for the center and corner cells respectively. The energy dependent fluxes in

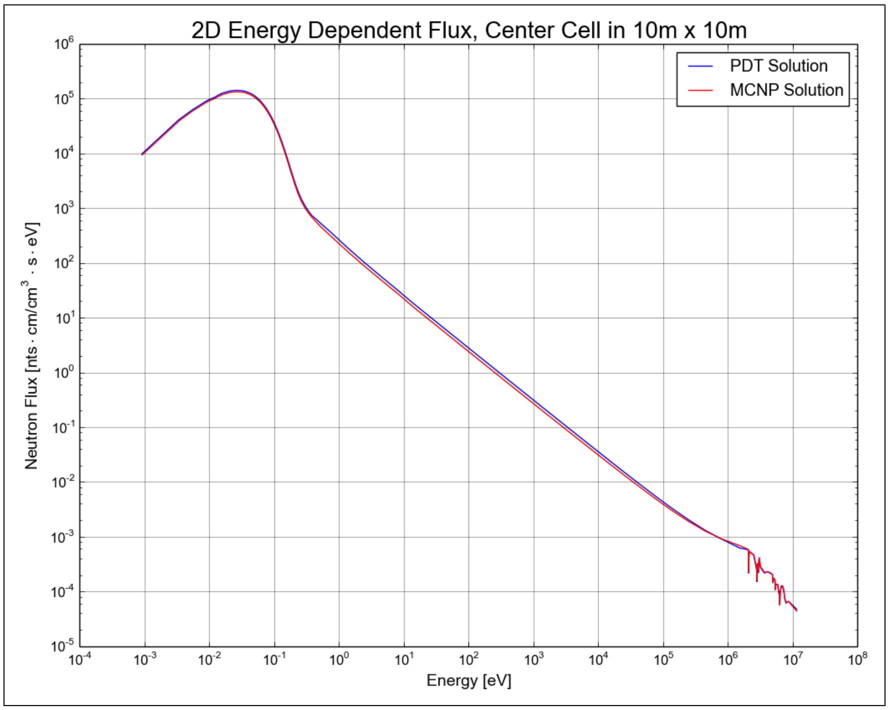

Figure 6.57: Energy Dependent Flux in Center Cell of $10m \times 10m$.

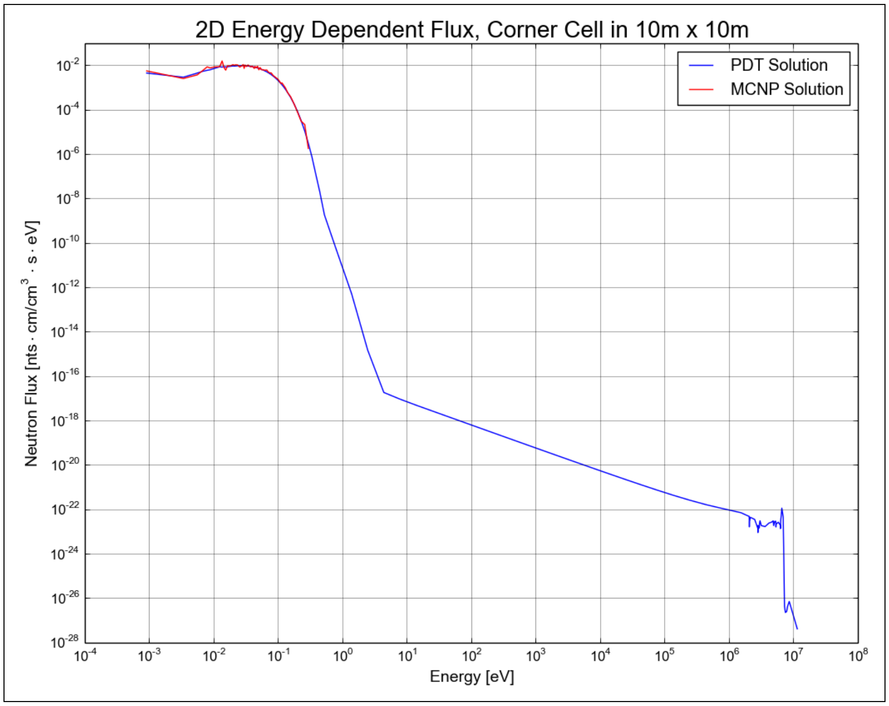

Figure 6.58: Energy Dependent Flux in Corner Cell of $10m \times 10m$.

the center cell of $10m \times 10m$ geometry have minor differences. For the corner cell of the $10m \times 10m$ geometry, the effect from the coherent scattering can be seen at the thermal energies. It is not as noticeable compared to the $1m \times 1m$ geometry because the $10m \times 10m$ geometry has larger cells across which the flux is being averaged. Additionally, the flux solution of the $10m \times 10m$ corner is seen to be strongly affected by leakage, which causes the slowing down region slope to become much flatter and results in a long Maxwellian tail that stretches from the Maxwellian peak down to the flattened slowing-down-range solution. The MCNP flux in the $10m \times 10m$ corner is seen to have fluctuations and then drops off completely around 0.2 eV. This is due to a weakness in the MCNP computation method: the simulated particles have trouble reaching regions many mean free paths away from the source.

6.3 3D Geometry Results

The last problem set looked at 3D geometry. $(1m)^3$ and $(10m)^3$ cubes were considered with an approximated centered AmBe point source with dimension of $(1cm)^3$. Independent spatial and angular resolution analyses were performed in the 3D geometry. 127 energy groups were used for the 3D spatial and angle discretization error calculations.

6.3.1 Spatial Analysis

The 3D spatial analysis looked at 4^3, 8^3, 16^3, 32^3, and 64^3 spatial cell refinement. 2048 discrete angles were used in all energy groups for the 3D spatial analysis calculations. Our study of angular discretization errors, described below, indicated that this number of angles generates an angular discretization error that is small compared to the spatial discretization error we study here. Just as was done with the 2D calculations, spatial flux plots were made for both PDT and MCNP by plotting the cell-averaged flux solutions at the cell-centered points. These points were connected to create a spatial surface plot of the neutron flux solution. The MCNP spatial neutron flux distribution, plotted at the midplane of the z-axis, is given in Figure 6.59. The MCNP solution peaks where the point source is located and then sharply decreases non-linearly away from the source. The slope of the spatial flux becomes less steep the farther it is away from the source. The PDT solution at midplane using 4^3, 8^3, 16^3, 32^3, and 64^3 spatial cell refinement is shown in Figures 6.60 through 6.64 respectively.

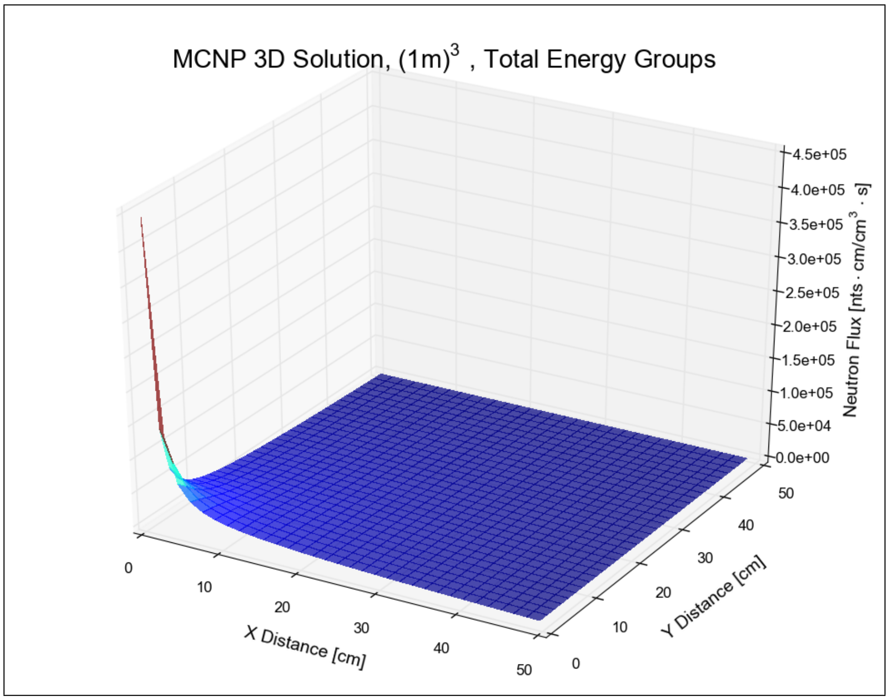

Figure 6.59: 3D MCNP Neutron Flux Solution at Midplane of $(1m)^3$.

The PDT solution clearly approaches the MCNP solution as more spatial cells are

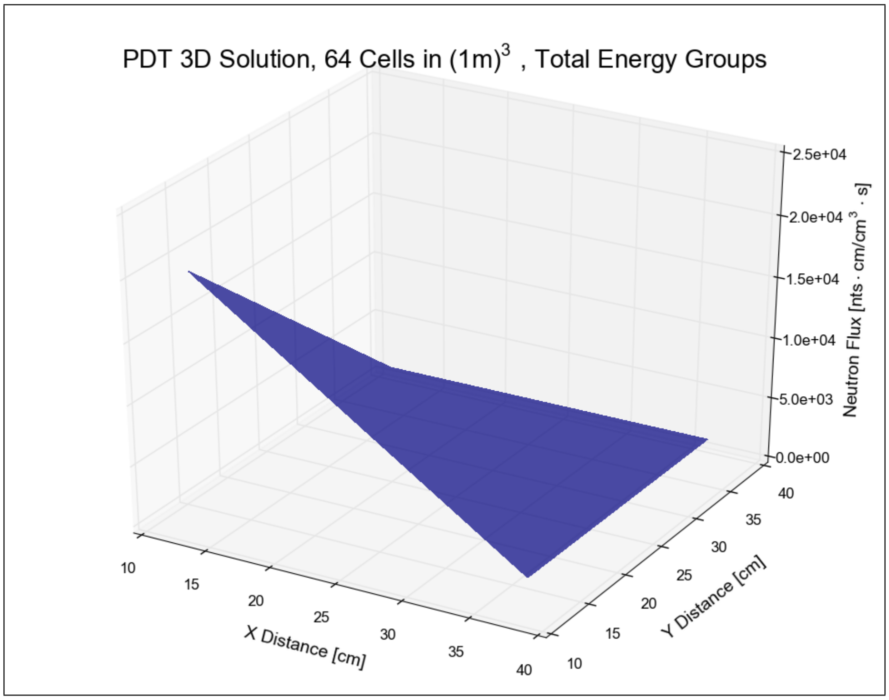

Figure 6.60: 3D PDT Neutron Flux Solution at Midplane of $(1m)^3$ using 4^3 Cells.

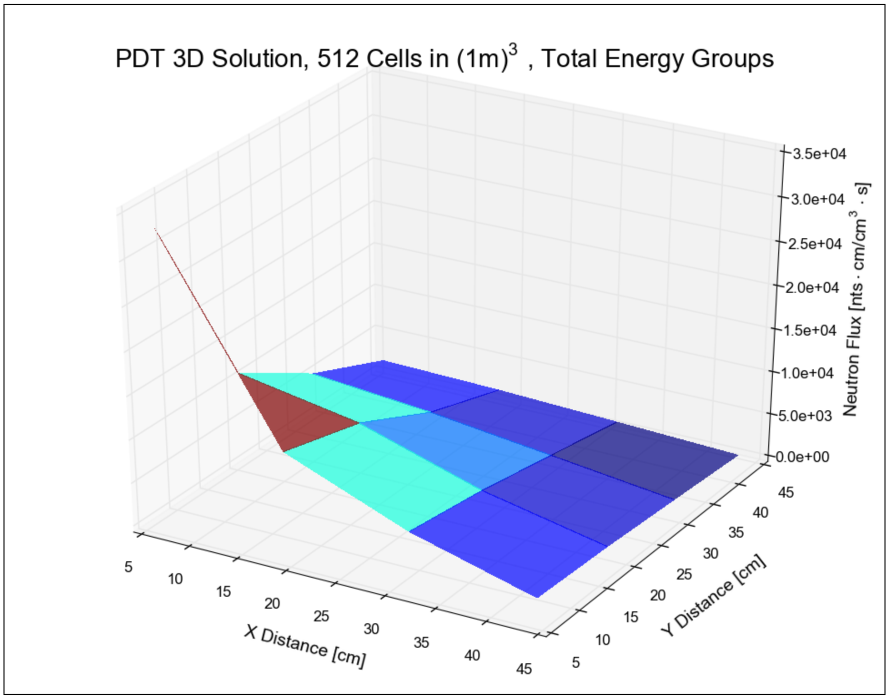

Figure 6.61: 3D PDT Neutron Flux Solution at Midplane of $(1m)^3$ using 8^3 Cells.

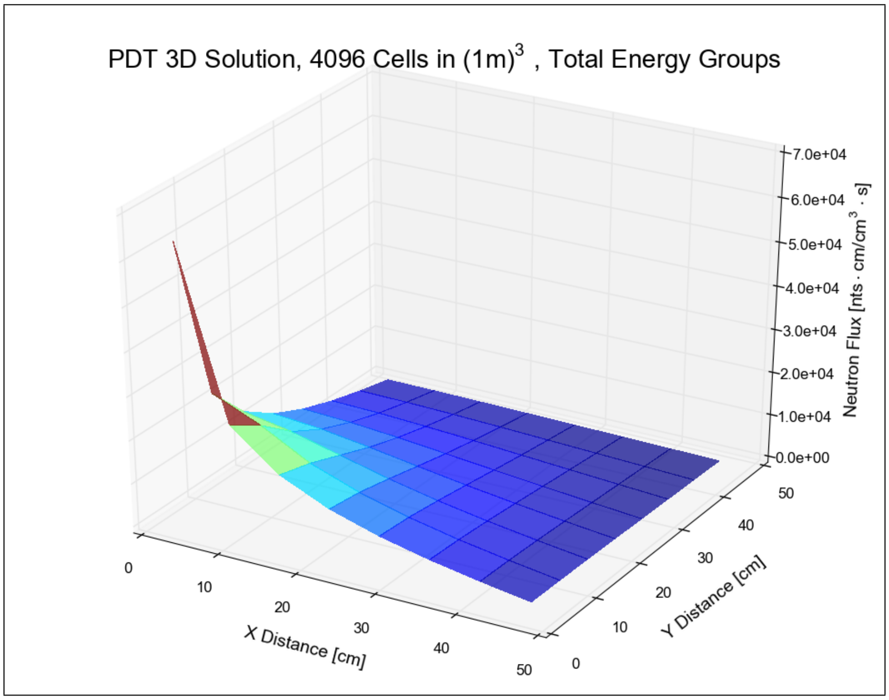

Figure 6.62: 3D PDT Neutron Flux Solution in $(1m)^3$ using 16^3 Cells.

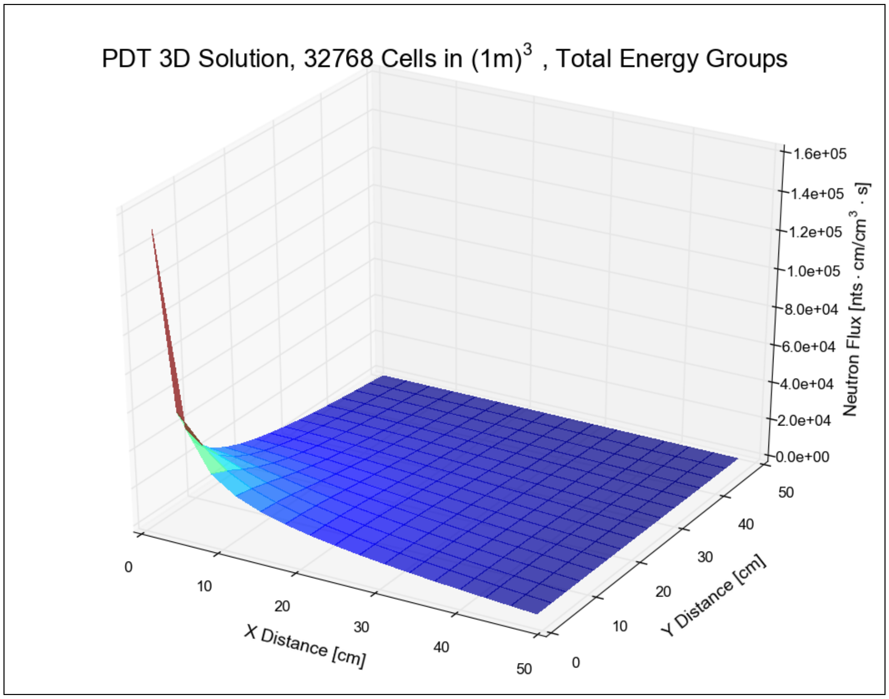

Figure 6.63: 3D PDT Neutron Flux Solution at Midplane of $(1m)^3$ using 32^3 Cells.

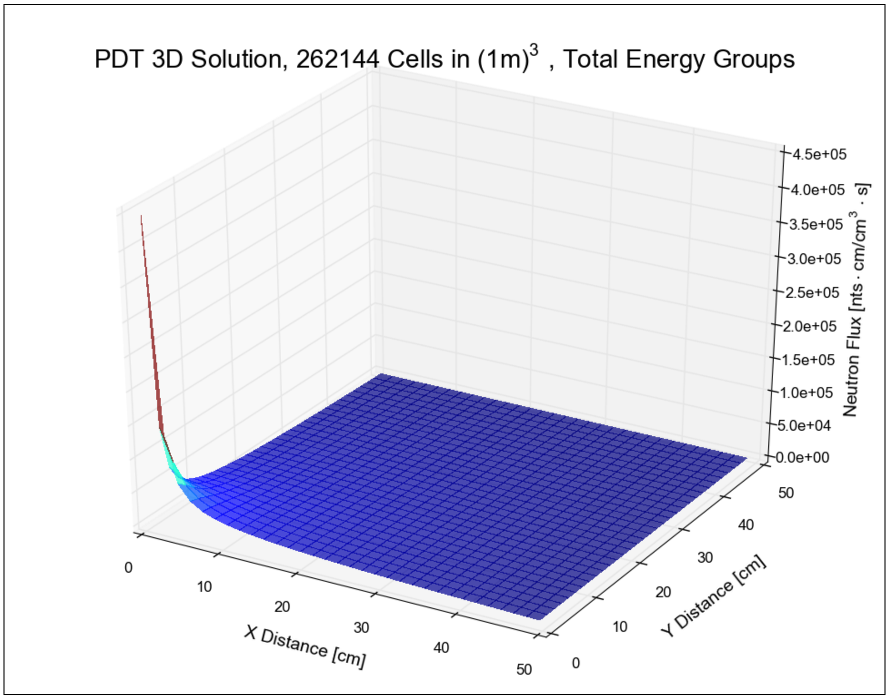

Figure 6.64: 3D PDT Neutron Flux Solution at Midplane of $(1m)^3$ using 64^3 Cells.

utilized. The MCNP and PDT neutron flux solutions using 64^3 cells are plotted on a logarithmic z-axis shown in Figures 6.65 and 6.66. In these figures, it is apparent that using 64^3 cells results in very similar PDT and MCNP neutron flux distributions at midplane.

The 64^3 cells MCNP and PDT neutron flux distributions at the top of the cube is shown in Figures 6.67 and 6.68. Using the 64^3 spatial refinement, very similar MCNP and PDT neutron flux distributions are seen at the top of the $(1m)^3$ cube. Also, the neutron flux distributions are seen to be a lot flatter compared to the neutron flux distribution at midplane. This is expected since the point source is located at the center of the midplane.

Equation 4.1 was utilized in order to compute the L2 discretization error using MCNP

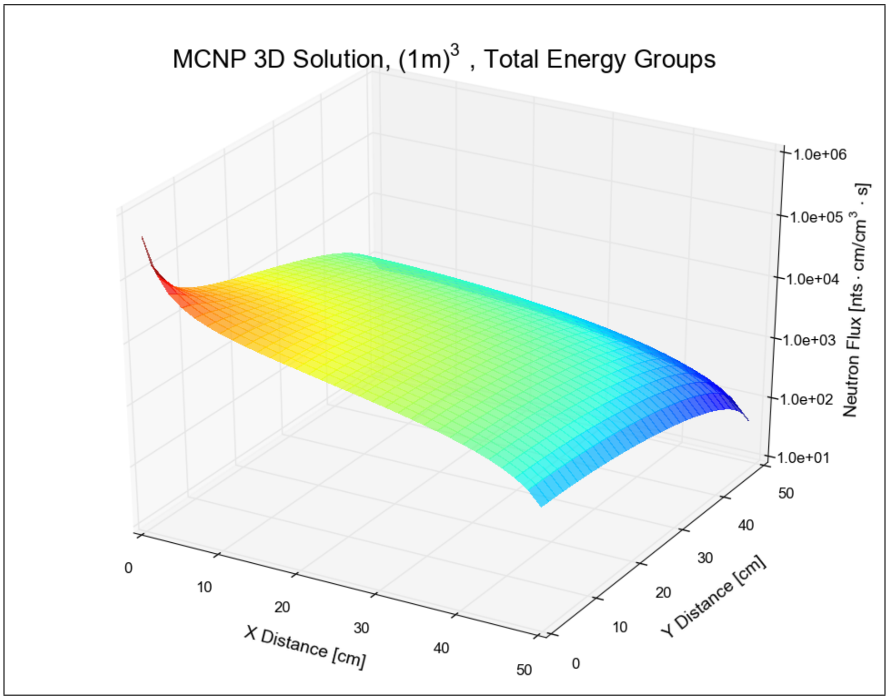

Figure 6.65: 3D MCNP Neutron Flux Solution at Midplane of $(1m)^3$.

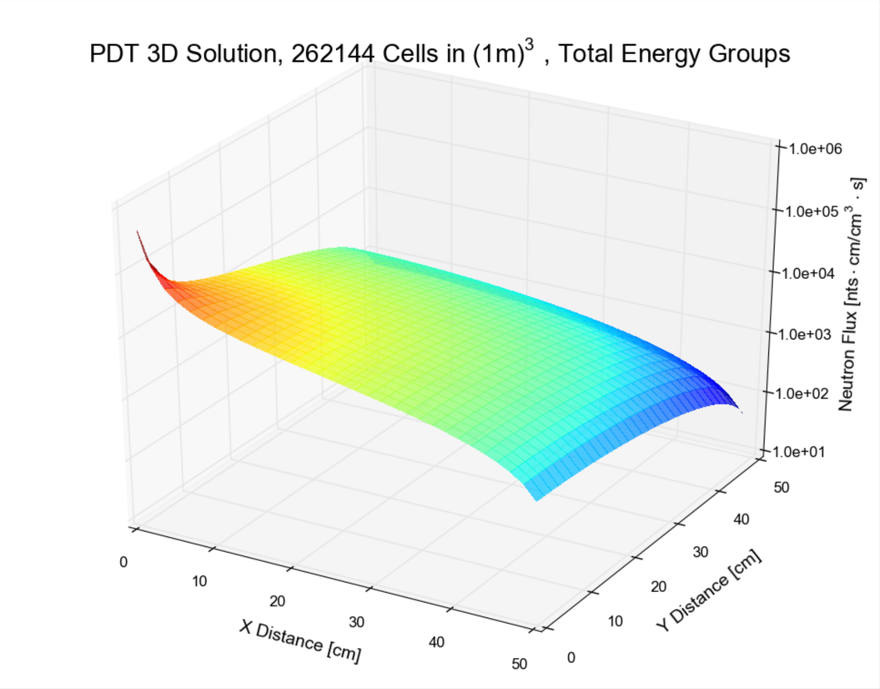

Figure 6.66: 3D PDT Neutron Flux Solution at Midplane of $(1m)^3$ using 64^3 Cells.

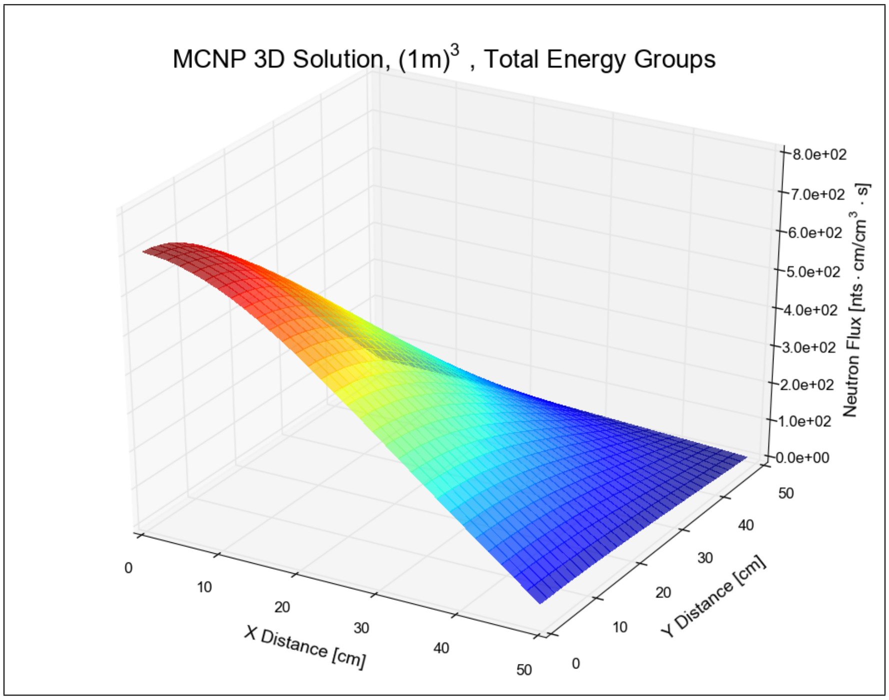

Figure 6.67: 3D MCNP Neutron Flux Solution at Top of $(1m)^3$.

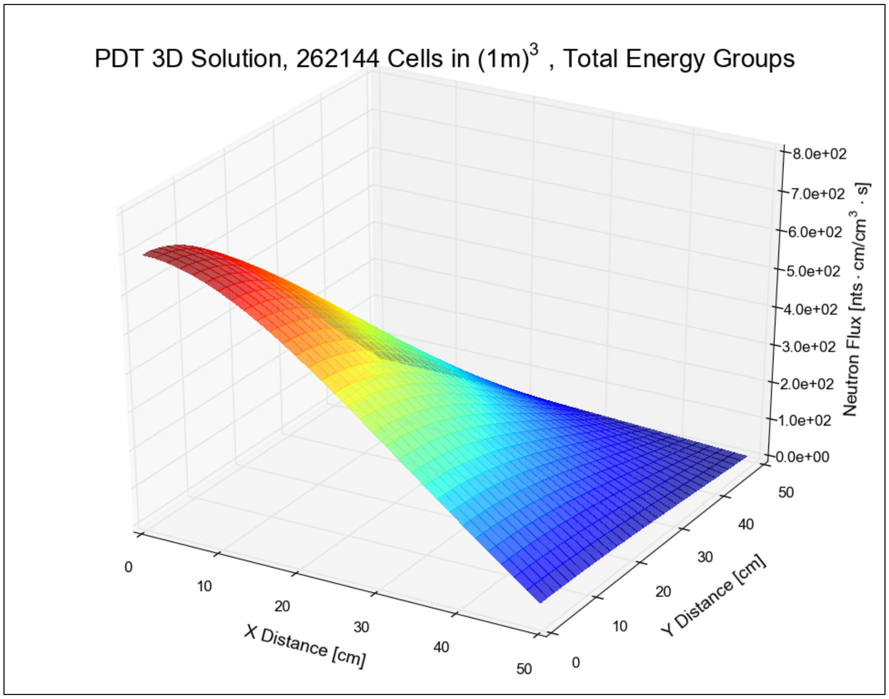

Figure 6.68: 3D PDT Neutron Flux Solution at Top of $(1m)^3$ using 64^3 Cells.

on a matching spatial mesh as the true solution. The L2 error for the $(1m)^3$ cube with varying spatial mesh refinements is outlined in Table 6.3. It is seen in Table 6.3,

Table 6.3: L2 Error Spatial Analysis in $(1m)^3$.

Problem	Cells	Cell Width [m]	L2 error	Convergence Rate	Error Ratio
4x4x4	64	0.2500	0.9112		
8x8x8	512	0.1250	0.7654	0.2515	1.1904
16x16x16	4096	0.0625	0.6517	0.2320	1.1744
32x32x32	32768	0.0313	0.4968	0.3915	1.3117
64x64x64	262144	0.0156	0.0669	2.8929	7.4276

that the error decreases with increasing number of spatial cells. Similar to the 2D geometry, the convergence rate is seen to be initially very low in the very coarse mesh, but increases with increasing spatial refinement. Going from 32x32x32 to 64x64x64 spatial refinement, the convergence rate is 2.89. The error was reduced by a factor of 7.4 when 8 times more cells were added when going from 32x32x32 to 64x64x64 spatial refinement. The L2 error as function of spatial refinement is plotted in Figure 6.69, along with a dashed line showing a second-order slope.

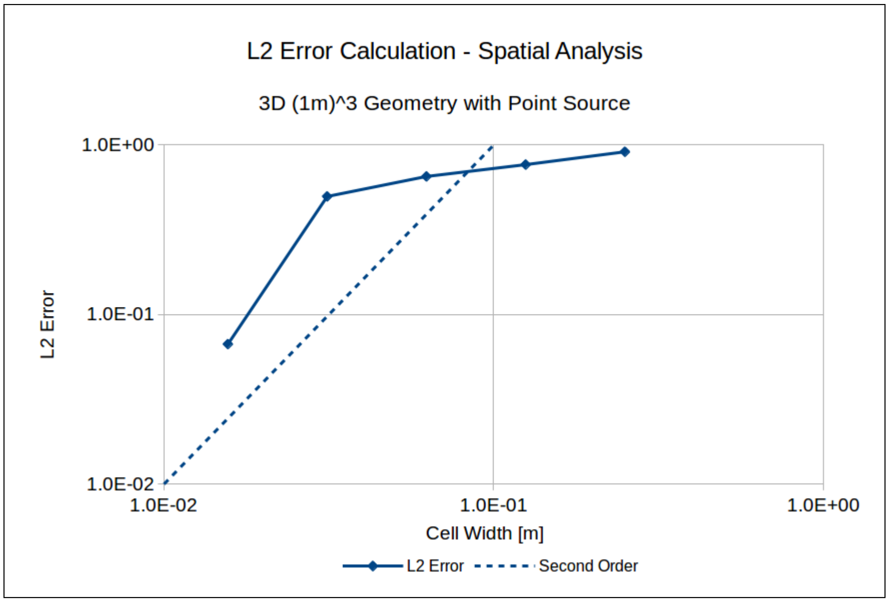

Figure 6.69: L2 Norm Error Spatial Analysis in $(1m)^3$.

Next, the $(10m)^3$ geometry is considered. The MCNP neutron flux at midplane of $(10m)^3$ geometry is plotted in Figure 6.59 on a 64^3 grid. Similar to the $(1m)^3$ results, the MCNP neutron flux distribution is highest where the point source is located and decreases rapidly away from the source. The PDT neutron flux solutions for $(10m)^3$ geometry with increasing spatial refinement are shown in Figures 6.71 through 6.75.

As expected with increasing spatial refinement, the PDT solution approaches the MCNP solution. Logarithmic plots of the neutron flux distribution using 64^3 cells are shown in Figures 6.76 and 6.77 for the MCNP and PDT solutions respectively. It is apparent that the MCNP and PDT neutron flux distributions at midplane are comparable when using 64^3 cells resolution.

The neutron flux distribution at the top of the cube using 64^3 cells is shown in Figures 6.78 and 6.79 for the MCNP and PDT solutions respectively. At the top

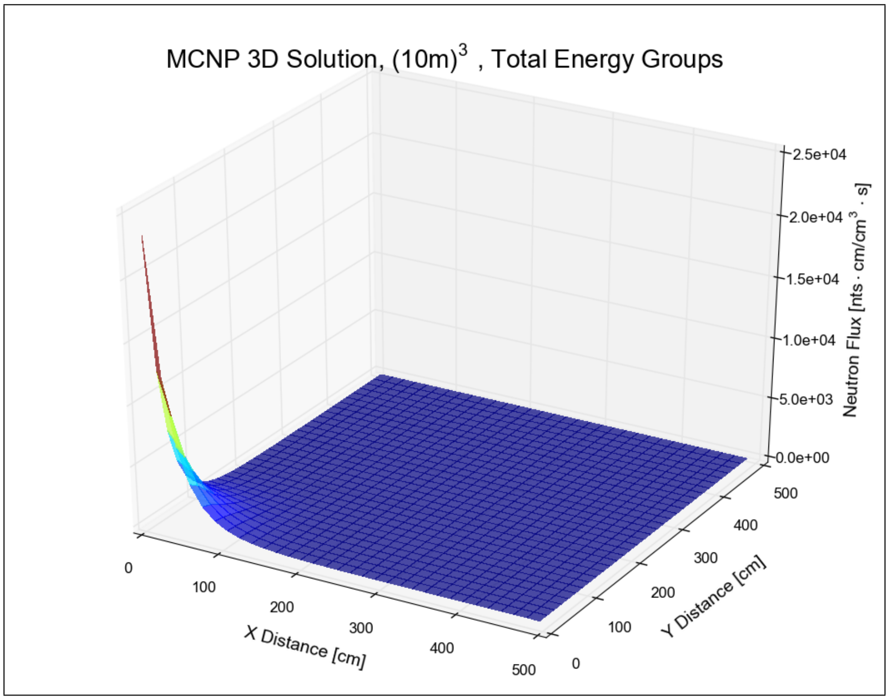

Figure 6.70: 3D MCNP Neutron Flux Solution at Midplane of $(10m)^3$.

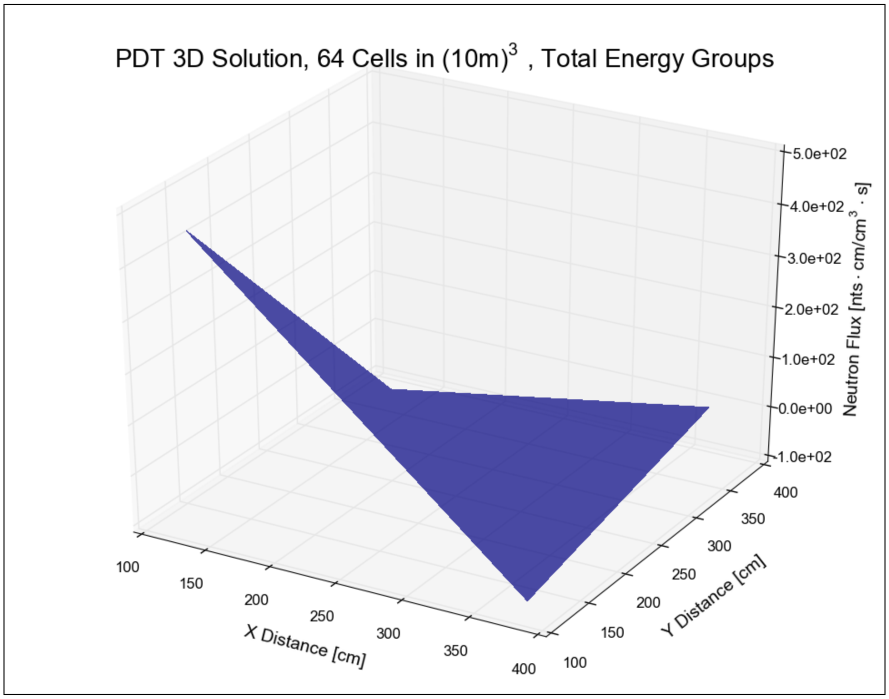

Figure 6.71: 3D PDT Neutron Flux Solution at Midplane of $(10m)^3$ using 4^3 Cells.

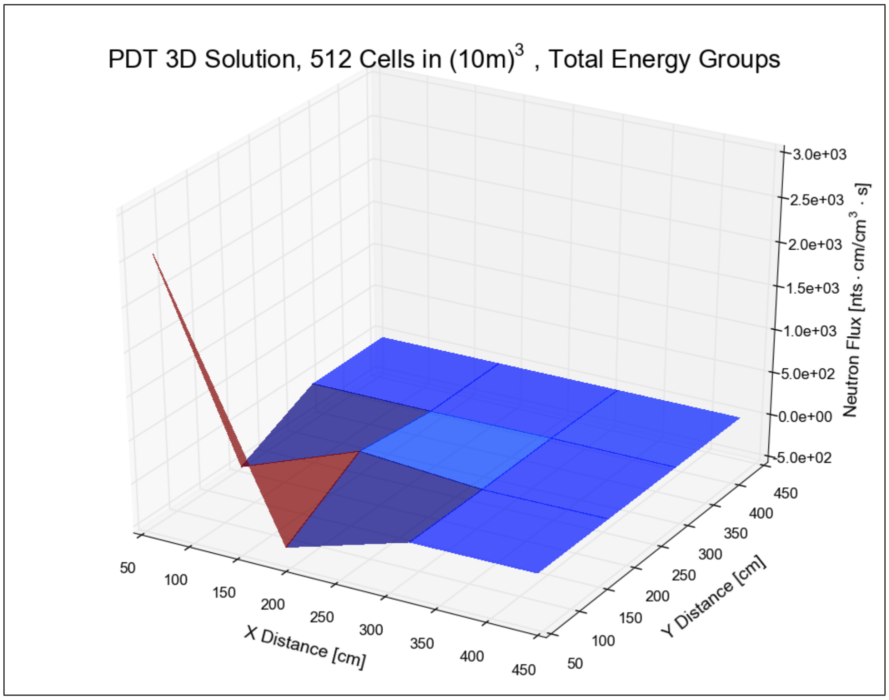

Figure 6.72: 3D PDT Neutron Flux Solution at Midplane of $(10m)^3$ using 8^3 Cells.

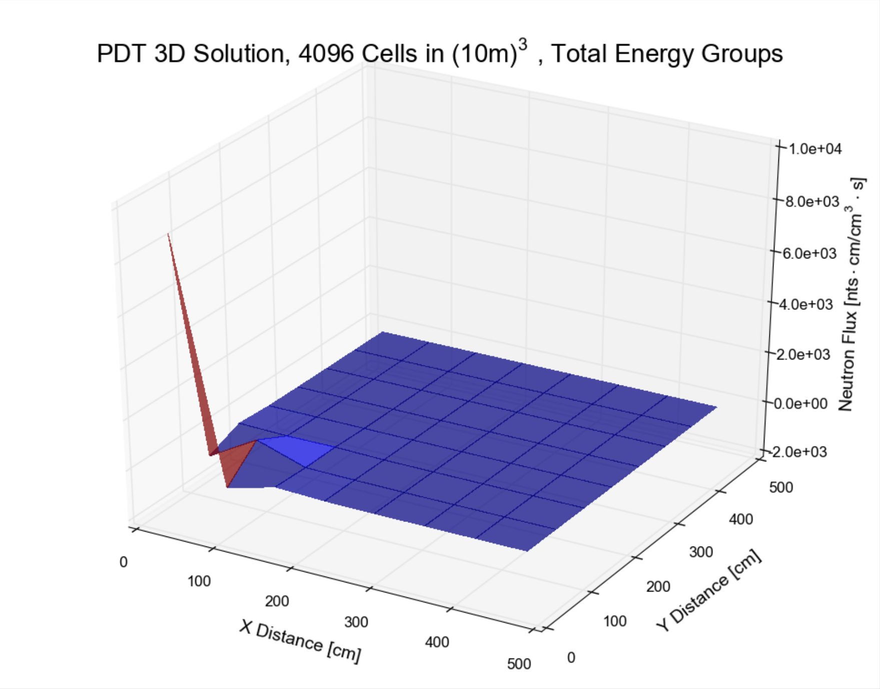

Figure 6.73: 3D PDT Neutron Flux Solution in $(1m)^3$ using 16^3 Cells.

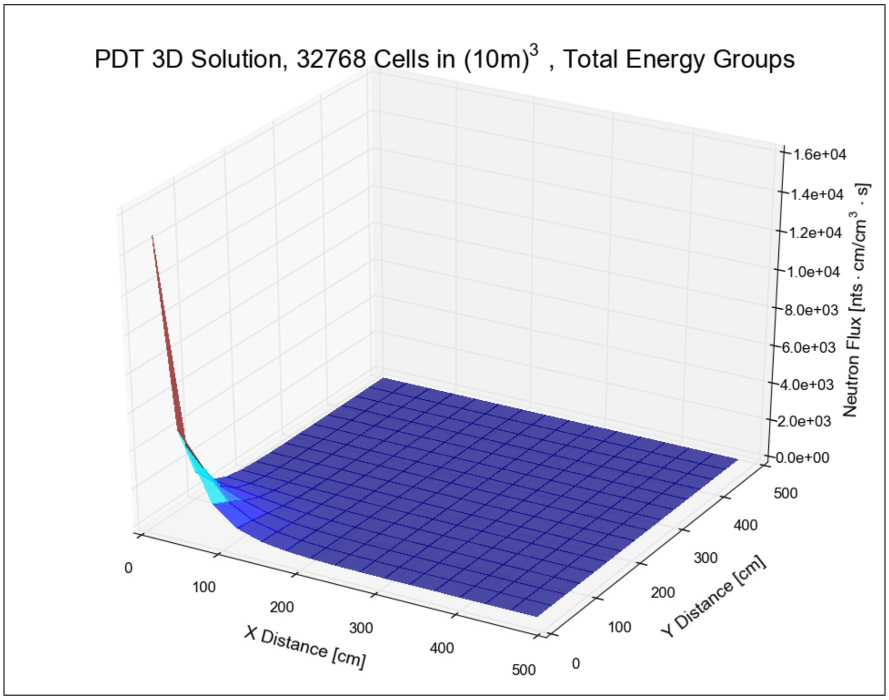

Figure 6.74: 3D PDT Neutron Flux Solution at Midplane of $(10m)^3$ using 32^3 Cells.

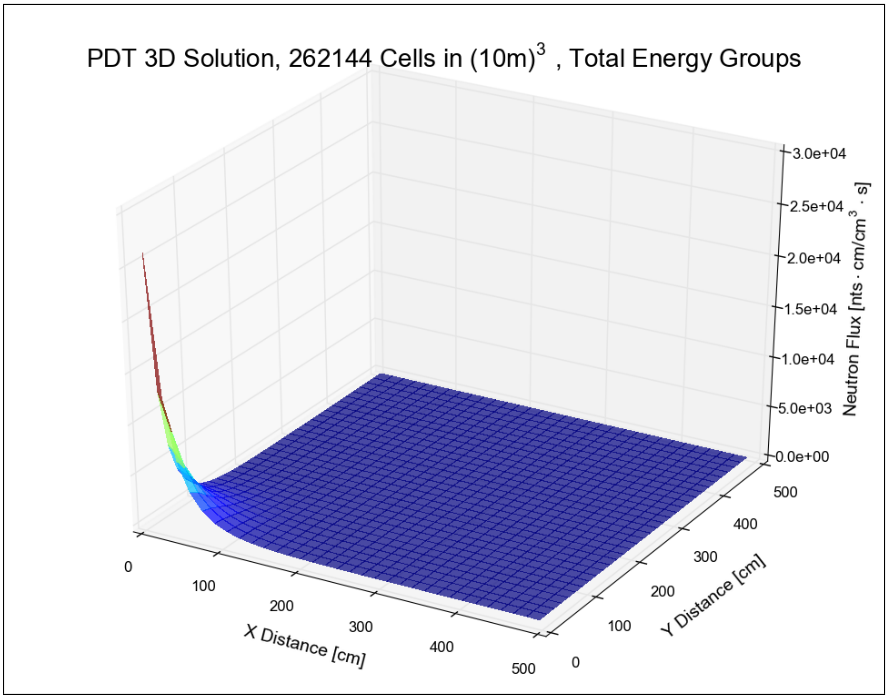

Figure 6.75: 3D PDT Neutron Flux Solution at Midplane of $(10m)^3$ using 64^3 Cells.

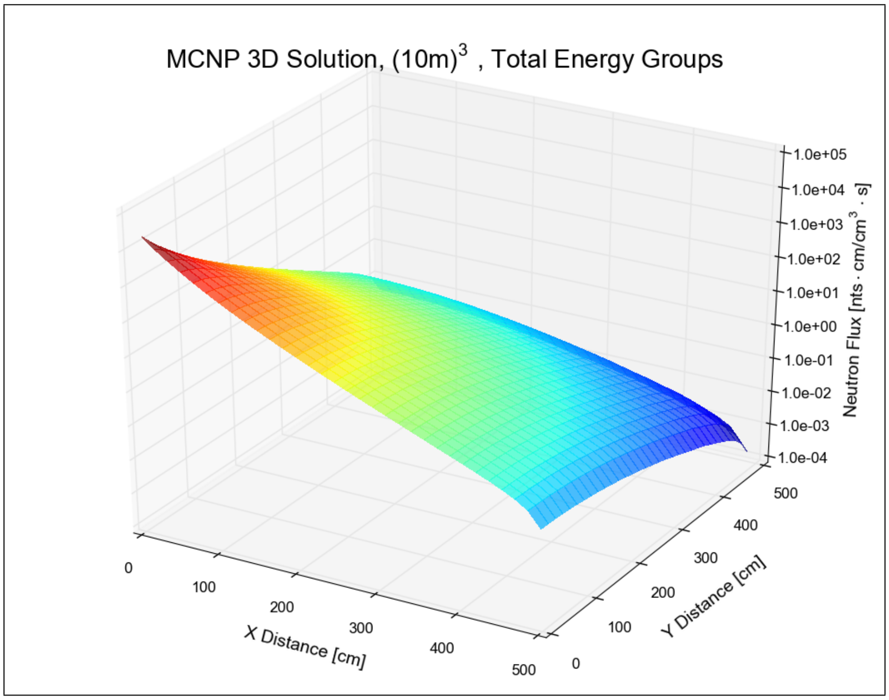

Figure 6.76: 3D MCNP Neutron Flux Solution at Midplane of $(10m)^3$.

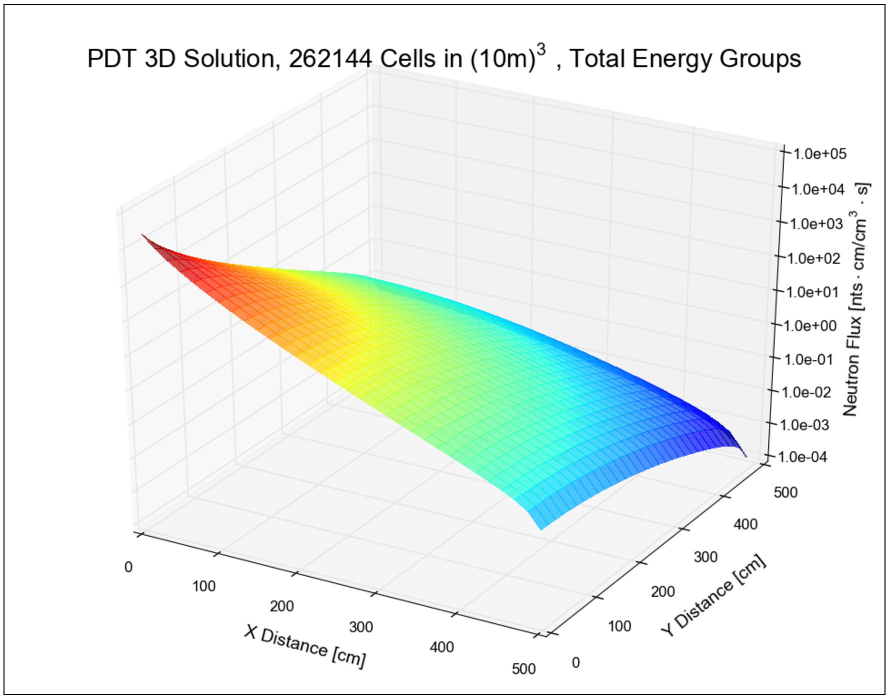

Figure 6.77: 3D PDT Neutron Flux Solution at Midplane of $(10m)^3$ using 64^3 Cells.

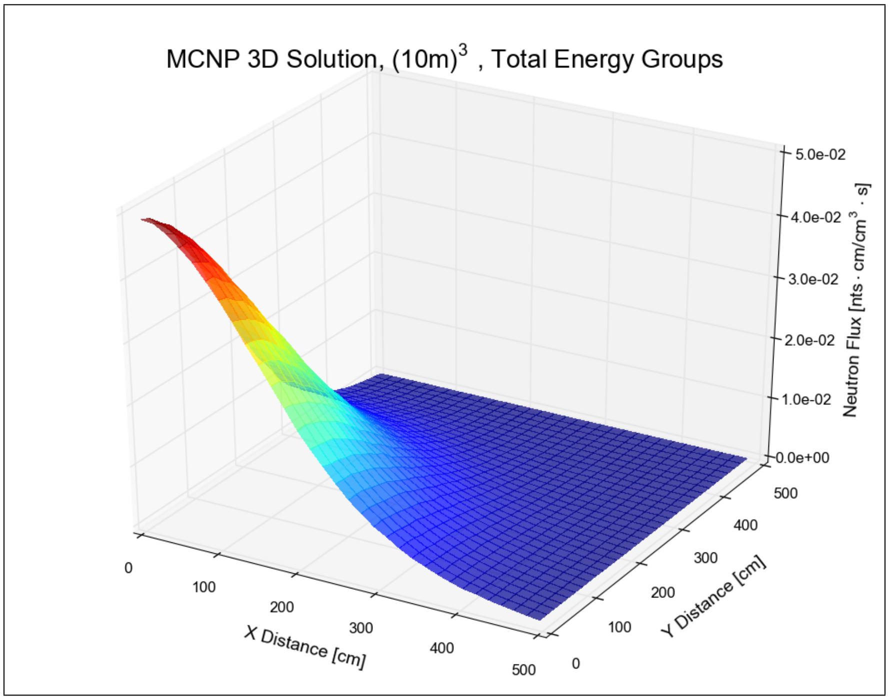

Figure 6.78: 3D MCNP Neutron Flux Solution at Top of $(10m)^3$.

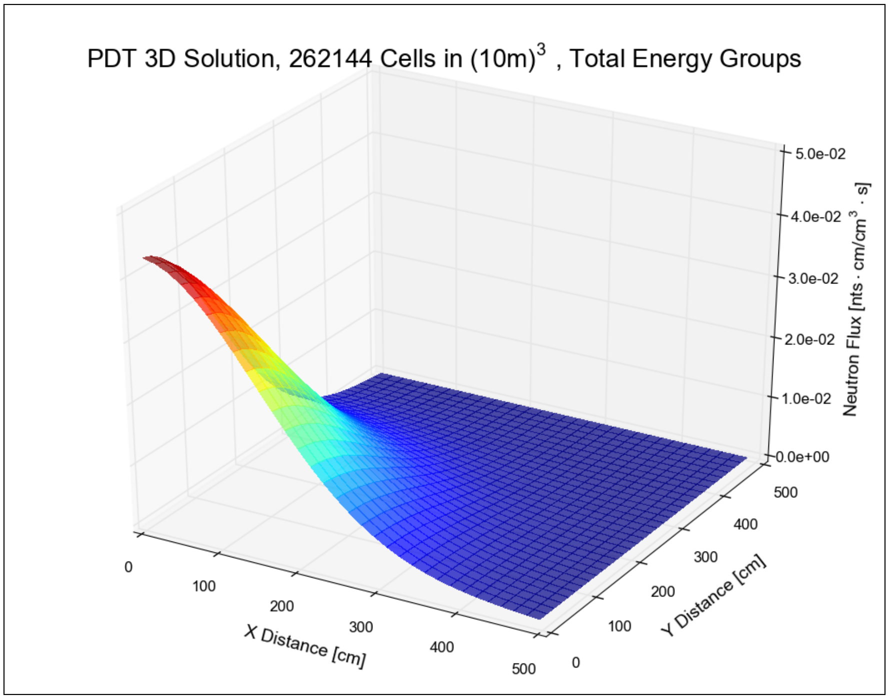

Figure 6.79: 3D PDT Neutron Flux Solution at Top of $(10m)^3$ using 64^3 Cells.

of the $(10m)^3$ cube, while still comparable, the PDT neutron flux distribution was found to be slightly less than the MCNP neutron flux distribution. Once again, the neutron flux distribution at top of the cube is seen to be flatter compared to the neutron flux distribution at midplane.

Table 6.4 depicts the L2 error as function of the number of spatial cells for the $(10m)^3$ cube, computed with Equation 4.1 where MCNP on a matching spatial grid was used as the true solution. As expected, increasing spatial refinement reduced the error. The convergence rate is low in the coarse mesh and increases with increasing spatial refinement to 2.90. The error ratio was 7.46 going to the 64x64x64 spatial refinement. The error as function of the cell width is plotted in Figure 6.80, along with a dashed line showing a second-order slope.

Table 6.4: L2 Error Spatial Analysis in $(10m)^3$.

Problem	Cells	Cell Width [m]	L2 error	Convergence Rate	Error Ratio
4x4x4	64	2.5000	1.2827		
8x8x8	512	1.2500	1.1930	0.0660	1.0752
16x16x16	4096	0.6250	1.0455	0.1904	1.1411
32x32x32	32768	0.3125	0.6470	0.6923	1.6158
64x64x64	262144	0.1563	0.0867	2.8997	7.4625

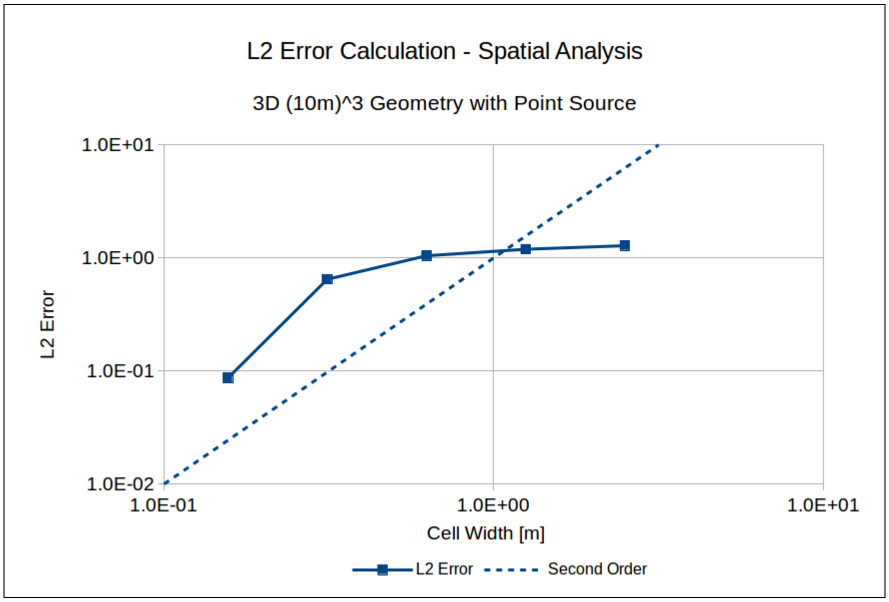

Figure 6.80: L2 Norm Error Spatial Analysis in $(10m)^3$.

6.3.2 Angular Analysis

For the 3D angular analysis, the same quadrature angle sets were utilized from the previous 2D angular analysis. These quadrature sets are shown in Table 4.2. The quadrature sets were tested independently in 7 energy intervals: $1 \times 10^{-11} MeV$, $1.78 \times 10^{-5} MeV$, $1 \times 10^{-3} MeV$, $0.1 MeV$, $1.0 MeV$, $4.94 MeV$, $9.0 MeV$, and $14.1 MeV$. Just as was done for the 2D angular analysis, in each energy range, an independent analysis was performed by varying the quadrature set in that specific energy range while keeping the quadrature set constant at 2048 angles in all other energy groups. This was done for the $(1m)^3$ geometry using 64^3 spatial cells and 127 energy groups. Ray effects become more dominant at distances farther from a localize source. Therefore, the spatial neutron flux distributions at the top of the cube rather than the midplane was analysed.

The MCNP neutron flux solution at the top of the $(1m)^3$ cube in the highest energy range, $9.0MeV$ to $14.1MeV$, is outlined in Figure 6.81. In comparison, the PDT solution at the top using the 128 angle set is shown in Figure 6.82. Significant spatial oscillations from ray effects are apparent in the PDT neutron flux using 128 angles. Most of these visible ray effects are resolved in the PDT neutron flux using a 512 angle quadrature set as displayed in Figure 6.83. With 2048 angles, the rest of the noticeable ray effects are gone as seen in Figure 6.84. Close agreement is seen between MCNP and PDT using the 2048 angle quadrature set.

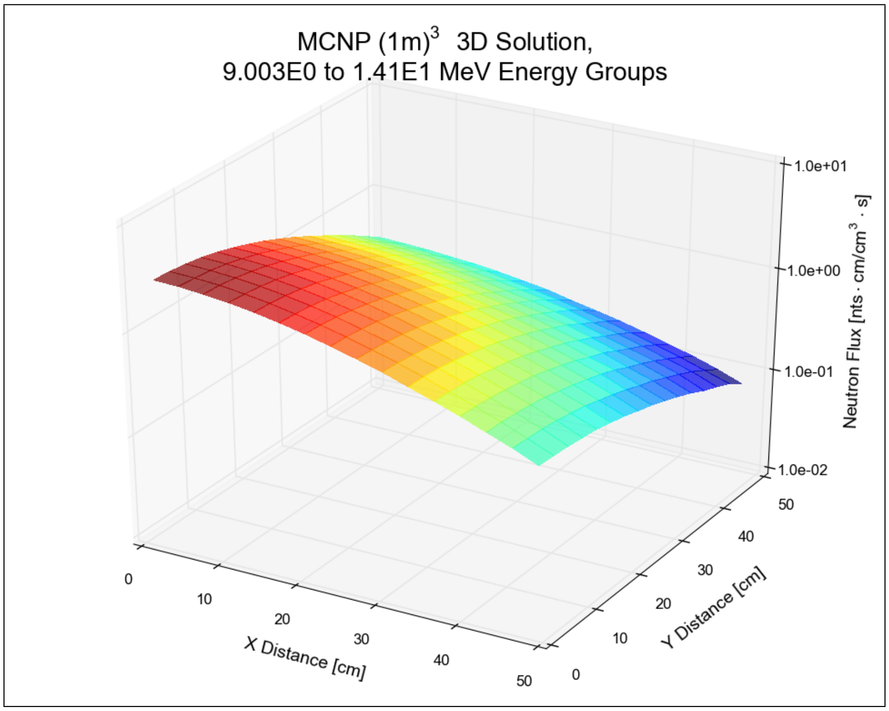

Figure 6.81: MCNP $(1m)^3$ 3D Neutron Flux Solution at Top in $9.0MeV$ to $14.1MeV$ Energy Groups.

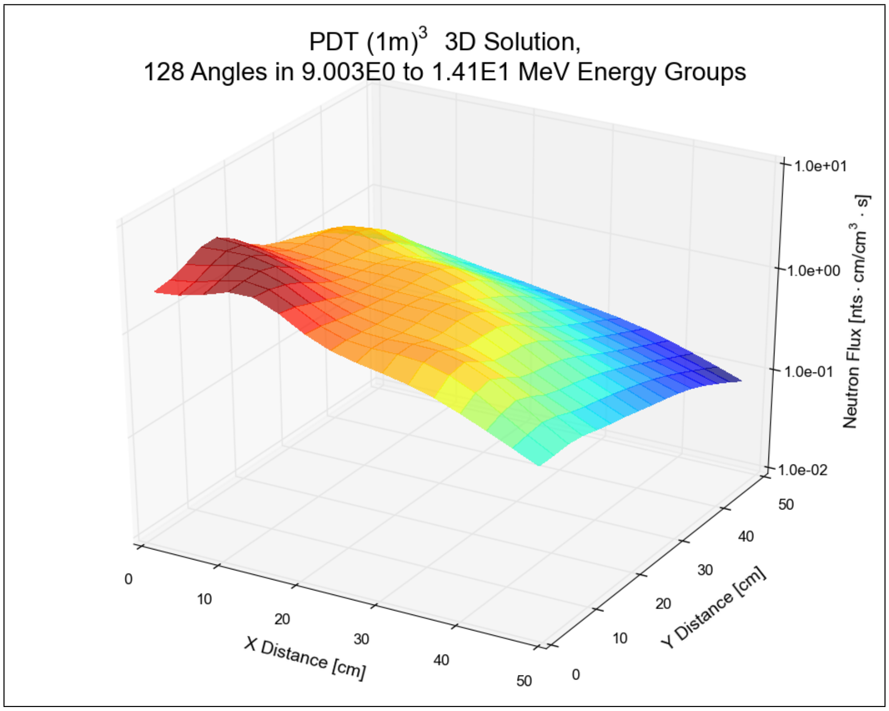

Figure 6.82: PDT $(1m)^3$ 3D Neutron Flux Solution at Top in $9.0MeV$ to $14.1MeV$ Energy Groups using 128 Angles.

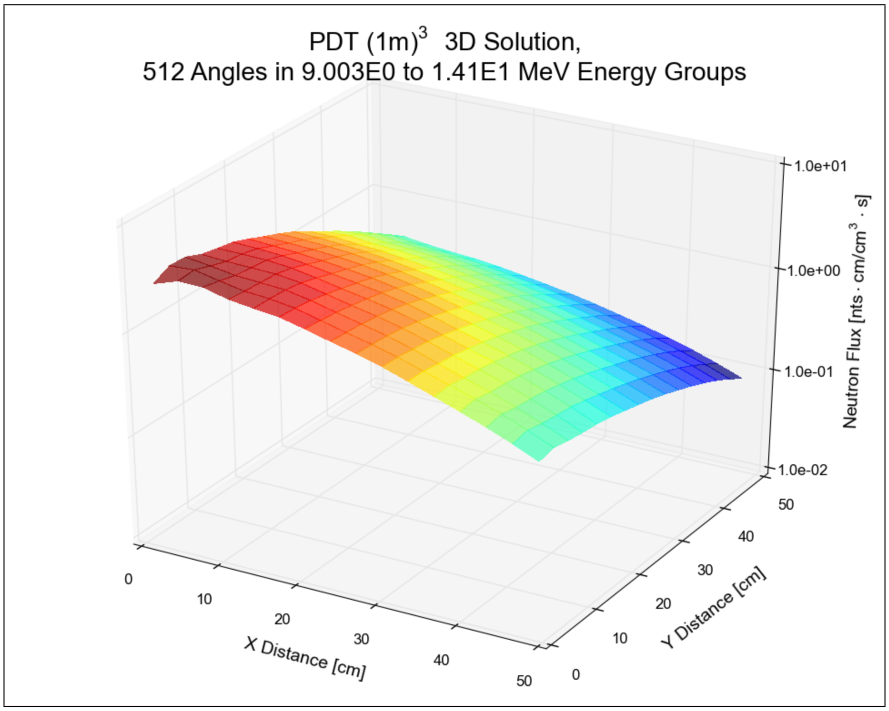

Figure 6.83: PDT $(1m)^3$ 3D Neutron Flux Solution at Top in $9.0MeV$ to $14.1MeV$ Energy Groups using 512 Angles.

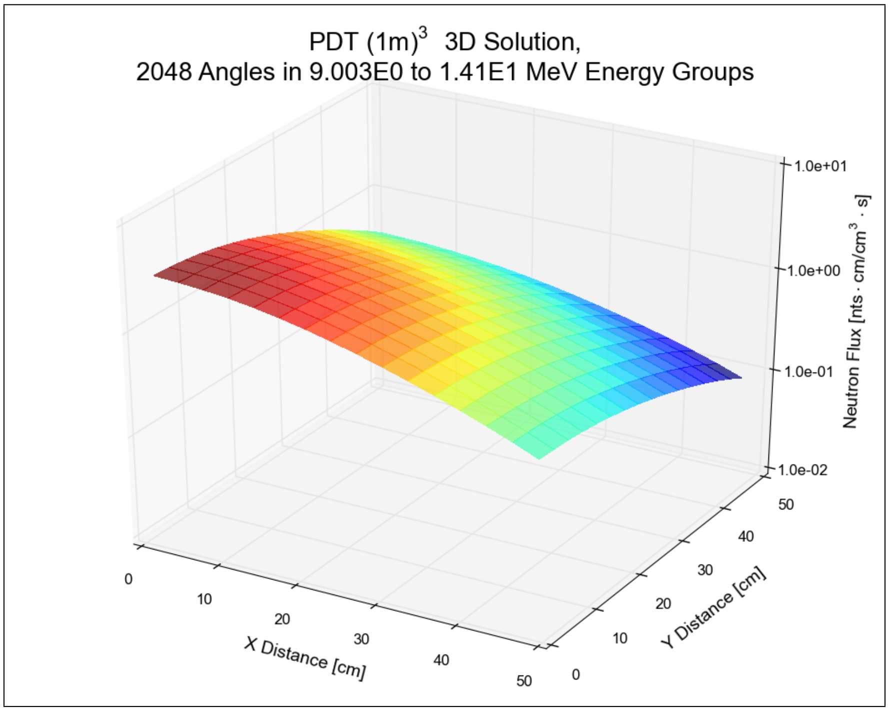

Figure 6.84: PDT $(1m)^3$ 3D Neutron Flux Solution at Top in $9.0MeV$ to $14.1MeV$ Energy Groups using 2048 Angles.

The MCNP solution at top of $(1m)^3$ cube for the $4.9MeV$ to $9.0MeV$ energy range is given in Figure 6.85. The PDT solution using 128 angles, shown in Figure 6.86, has major ray effects. Once again, these ray effects were mostly resolved using the higher quadrature set of 512 angles as seen in Figure 6.87. The last of the ray effects were resolved in the 2048 angle quadrature set shown in Figure 6.88.

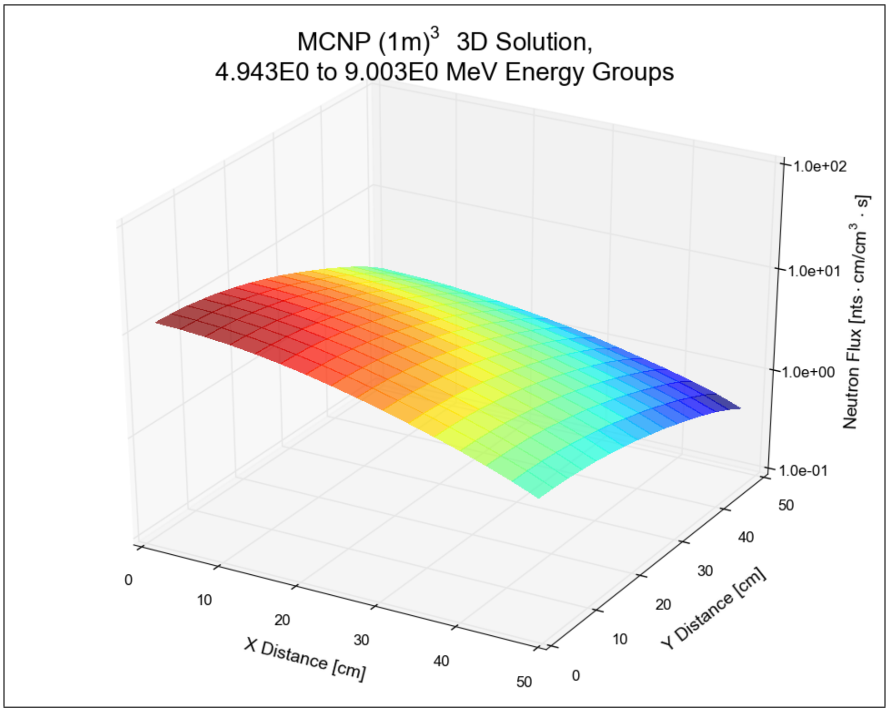

Figure 6.85: MCNP $(1m)^3$ 3D Neutron Flux Solution at Top in $4.9MeV$ to $9.0MeV$ Energy Groups.

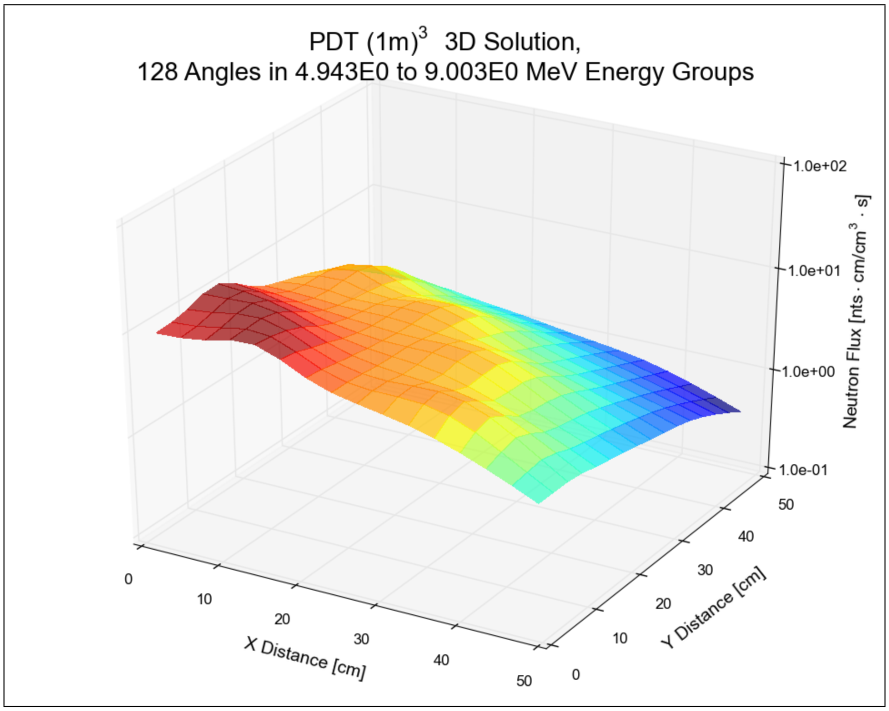

Figure 6.86: PDT $(1m)^3$ 3D Neutron Flux Solution at Top in $4.9MeV$ to $9.0MeV$ Energy Groups using 128 Angles.

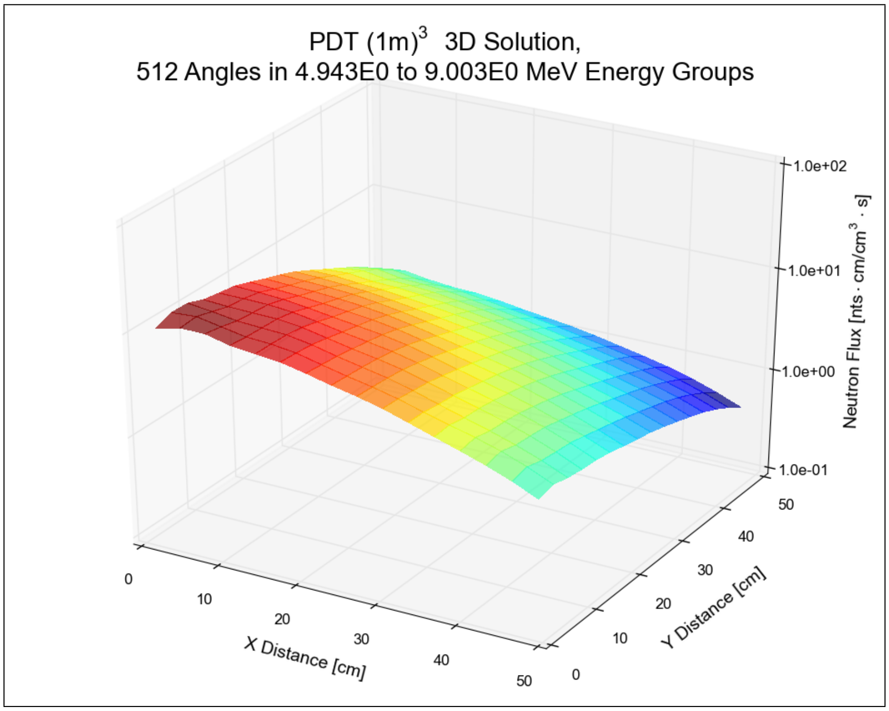

Figure 6.87: PDT $(1m)^3$ 3D Neutron Flux Solution at Top in $4.9MeV$ to $9.0MeV$ Energy Groups using 512 Angles.

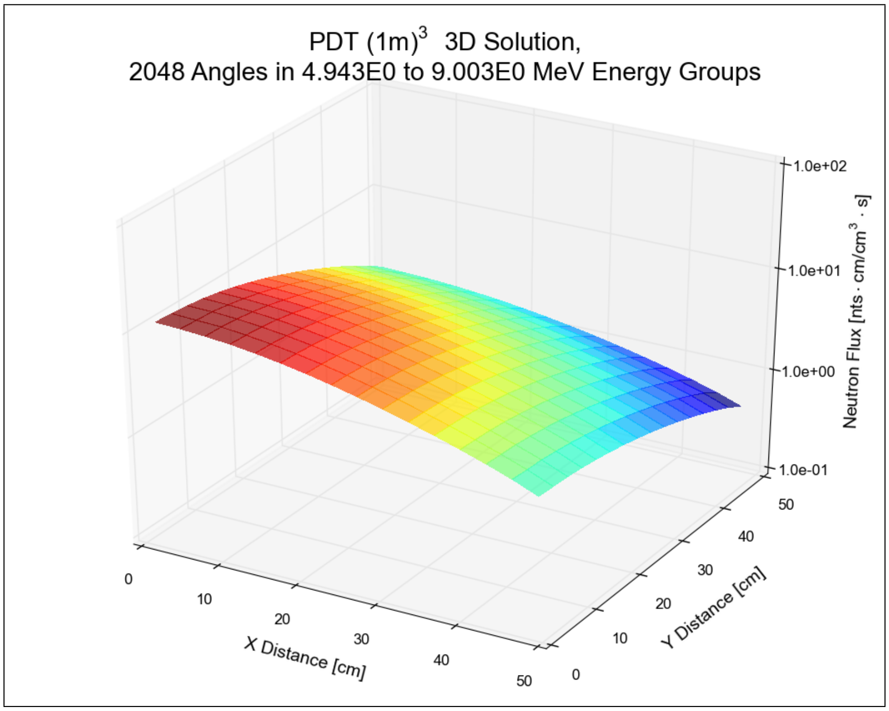

Figure 6.88: PDT $(1m)^3$ 3D Neutron Flux Solution at Top in $4.9MeV$ to $9.0MeV$ Energy Groups using 2048 Angles.

The MCNP neutron flux at the top of the $(1m)^3$ cube using energy group set, $1.0MeV$ to $4.9MeV$ is shown in Figure 6.89. In contrast to the higher energy groups, the PDT flux using 128 angles, plotted in Figure 6.90, does not show any notable ray effects. Since ray effects become less dominant at lower neutron energies, the lower energy groups will also not have visible ray effects in the spatial neutron flux using the 128 angle quadrature set.

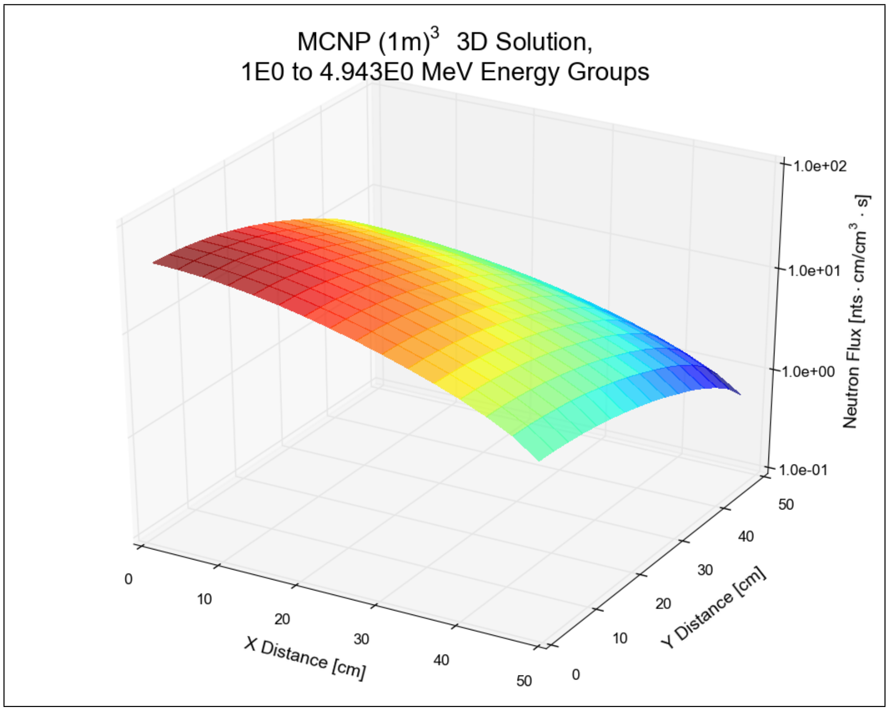

Figure 6.89: MCNP $(1m)^3$ 3D Neutron Flux Solution at Top in $1.0MeV$ to $4.9MeV$ Energy Groups.

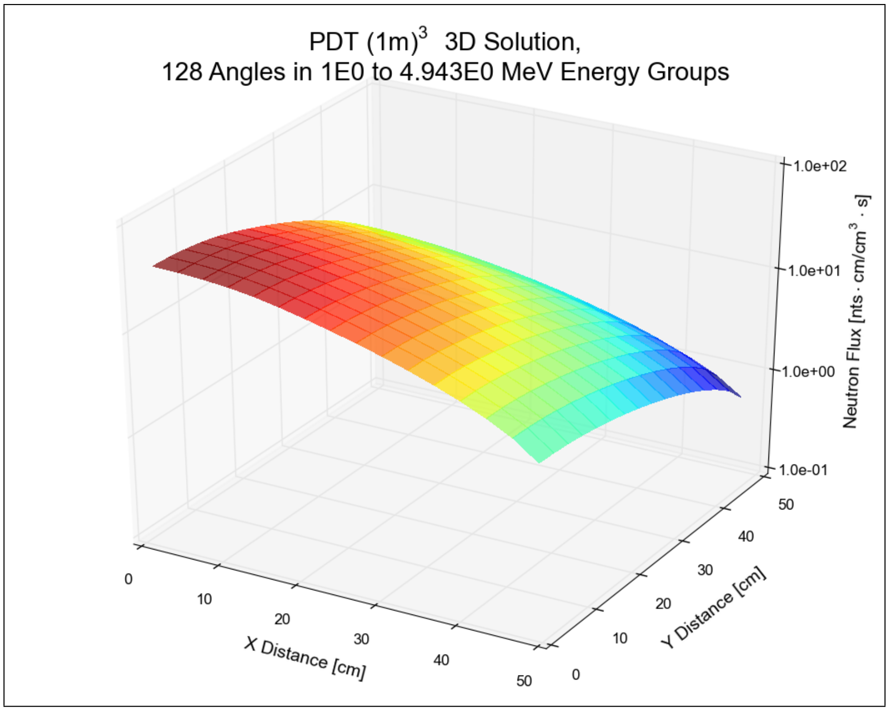

Figure 6.90: PDT $(1m)^3$ 3D Neutron Flux Solution at Top in $1.0MeV$ to $4.9MeV$ Energy Groups using 128 Angles.

The ray effects can also be clearly seen by looking at the neutron flux alongside one of the outer edges. Figures 6.91 through 6.94 outline the neutron flux at midplane along side an outer edge in the fast energy groups $4.9MeV$ to $9.0MeV$ using the 128, 512, 2048, and 8192 angle quadrature sets respectively. It is clear that in the $4.9MeV$ to $9.0MeV$ energy groups, PDT has significant error when utilizing only the 128 angle quadrature set. Utilizing the 512 quadrature set removed the majority of the ray effects as shown in Figure 6.92. Further error reduction was found using the 2048 angles shown in Figure 6.93 and finally in the 8192 angle set shown in Figure 6.94.

In comparison the neutron flux in thermal energy groups $1 \times 10^{-11}MeV$ to $1.78 \times 10^{-5}MeV$, is shown in Figure 6.95.

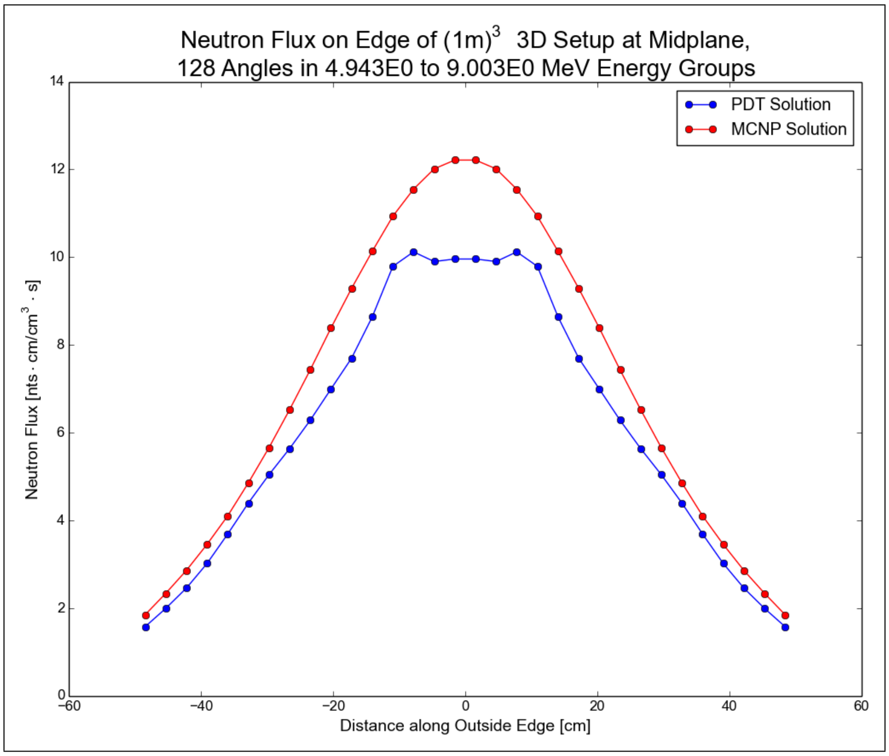

Figure 6.91: Neutron Flux on Edge of $(1m)^3$ 3D Setup at Midplane in $4.9MeV$ to $9.0MeV$ Energy Groups using 128 Angles.

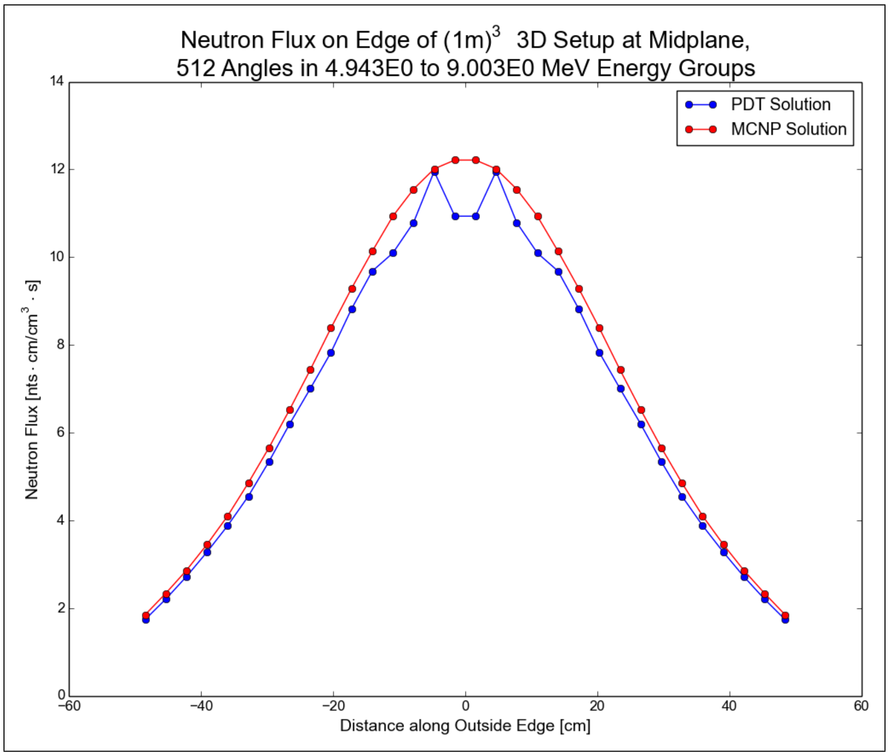

Figure 6.92: Neutron Flux on Edge of $(1m)^3$ 3D Setup at Midplane in $4.9MeV$ to $9.0MeV$ Energy Groups using 512 Angles.

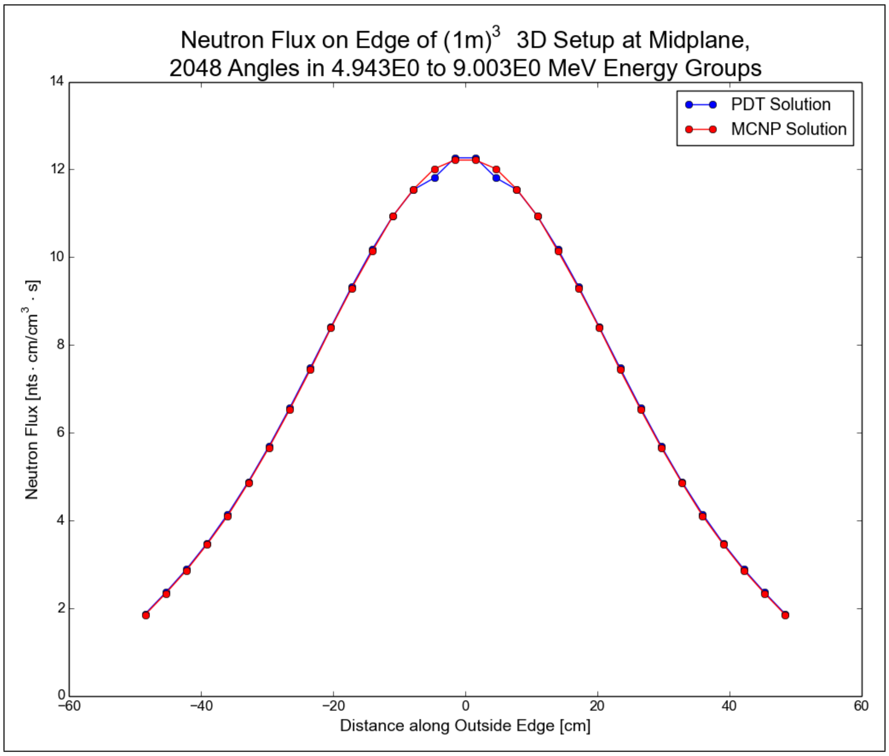

Figure 6.93: Neutron Flux on Edge of $(1m)^3$ 3D Setup at Midplane in $4.9MeV$ to $9.0MeV$ Energy Groups using 2048 Angles.

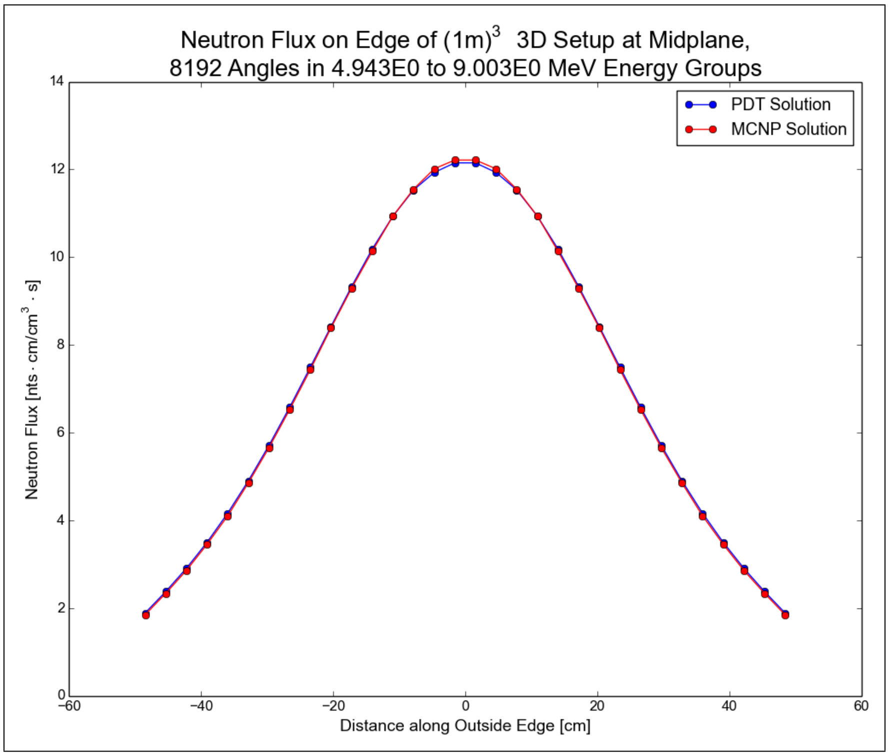

Figure 6.94: Neutron Flux on Edge of $(1m)^3$ 3D Setup at Midplane in $4.9MeV$ to $9.0MeV$ Energy Groups using 8192 Angles.

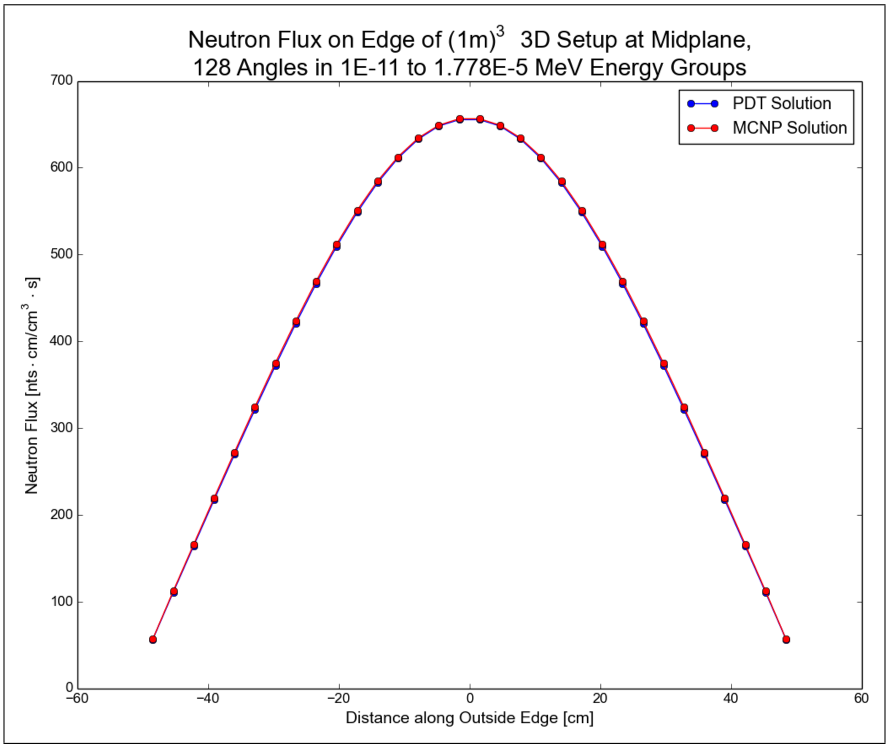

Figure 6.95: Neutron Flux on Edge of $(1m)^3$ 3D Setup at Midplane in $1 \times 10^{-11} MeV$ to $1.78 \times 10^{-5} MeV$ Energy Groups using 128 Angles.

The L2 error is calculated for each energy interval, using the 32k discrete ordinate PDT solution in that specified energy interval as the reference true solution. The L2 error is plotted in Figure 6.96. Similar to the 2D analysis, the L2 errors are seen to be well approximated with power functions. A general trend of higher energy intervals having larger errors is observed. Once again, the lowest energy interval proved to be an exception.

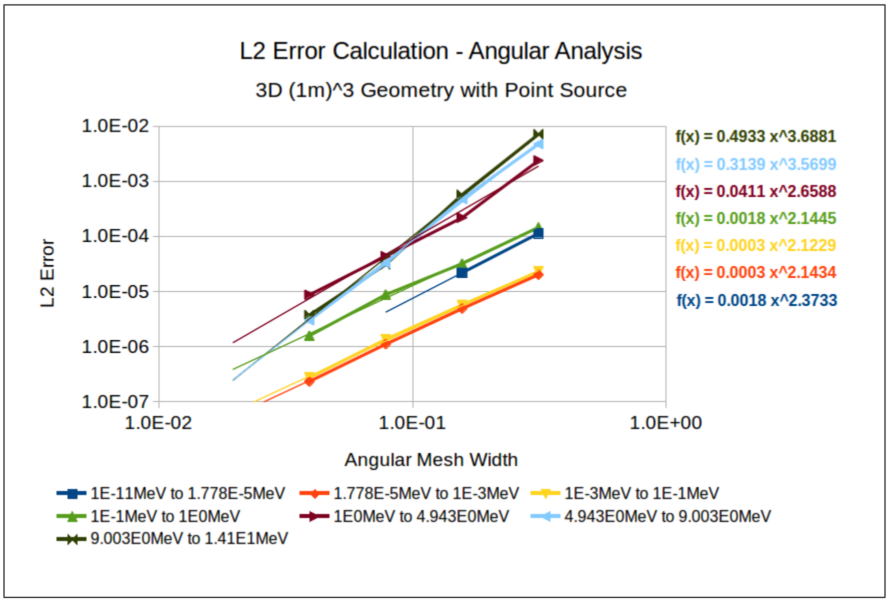

Figure 6.96: L2 Error Angular Analysis using PDT Solution with 32k Discrete Ordinates as Reference Solution in $(1m)^3$.

6.3.3 *Energy Dependent Flux*

The energy dependent flux was plotted at the center cell and at the outer corner cell for both the $(1m)^3$ and $(10m)^3$ geometries. The data was obtained from simulations using 64^3 cells, 127 energy groups, and adequate angular resolution based on the angular analysis. 128 discrete angles were used for energy groups up to $1.78 \times 10^{-5} MeV$, 512 discrete angles were used for energy groups within $1.78 \times 10^{-5} MeV$ to $4.94 MeV$, 2048 discrete ordinates were used for energy groups from $4.94 MeV$ to $7.33 MeV$, and 8192 discrete angles for energy groups above $7.33 MeV$. Figures 6.97 and 6.98, outline the energy dependent neutron flux in the center and corner cell for the $(1m)^3$ geometry. For the center cell, the PDT flux was found to be slightly larger than the MCNP flux in the slowing down region. Additional slowing down region groups would most likely reduce this error. Regardless, overall good agreement is seen between the MCNP and PDT solutions. The energy dependent flux in the corner cell contains jagged peaks in the thermal energy range. This is

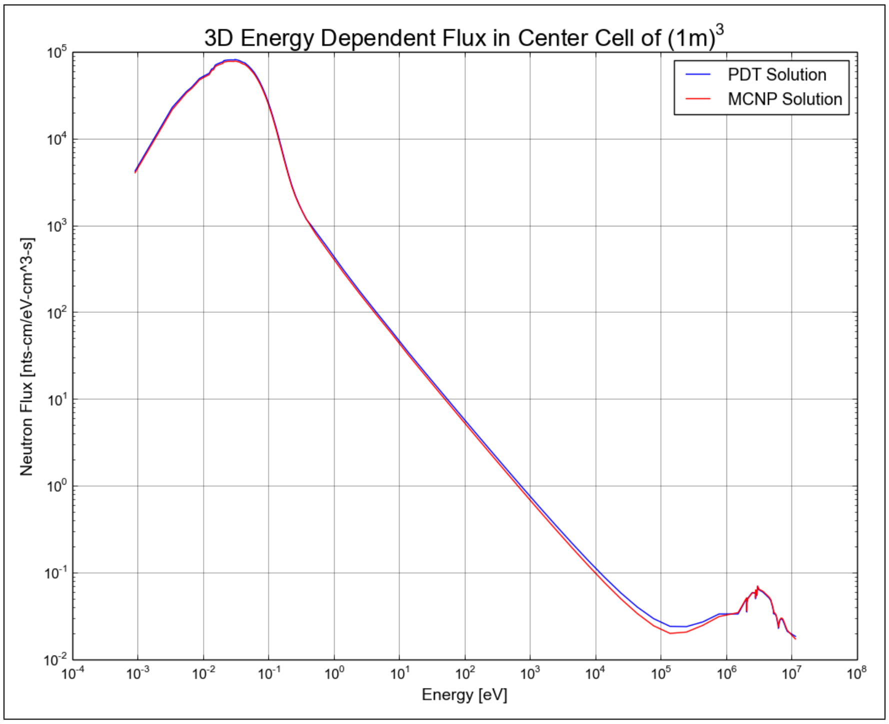

Figure 6.97: Energy Dependent Flux in Center Cell of $(1m)^3$.

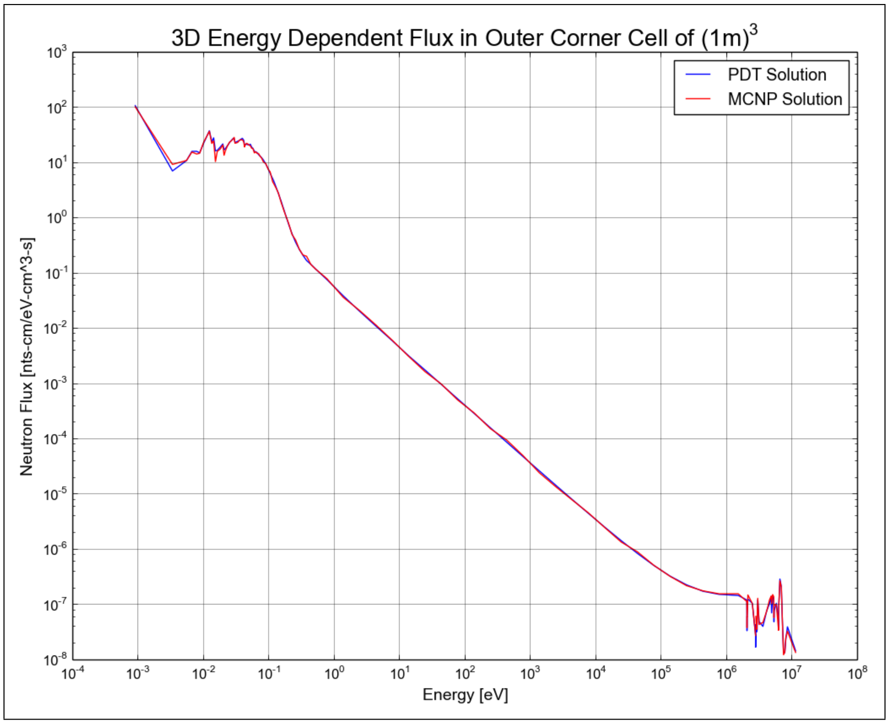

Figure 6.98: Energy Dependent Flux in Corner Cell of $(1m)^3$.

caused by the discontinuities in the coherent scattering cross-sections as described in the 2D geometry energy dependent section.

The energy dependent fluxes for $(10m)^3$ geometry are given in Figures 6.99 and 6.100 for the center and corner cells respectively. The energy dependent flux in the center cell of $(10m)^3$ shows some minor differences mostly in the slowing down region. Just as was seen in the $10m \times 10m$ 2D geometry corner cell, the effect of leakage in the corner cell of the $(10m)^3$ geometry is clearly visible with a flatter flux over the slowing down region and a long Maxwellian tail. With the current number of neutrons simulated in MCNP, very few neutrons were able reach the outer corner cell of the $(10m)^3$ geometry. This is not a major concern for the error calculations since the neutron flux in the outer corner cell of the $(10m)^3$ cube is so small.

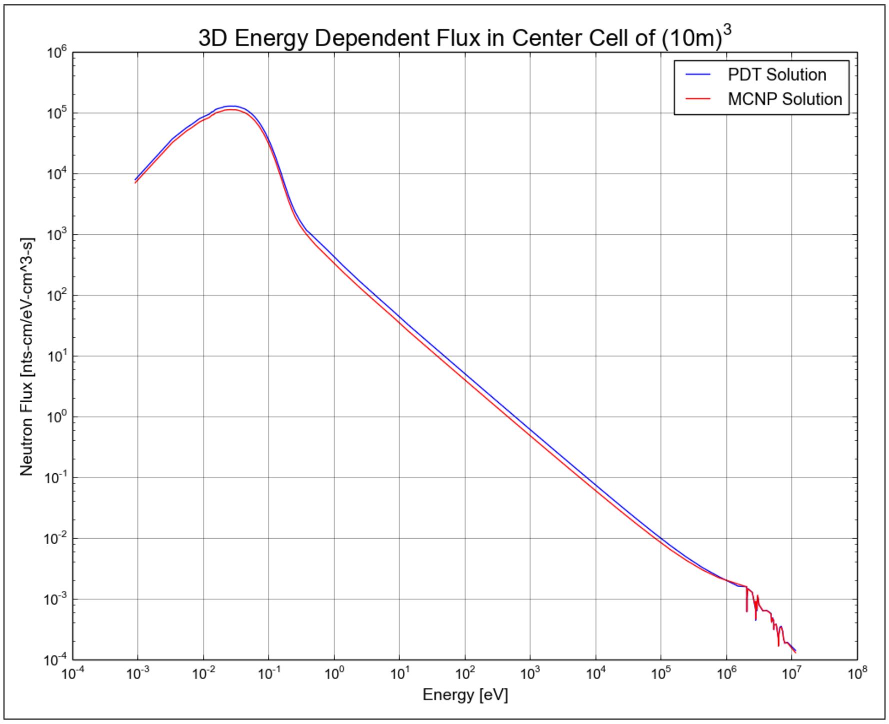

Figure 6.99: Energy Dependent Flux in Center Cell of $(10m)^3$.

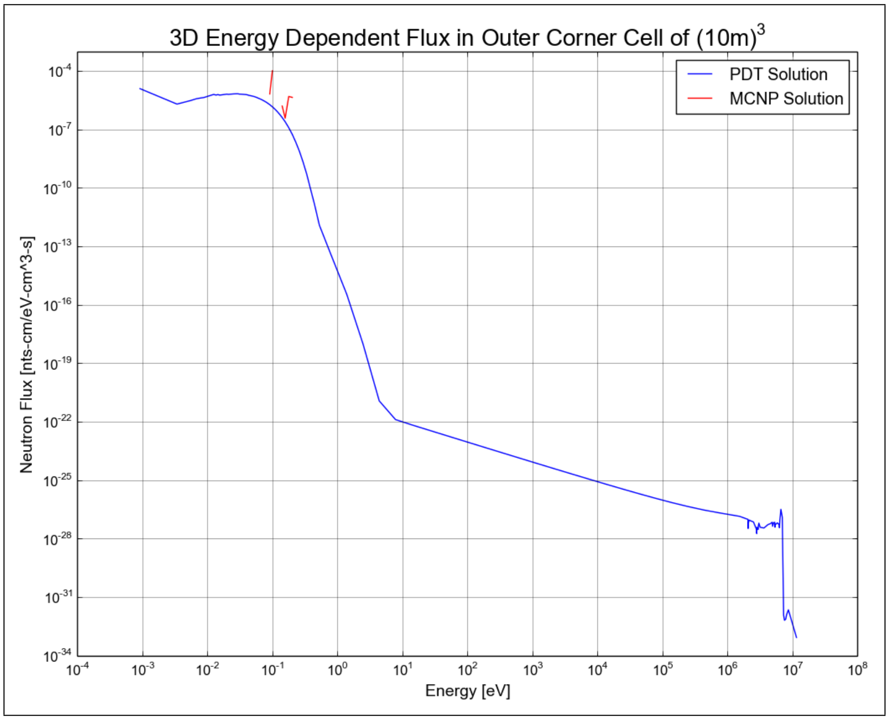

Figure 6.100: Energy Dependent Flux in Corner Cell of $(10m)^3$.

6.4 CSDA Results

This section will discuss the CSDA results. The CSDA solution was built using the modes of the analytic solution outlined in the CSDA chapter of the Computation Models section. The cell and energy averaged CSDA solution was computed for infinite medium with a uniform source, 2D geometry with an infinite line source, and 3D geometry with a point source.

6.4.1 Infinite Medium

For the infinite medium geometry, the energy averaged, energy dependent neutron flux CSDA solution was plotted at the energy midpoints in order to compare with the MCNP and PDT results. The CSDA infinite medium neutron flux solution is shown in Figure 6.101. The CSDA neutron flux solution is seen to closely align with the MCNP and PDT results in the slowing down region. On the other hand, the CSDA results largely differ in the thermal energy region. CSDA makes the major assumption that neutrons slow down continuously such that there are no jumps in energy. This assumption is relatively accurate for the slowing down region, but is completely incorrect for the thermal energy region. In reality, when neutrons slow down to thermal energies they achieve thermal equilibrium with the background media allowing up-scattering to occur. This equilibrium is characterized by a Maxwellian distribution, which is clearly seen in the MCNP and PDT solutions, but is absent in the CSDA solution. There are also differences between CSDA and MCNP present in the high energy range. Zooming in on the high energy region as shown in Figure 6.102, it is seen that CSDA is much lower than MCNP right at the DT source energy (14.1 MeV), but is higher than MCNP over the rest of the fast energy range. This is

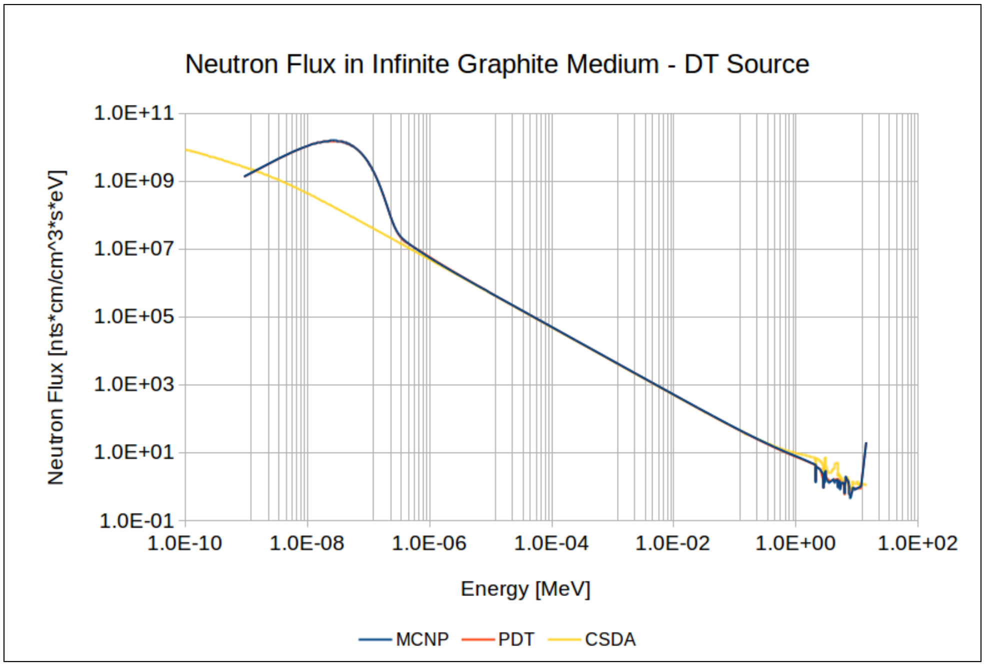

Figure 6.101: Neutron Flux in Infinite Graphite Medium with Uniform DT Source

caused by CSDA not accounting for uncollided neutron flux. Recall that in CSDA, neutrons immediately lose energy as soon as they move in order for them slow down continuously. This means there are no 14.1-MeV neutrons in the CSDA solution except at the source point, whereas in reality (and in MCNP), many 14-MeV neutrons exist relatively far from the source. CSDA misses this, and as a result it is much too low at the source energy (14.1MeV) and too high at energies just below . As result, the CSDA flux is higher than MCNP in the high energy range except at the very high energy tail, where it is much lower than MCNP.

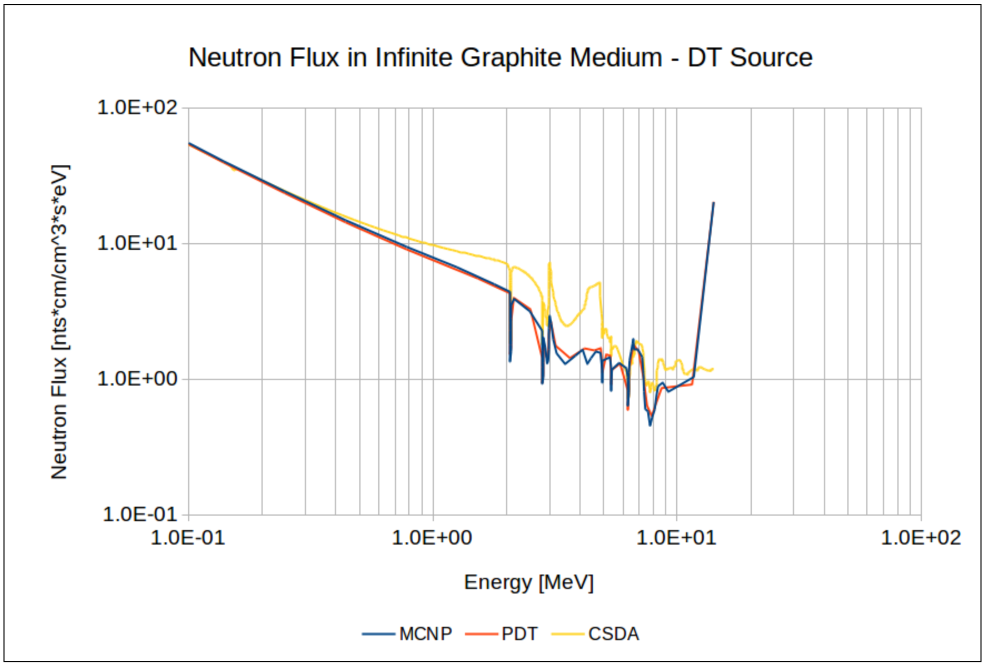

Figure 6.102: Neutron Flux in Infinite Graphite Medium with Uniform DT Source

6.4.2 2D Geometry

The 2D CSDA results were obtained by plotting the cell averaged CSDA solution at the midpoints of the cells. CSDA and MCNP neutron flux results in the $1m \times 1m$ geometry for the thermal group $0.104eV$ to $0.108eV$ with an infinite DT line source are outlined in Figures 6.103 and 6.104 respectively. From the infinite medium solution, we saw that the CSDA solution has a nearly 1/E shape that continues to very low energies, until there is a high enough absorption cross-section. In addition, the CSDA solution does not account for up-scattering. The up-scatter contribution will flatten the spatial distribution of a thermal region group neutron flux. This is because at a distance away from the source, there are neutron contributions from both neutrons slowing down from higher energies and from neutrons up-scattering from lower energies. As result, the CSDA solution is more spatially peaked compared

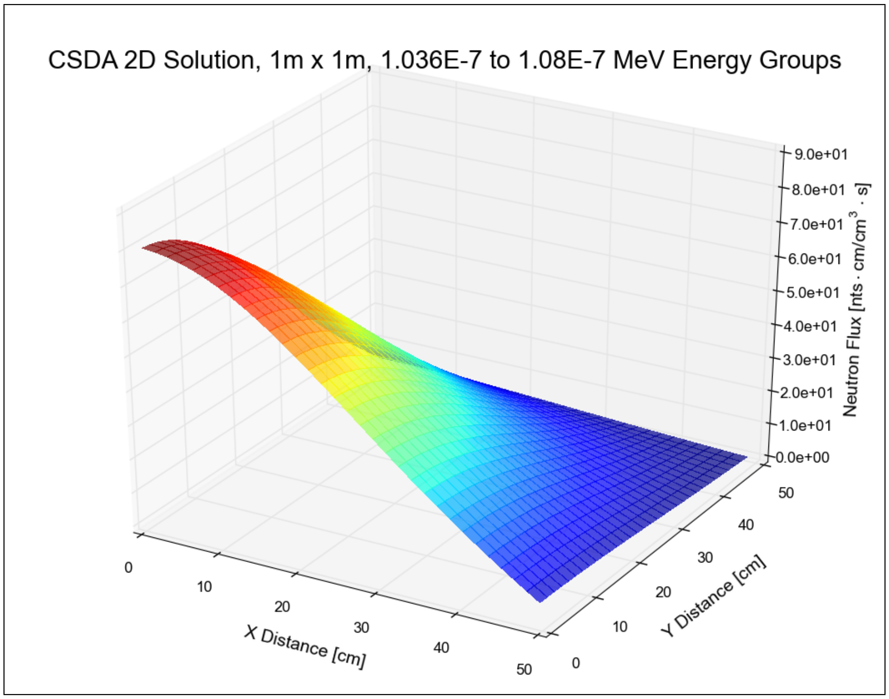

Figure 6.103: CSDA $1m \times 1m$ 2D Neutron Flux Solution in $0.104eV$ to $0.108eV$ Energy Groups.

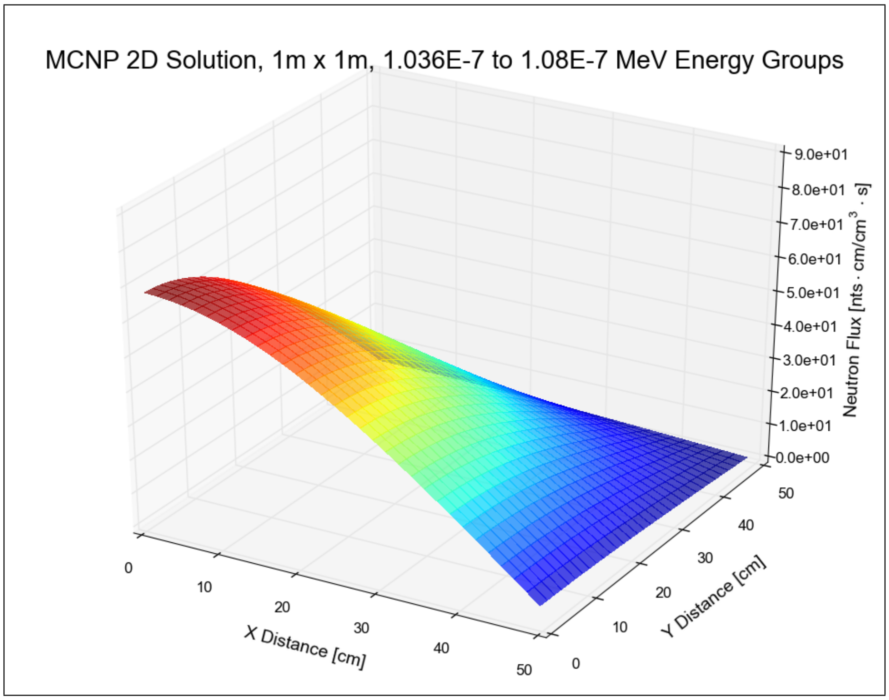

Figure 6.104: MCNP $1m \times 1m$ 2D Neutron Flux Solution in $0.104eV$ to $0.108eV$ Energy Groups.

to the MCNP solution at thermal energies.

Figures 6.105 and 6.106 show the CSDA and MCNP neutron flux at a slowing down energy range of $0.1keV$ to $0.178keV$. The MCNP and CSDA fluxes were found to match closely in this slowing down energy range.

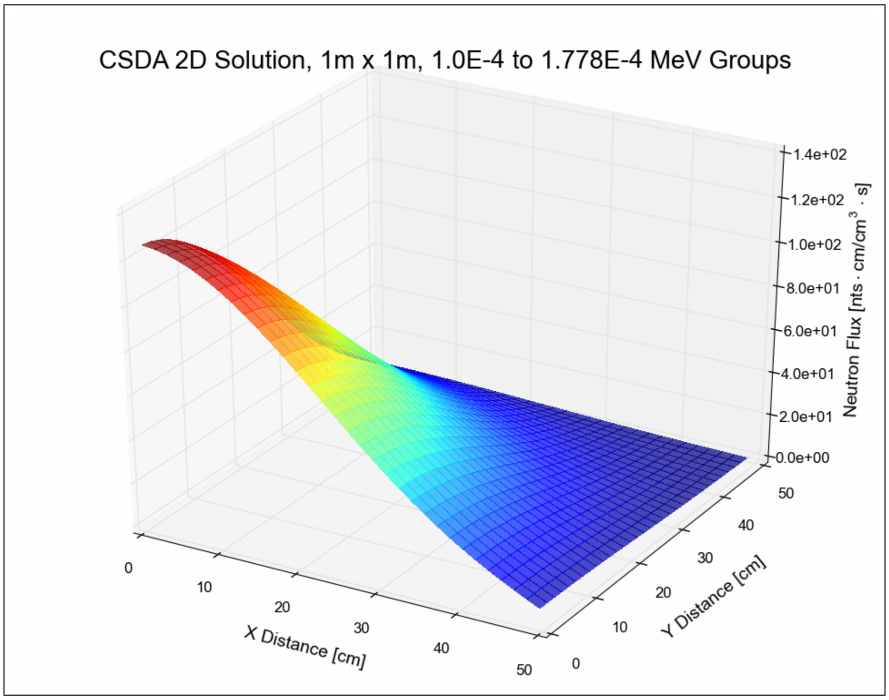

Figure 6.105: CSDA $1m \times 1m$ 2D Neutron Flux Solution in $0.1keV$ to $0.178keV$ Energy Groups.

Last, the CSDA and MCNP neutron flux results in the fast energy range $2.07MeV$ to $2.073MeV$ are given in Figures 6.107 and 6.108. Major differences are evident between the CSDA and MCNP neutron flux solutions in this high energy range where CSDA is lower at the center and is more spatially flat compared to MCNP. These differences are due to the CSDA solution not accounting for uncollided neutron flux.

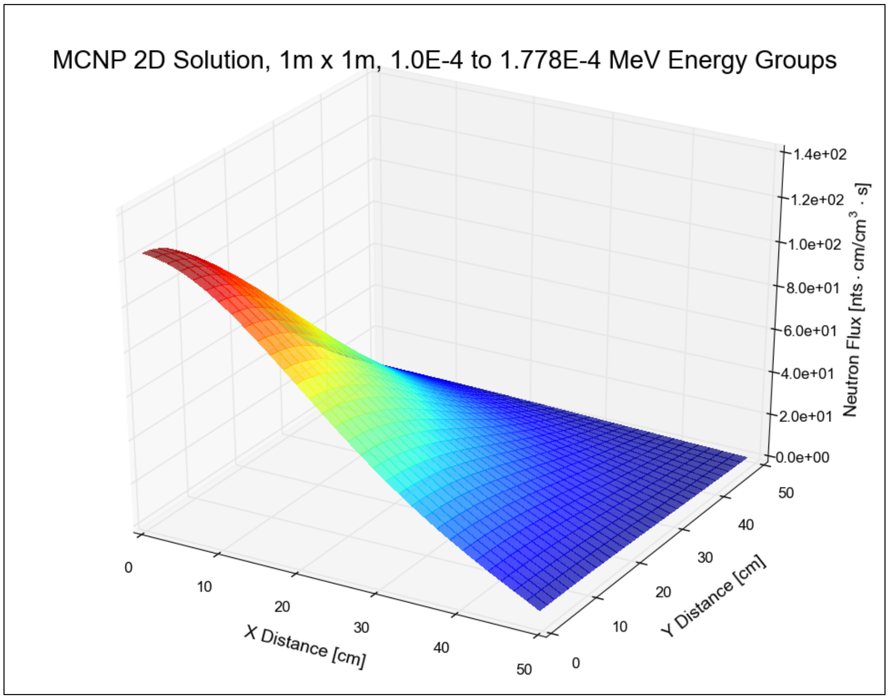

Figure 6.106: MCNP $1m \times 1m$ 2D Neutron Flux Solution in $0.1keV$ to $0.178keV$ Energy Groups.

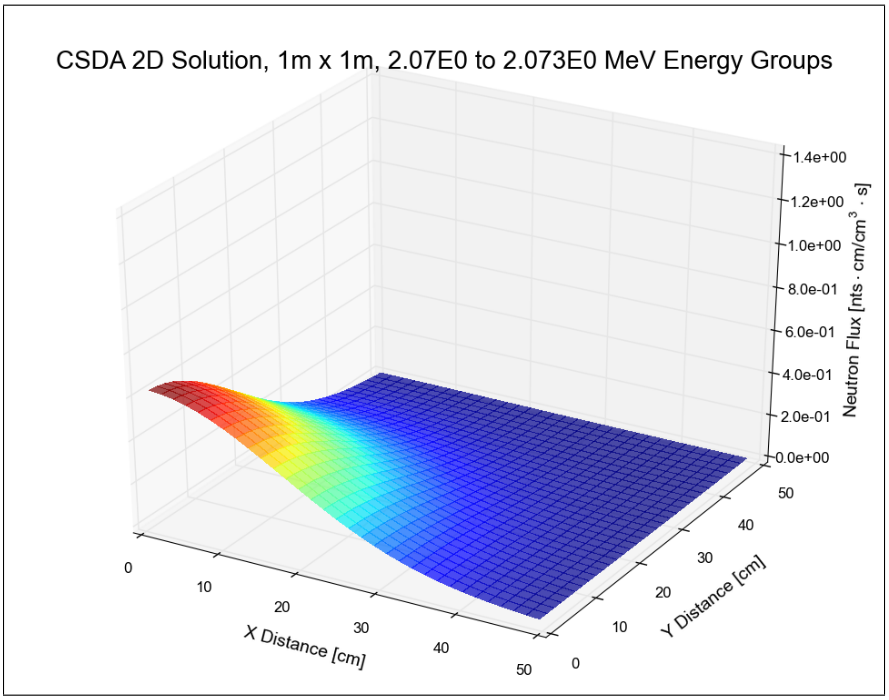

Figure 6.107: CSDA $1m \times 1m$ 2D Neutron Flux Solution in $2.07MeV$ to $2.073MeV$ Energy Groups.

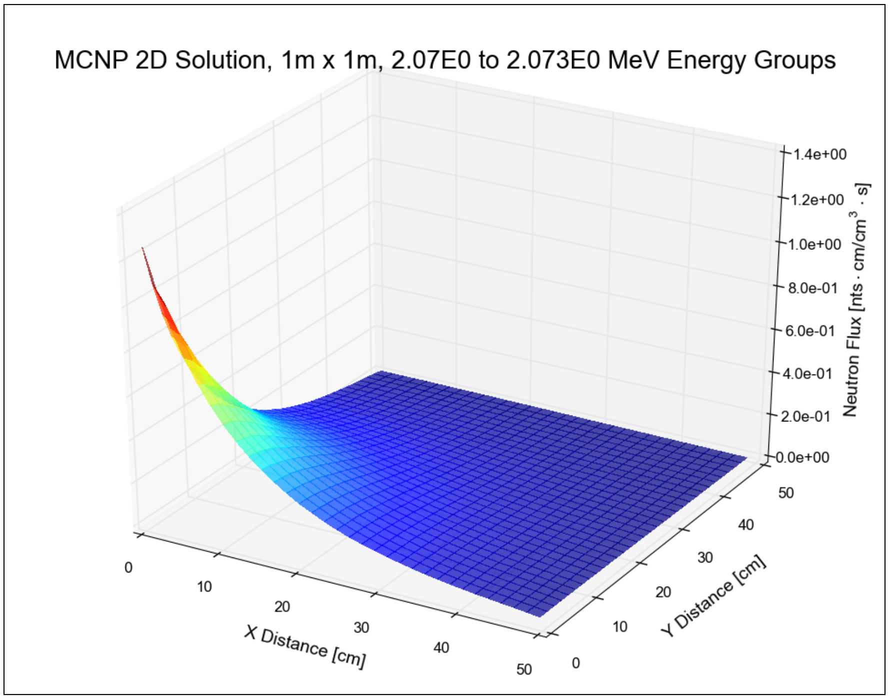

Figure 6.108: MCNP $1m \times 1m$ 2D Neutron Flux Solution in $2.07MeV$ to $2.073MeV$ Energy Groups.

CSDA assumes that particles slow down as soon as they move in order to continuously slow down. In reality and in MCNP there is an uncollided flux contribution heading away from the source. This uncollided flux becomes more significant where streaming becomes more dominant. The neutron scatter cross-section in graphite is lower at fast energies and thus the uncollided flux for fast neutrons will travel farther on average before a collision. As result, in the fast energy region, the CSDA spatial flux distribution will be flatter compared to reality or MCNP, which is clearly seen in Figures 6.107 and 6.108. It is evident from the prior analysis that the CSDA approximation is strongest at slowing down energies and is much weaker at thermal and fast energies.

6.4.3 3D Geometry

The 3D CSDA and MCNP neutron flux results in $(1m)^3$ geometry at midplane with a point DT source for thermal groups $0.104eV$ to $0.108eV$ are outlined in Figures 6.109 and 6.110 respectively. Similar to the 2D results, the CSDA flux is more peaked compared to the corresponding MCNP flux in the thermal region. This is due to CSDA not taking into account up-scattering neutrons, which flattens the neutron flux spatial distribution as described in the 2D CSDA section.

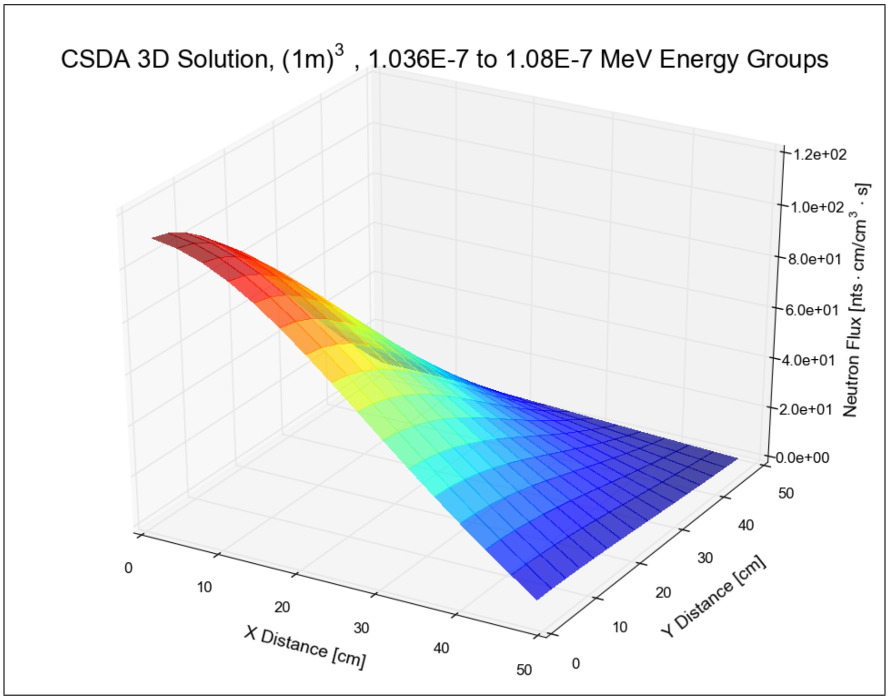

Figure 6.109: CSDA $(1m)^3$ 3D Neutron Flux Solution in $0.104eV$ to $0.108eV$ Energy Groups.

Figures 6.111 and 6.112 show the CSDA and MCNP neutron flux at a slowing down energy range of $0.1keV$ to $0.178keV$. The MCNP and CSDA fluxes were found to

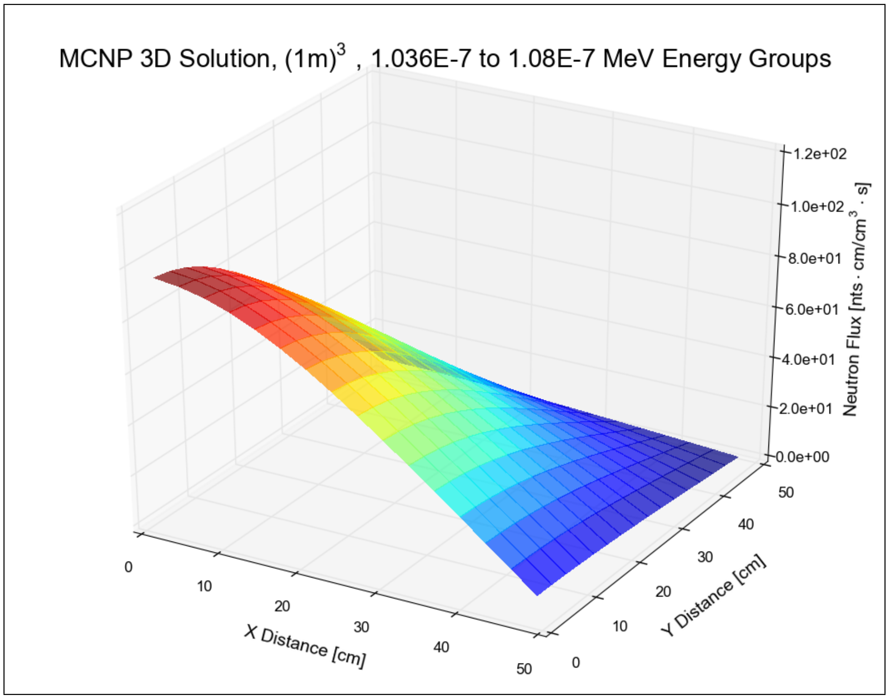

Figure 6.110: MCNP $(1m)^3$ 3D Neutron Flux Solution in $0.104eV$ to $0.108eV$ Energy Groups.

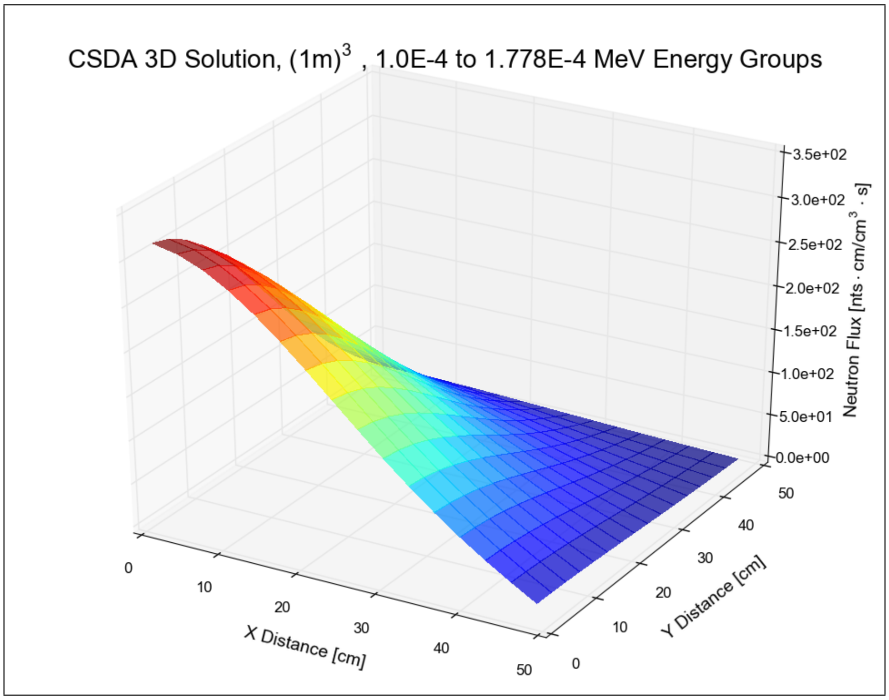

Figure 6.111: CSDA $(1m)^3$ 3D Neutron Flux Solution in $0.1keV$ to $0.178keV$ Energy Groups.

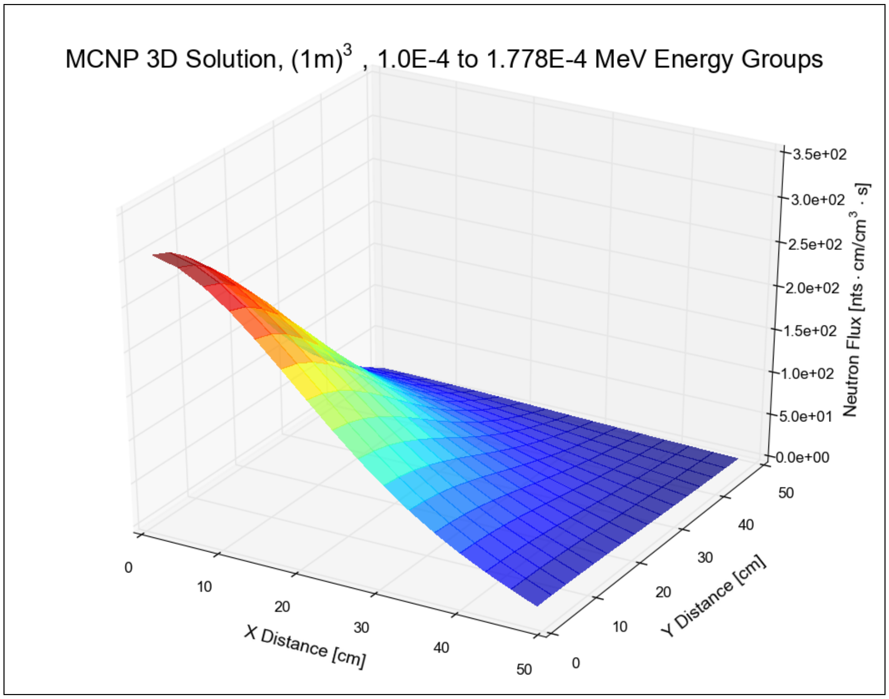

Figure 6.112: MCNP $(1m)^3$ 3D Neutron Flux Solution in $0.1keV$ to $0.178keV$ Energy Groups.

match up closely in the slowing down energy range.

Last, the CSDA and MCNP neutron flux results in the fast energy range $2.07MeV$ to $2.073MeV$ are given in Figures 6.113 and 6.114. It is clear that the CSDA solution is much lower than MCNP at the center. Once again, this is due to CSDA not accounting for the uncollided neutron flux. In reality, there is an uncollided neutron flux contribution travelling away from the source. The fast energy neutron flux for CSDA and MCNP is plotted on the CSDA flux scale in Figures 6.115 and 6.116. From Figures 6.115 and 6.116, it is clear that the CSDA solution is much flatter spatially compared to MCNP. The 3D CSDA analysis confirms that the CSDA approximation is strongest at slowing down energies and is much weaker at thermal and fast energies.

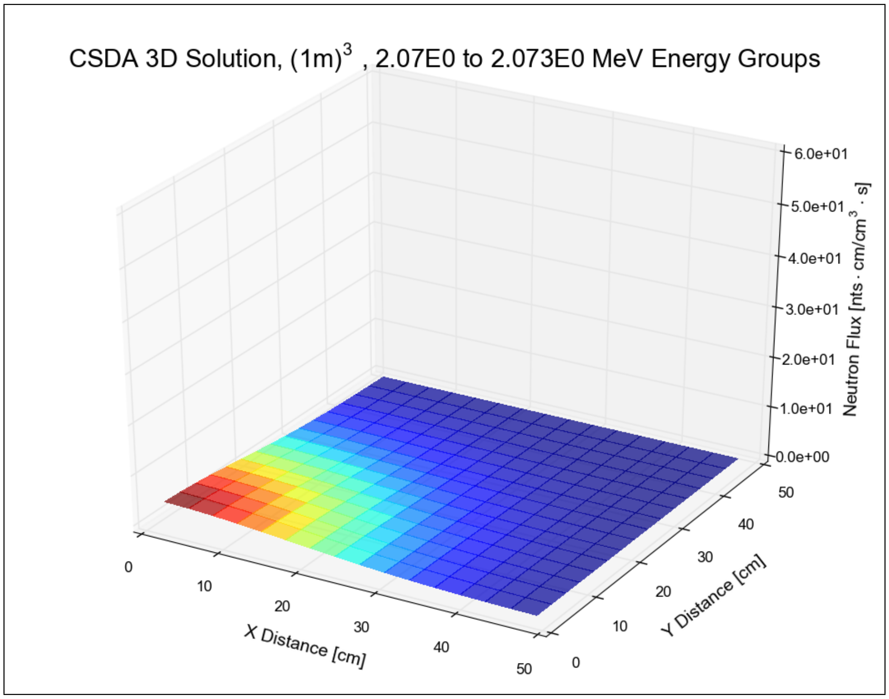

Figure 6.113: CSDA $(1m)^3$ 3D Neutron Flux Solution in $2.07MeV$ to $2.073MeV$ Energy Groups.

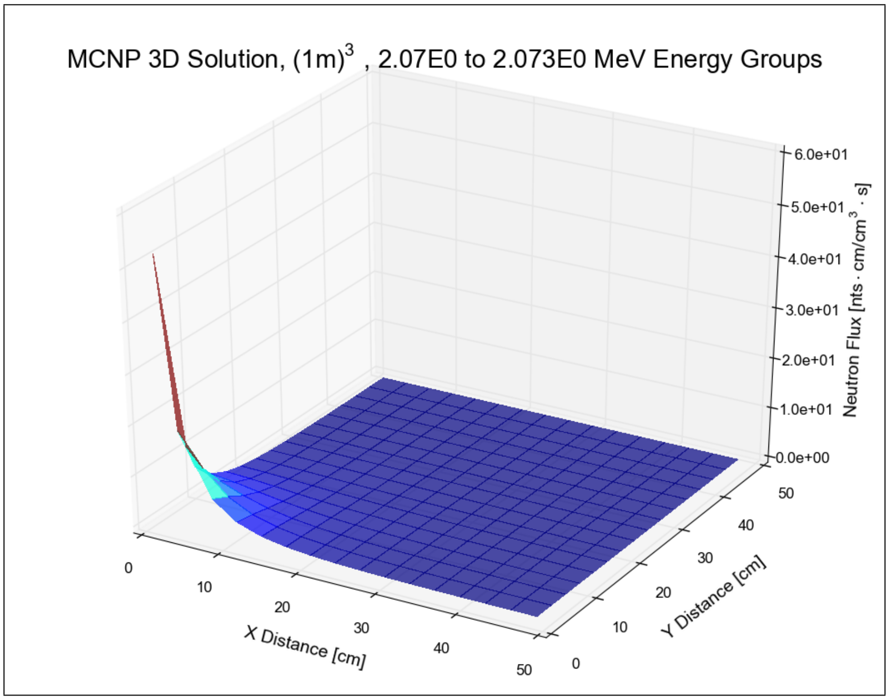

Figure 6.114: MCNP $(1m)^3$ 3D Neutron Flux Solution in $2.07MeV$ to $2.073MeV$ Energy Groups.

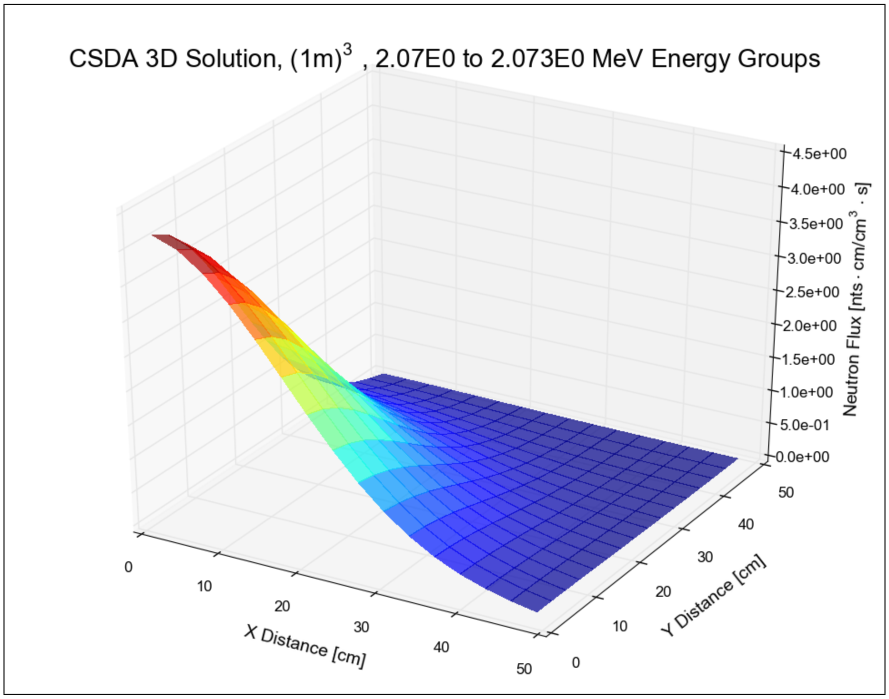

Figure 6.115: CSDA $(1m)^3$ 3D Neutron Flux Solution in $2.07MeV$ to $2.073MeV$ Energy Groups with Upper CSDA Limit.

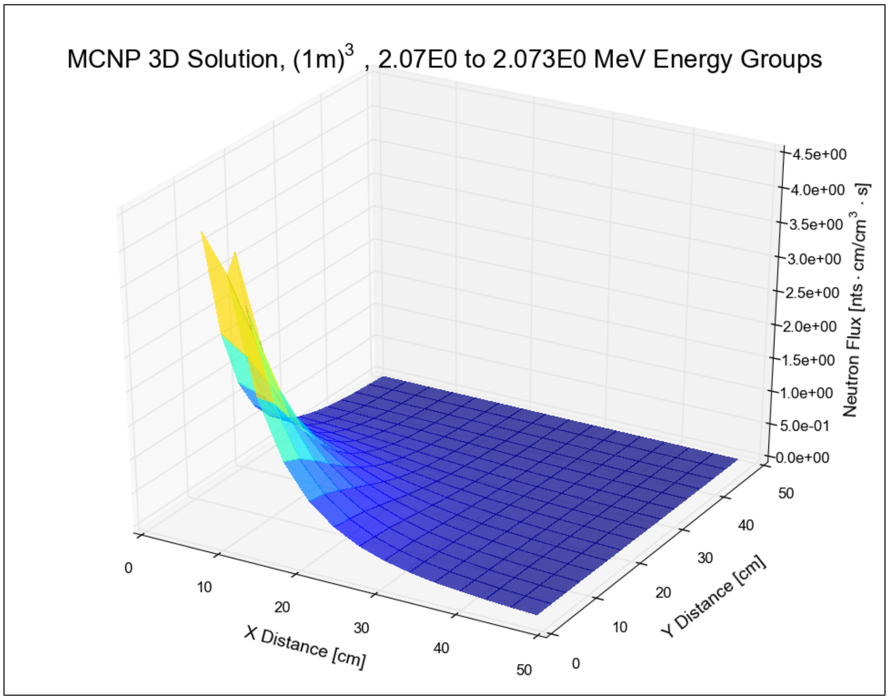

Figure 6.116: MCNP $(1m)^3$ 3D Neutron Flux Solution in $2.07MeV$ to $2.073MeV$ Energy Groups with Upper CSDA Limit.

7. CONCLUSIONS

The CERT project addresses problems of thermal radiation transport in the HED regime that are highly relevant to NNSA. A major challenge to the development of thermal radiation transport is that the strong non-linear coupling of radiation hydrodynamcs and thermal radiation transport makes it very difficult to infer radiation transport uncertainties from experiments. To address this problem, the CERT team has designed neutrons-in-graphite surrogate experiments. It has been shown mathematically that there is a strong analogy between radiative absorption/re-emission and neutrons scattering in highly diffusive mediums that allows the solution for radiation transport benchmark problems to be measured by the neutrons-in-graphite surrogate experiments.

This thesis systematically studied the discretization error as a function of the spatial, angular, and energy resolution for deterministic transport calculations in the neutrons-in-graphite problems that are being studied by CERT. In order to accomplish this goal, semi-analytic (CSDA), stochastic (MCNP), and deterministic (PDT) methodologies were utilized in several sets of problems: infinite medium with a uniform AmBe and DT source spectra, two-dimensional graphite problem with a infinite AmBe line source, and graphite cube with a AmBe point source. Results from these computational approaches were compared to determine what angle, energy, and spatial resolution was needed to obtain high-fidelity deterministic neutron transport solutions. The deterministic discretization error was computed as function of the spatial, angular, and energy resolution.

In infinite medium geometry, the solution only has energy dependence. Energy group structures using varying number of thermal, transition from thermal to slowing down, slowing down, and fast energy groups were modelled. The L2 error analysis was performed independently in each energy region in order to investigate how the number of energy groups in each energy region affects the discretization error. An adequate energy group structure that provided sufficiently small error and a reasonably small number of groups was found to have 127 groups consisting of 61 thermal groups below energy 0.5 eV, 25 slowing down energy groups between energies 0.5 eV and 1.0 MeV, and 41 fast energy groups with energy greater than $1.0 MeV$. Here "sufficiently small" means small enough to not significantly confound the study of spatial and angular discretization errors.

A spatial analysis was performed for both the 2D and 3D geometries. The theoretical fine-mesh convergence rate for the smooth portion of the analytic solution is second order. The convergence rate was found to be initially very low for the very coarse spatial refinement in both the $1m \times 1m$ and $10m \times 10m$ geometries and increased with increasing spatial refinement. In $1m \times 1m$ geometry, the convergence rate increased to 1.59 for the 64x64 spatial grid. In $10m \times 10m$ geometry, the convergence rate approached second order with a value of 2.07. In 3D geometry, the convergence rate started low for the coarse mesh and increased to 2.89 and 2.90 for the $(1m)^3$ and $(10m)^3$ geometries respectively on the 64x64x64 spatial mesh.

The angular analysis was performed independently in multiple energy ranges in order to compute the angular discretization as function of the angular resolution in various energy ranges. For the 2D infinite line source geometry, notable ray affects were present using a 128 angle quadrature set for energies above $1.0 MeV$. Using a 512 angle quadrature set, resolved the majority of the angular discretization errors from ray effects. Additional error reduction was seen using the 2048 angle quadrature set.

This was seen in both the $1m \times 1m$ and the $10m \times 10m$ geometries. Ray effects were much less dominant for lower neutron energies. Minimal angular discretization error was seen for energies below 0.1 MeV when using the 128 angle quadrature set in both the $1m \times 1m$ and the $10m \times 10m$ geometries. Similar results were seen in the 3D point source geometry with significant angular discretization errors from ray effects present in energies greater than $1.0 MeV$ for the 128 angle quadrature set. Once again, the 512 angle quadrature set resolved the majority of these ray effects. For energies less than 0.1 MeV, there were not significant angular discretization errors when using the 128 angle quadrature set. Computing angular discretization L2 errors for each energy interval where the PDT solution with 32k discrete angles in that specified energy interval was utilized as the reference true solution. The errors were found to be closely approximated by power functions.

The semi-analytic CSDA method was found to be strong in the slowing down energy region. However, large errors in the CSDA results were found in the thermal and fast energy regions. The CSDA assumption that neutrons slow down continuously such that there are no jumps in energy is weak at thermal energies where up-scattering occurs. This results in the CSDA solution being less spatially flat compared to reality or MCNP. In addition, the CSDA solution does not account for the uncollided neutron flux since it assumes that neutrons immediately slow down as soon as they move in order for them to continuously slow down. This becomes more significant at energies where streaming becomes more significant (lower scattering cross-section). Since the neutron scattering cross-section in graphite is lower at high energies, the CSDA solution in the fast energy range becomes much flatter compared to reality and MCNP. In future work, it would be interesting to explore the improvement in the CSDA solution if the uncollided flux were computed analytically and the CSDA were used only to compute the flux of scattered neutrons.

In summary, the deterministic discretization error was studied as function of the spatial, angular, and energy resolution for the neutrons-in-graphite problems of interest to the CERT project. This research has provided valuable information about uncertainty quantification for CERT and for the further development of PDT.

REFERENCES

[1] Marvin L. Adams. Discontinuous finite-element transport solution in the thick diffusion limit in cartesian geometry. *The American Nuclear Society International Topical Meeting*, Jan 1991. Pittsburgh, PA.

[2] Marvin L. Adams and Edward W. Larsen. Fast iterative methods for discrete-ordinates particle transport calculations. *Progress in Nuclear Energy*, 40(1):3–159, 2002.

[3] Michael P. Adams, Marvin L. Adams, Daryl W. Hawkins, Timmie Smith, Lawrence Rauchwerger, Nancy M. Amato, Teresa S. Bailey, and Robert D. Falgout. Provably optimal parallel transport sweeps on regular grids. *Joint International Conference on Mathematics and Computation (M&C), Supercomputing in Nuclear Applications (SNA) and the Monte Carlo (MC) Method*, May 2013. Sun Valley, Idaho.

[4] Michael P. Adams, Marvin L. Adams, Carolyn N. McGraw, Andrew T. Till, and Teresa S. Bailey. Provably optimal parallel transport sweeps with non-continguous partitions. *Joint International Conference on Mathematics and Computation (M&C), Supercomputing in Nuclear Applications (SNA) and the Monte Carlo (MC) Method*, Apr 2015. Nashville, Tennessee.

[5] Teresa S. Bailey. *The Piecewise Linear Discontinuous Finite Element Method Applied to the RZ and XYZ Transport Equations.* Doctor of philosophy, Texas A&M University, May 2008.

[6] Teresa S. Bailey, Marvin L. Adams, B. Yang, and M. R. Zika. A piecewise linear finite element discretization of the diffusion equation for arbitrary polyhedral grids. *J. Computer Physics*, 227:3738–3757, 2008.

[7] George I. Bell and Samuel Glasstone. *Nuclear Reactor Theory.* Van Nostrand Reinhold Company, New York, N.Y., first edition, 1970.

[8] A. Buss, A. Fidel, T. Smith Harshvardan, G. Tanase, N. Thomas, X. Xu, M. Bianco, N. M. Amato, and L. Rauchwerger. The stapl pview. *LCPC*, pages 7–9, Oct 2010.

[9] A. Buss, Harshvardan, I. Papadopoulos, O. Pearce, T. Smith, G. Tanase, N. Thomas, X. Xu, M. Bianco, N. M. Amato, and L. Rauchwerger. Stapl: Standard template adaptive parallel library. *SYSTOR*, 4:1–10, June 2010.

[10] Mark David DeHART. *A Discrete Ordinates Approximation to the Neutron Tranport Equation Applied to Generalized Geometries.* Doctor of philosophy, Texas A&M University, 1992.

[11] James J. Duderstadt and Louis J. Hamilton. *Nuclear Reactor Analysis.* Jon Wiley & Sons, Inc., first edition, 1976.

[12] A. Fidel Harshvardan, N. M. Amato, and L. Rauchwerger. The stapl parallel graph library. *Wkshp. on Lang. and Comp. for Par. Comp. (LCPC)*, Sep 2012. Tokyo, Japan.

[13] Daryl Hawkins, Timmie Smith, Michael Adams, Lawrence Rauchwerger, Nancy Amato, and Marvin Adams. Efficient massively parallel transport sweeps. *Transactions of the American Nuclear Society*, 107:477–481, Nov 2012.

[14] W. Daryl Hawkins. Parallel deterministic transport scaling results. personal communication.

[15] Frank P. Incropera, David P. Dewitt, Theodore L. Bergman, and Adrienne S. Lavine. *Fundamentals of Heat and Mass Transfer*. Jon Wiley & Sons, Inc., sixth edition, 2007.

[16] Joshua J. Jarrell and Marvin L. Adams. Discrete-ordinates quadrature sets based on linear discontinuous finite elements. *International Conference on Mathematics and Computational Methods Applied to Nuclear Science and Engineering*, May 2011. Rio de Janeiro, Brazil.

[17] John Lamarsh and Anthony Baratta. *Introduction to Nuclear Reactor Theory*. Prentice Hall, Upper Saddle River, N.J., third edition, 2001.

[18] Edward W. Larsen, Jim E. Morel E. E. Lewis, Jerome Spanier, R. N. Hwang Robert Roy, Dan G. Cacuci, G. E. Whitesides, R. M. Westfall, C. M. Hopper, and Jakc Dorning. *Nuclear Computational Science: A Century in Review*. Springer Dordrecht Heidelberg London New York, 2010.

[19] Cheuk Y. Lau and Marvin L. Adams. Discrete-ordinates quadratures based on linear and quadratic discontinuous finite elements over spherical quadrilaterals. *Joint International Conference on Mathematics and Computation (M&C), Supercomputing in Nuclear Applications (SNA) and the Monte Carlo (MC) Method*, Apr 2015. Nashville, Tennessee.

[20] E. E. Lewis and Jr. W. F. Miller. *Computational Methods of Neutron Transport*. Jon Wiley & Sons, Inc., first edition, 1984.

[21] Ben Q. Li. *Discontinuous finite elements in fluid dynamics and heat transfer.* Springer, London, 2006.

[22] R. E. MacFarlane, D. W. Muir, R. M. Boicourt, and A. C. Kahler. *The NJOY Nuclear Data Processing System, Version 2012.* Los Alamos National Laboratory, Los Alamos, NM, Dec 2012. LA-UR-12-27079.

[23] Ryan G. McClarren. Temperature-extrapolation method for implicit monte carlo - radiation hydrodynamics calculations. *International Conference on Mathematics and Computational Methods Applied to Nuclear Science & Engineering (M&C 2013)*, May 2013. LaGrange Park, IL.

[24] Ryan G. McClarren, Marvin L. Adams, Derek Bingham, Leslie A. Braby, Thomas Conroy, Jim E. Morel, Delia Perez-Nunez, and Jean Ragusa1. Uncertainty quantification and predictive science for high-energy density radiative transfer using neutron experiments. *11th World Congress on Computational Mechanics (WCCM XI)*, Jul 2014.

[25] Carolyn N. McGraw, Marvin L. Adams, W. Daryl Hawkins, Michael P. Adams, and Timmie Smith. Accuracy of the linear discontinuous galerkin method for reactor analysis with resolved fuel pins. *International Conference on the Physics of Reactors*, Sep 2015. Kyoto, Japan.

[26] Jim Morel, Marvin Adams, Les Braby, Ryan McClarren, Jean Ragusa, Lawrence Rauchwerger, Nancy Amato, Derek Bingham, Tom Conroy, Tom Manteuffel, Steve McCormick, and Delia Perez-Nunez. Center for exascale radiation transport proposal. Texas A&M University, Jul 2013.

[27] Fynn Scheben. *Iterative Methods for Criticality Computations in Neutrons Transport Theory.* Doctor of philosophy, University of Bath, Jan 2011.

[28] J. K. Shultis and R. E. Faw. *An MCNP Primer.* Kansas State University, Manhattan, KS, Dec 2011.

[29] Hiromi G. Stone and Marvin L. Adams. A piecewise linear finite element basis with application to particle transport. *Nuclear Mathematical and Computational Sciences: A Century in Review, A Century Anew*, Apr 2003. Gatlinburg, Tennessee.

[30] Hayes Franklin Stripling. *Adjoint-Based Uncertainty Quantification and Sensitivity Analysis for Reactors Depletion Calculations.* Doctor of philosophy, Texas A&M University, Aug 2013.

[31] G. Tanase, A. Buss, A. Fidel, I. Papadopoulos Harshvardan, O. Pearce, T. Smith, N. Thomas, X. Su, N. Mourad, J. Vu, M. Bianco, N. M. Amato, and L. Rauchwerger. The stapl parallel container framework. *Proc. ACM SIGPLAN Symp. Prin. Prac. Par. Prog*, 2011.

[32] X-5 Monte Carlo Team. *MCNP - A General Monte Carlo N-Particle Transport Code, Version 5 - Volume I: Overview and Theory.* Los Alamos National Laboratory, Los Alamos, NM, Feb 2008. LA-UR-03-1987.

[33] Yaqi Wang. *Adaptive Mesh Refinement Solution Techiques for the Multigroup SN Transport Equation Using a Higher-Order Discontinuous Finite Element Method.* Doctor of philosophy, Texas A&M University, Apr 2009.